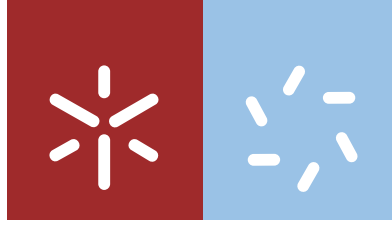


Universidade do Minho
Escola de Ciências

Sharath Kumar Manjeshwar Sathyanath

**Electron Microscopy and Spectroscopy Study
of Modified Titanate Nanowires and Nanotubes**

July 2018



Universidade do Minho
Escola de Ciências

Sharath Kumar Manjeshwar Sathyanath

**Electron Microscopy and Spectroscopy Study
of Modified Titanate Nanowires and Nanotubes**

Master's Degree in Physics - Applied Physics

Supervisors:

Professor Anabela Gomes Rolo
Dr Leonard Deepak Francis

July 2018

Name: Sharath Kumar Manjeshwar Sathyanath

E-mail address: sharathkumar_nitt@yahoo.com

Phone: +351 934113349

Identity Card Number: K8689372

Title of dissertation: Electron Microscopy and Spectroscopy Study of Modified Titanate Nanowires and Nanotubes

Supervisors: Professor Anabela Gomes Rolo, Department of Physics, University of Minho and Dr Leonard Deepak Francis, Department of Advanced Electron Microscopy, Imaging and Spectroscopy, International Iberian Nanotechnology Laboratory (INL)

Year of completion: 2018

Master's Degree: Master's Degree in Physics - Applied Physics

Declaration

I, Sharath Kumar Manjeshwar Sathyanath, declare that the full reproduction of this thesis is only authorised for research purposes through written statement by the interested party.

University of Minho, ____/____/____

Signature: _____

ACKNOWLEDGEMENTS

I would like to express my sincere gratitude to my supervisors Prof. Anabela Gomes Rolo, Department of Physics, University of Minho and Dr. Leonard Deepak Francis, Department of Advanced Electron Microscopy, Imaging and Spectroscopy at the International Iberian Nanotechnology Laboratory (INL), for providing me the opportunity to pursue this project and for their continuous guidance to successfully complete this work.

I would also like to thank INL for giving me the opportunity to carry out my thesis work at the Department of Advanced Electron Microscopy, Imaging and Spectroscopy.

Also, I would like to thank Dr. Beatriz Barrocas and Prof. Olinda C. Monteiro from Center for Chemistry and Biochemistry and Center for Structural Chemistry, Faculty of Sciences, University of Lisbon, Portugal for providing the samples investigated and also for the fruitful discussions during this work.

My sincere thanks also goes to Dr. Enrique Carb-Argibay, Department of Advanced Electron Microscopy, Imaging and Spectroscopy at the International Iberian Nanotechnology Laboratory (INL) for training me on the electron microscopes at INL, and also for providing the timely help during microscopy sessions.

I would like to thank Dr. Alex Bondarchuk, Department of Advanced Electron Microscopy, Imaging and Spectroscopy at the International Iberian Nanotechnology Laboratory (INL), and Dr. Carlos P. Moreira, Director, Materials Centre of the University of Porto (CEMUP), for carrying out XPS analysis. I would like to thank Dr. Maria de Fatima Guimaraes Cerqueira, and Prof. Anabela Gomes Rolo from the Department of Physics, University of Minho, for carrying out Raman measurements at INL and at DF-UM. Also I would like to thank Prof. Maria do Rosario Correia from the Department of Physics and i3N, University of Aveiro, for allowing us to carry out Raman measurements. I would like to thank Dr. Daniel Stroppa from Thermo Fischer for providing trainings on electron microscopy techniques. I would like to thank Dr. Luis Manuel Gomes Vieira, Department of Physics, University of Minho for helping with IR experiments and Dr. Nagamalai Vasimalai, Department of Nano-for-Environment, INL for helping in preparing samples for XPS analysis. I would like to thank Dr

Sebastian Calderon Velasco, Department of Advanced Electron Microscopy, Imaging and Spectroscopy at the International Iberian Nanotechnology Laboratory (INL) and Dr. Nasim Alem, Department of Materials Science and Engineering, Penn State University, USA, for giving me useful suggestions on electron microscopy and analysis.

I would like to thank Dr. Junjie Li and Dr. Anumol Ashokkumar for their help during the thesis work. I would also like to thank my batch mates at University of Minho, and all my friends.

Last but not the least, I would like to thank my family for their constant encouragement and support.

ELECTRON MICROSCOPY AND SPECTROSCOPY STUDY OF MODIFIED TITANATE NANOWIRES AND NANOTUBES

ABSTRACT

One dimensional titanate nanostructures, such as titanate nanowires (TNWs) and nanotubes (TNTs), are promising alternatives to TiO_2 in various applications including photocatalysis. They combine the properties of TiO_2 nanoparticles with the properties of layered titanates such as ion exchange ability and higher specific surface area, due to their open mesoporous morphology.

In this thesis, investigations on cobalt doped and intercalated titanate nanowires and nanotubes using various characterization techniques are presented. Aberration corrected electron microscopy along with energy dispersive x-ray spectroscopy (EDX), is employed to ascertain the morphology, structure and chemical composition of the titanate nanostructures. In order to minimize electron beam induced damage, electron microscopy was carried out at 80 kV. EDX mapping revealed the distribution of the various elements including the dopant intercalant cobalt in both nanotubes and nanowires. L_3/L_2 white line ratio in energy loss spectroscopy (EELS) is used to determine the oxidation state of cobalt in the modified titanate nanostructures, from single nanowire/nanotube. This analysis indicates the presence of cobalt in mixed oxidation state (2+ and 3+) in doped samples and 2+ oxidation state in intercalated samples. These findings were further confirmed by X-ray photoelectron spectroscopy (XPS) measurements. Raman analysis showed notable changes in the characteristic Raman peaks in the case of cobalt doped and intercalated titanate nanowires and nanotubes in comparison to the reference titanate nanowires and nanotubes. Cobalt incorporation was better achieved in the intercalated TNT and TNW samples in comparison to that of doped TNTs and TNWs.

The findings in this work are very relevant because they can contribute to better understand, and even anticipate, the performance of such metal modified nanostructures, since they make possible to relate the performance with the amount, position and oxidation state of the metal in the nanostructure.

ESTUDO DE MICROSCOPIA ELETRÓNICA E ESPECTROSCOPIA DE NANOFIOS E NANOTUBOS DE TITANATO MODIFICADO

RESUMO

As nanoestruturas unidimensionais de titanato, ou seja, nanofios (TNWs) e nanotubos (TNTs), apresentam-se como alternativas muito promissoras ao TiO_2 em várias aplicações, em particular como fotocatalisadores. Estas estruturas combinam as propriedades e aplicações, das nanopartículas de TiO_2 , como por exemplo atividade (foto)catalítica com as propriedades dos titanatos lamelares, como a capacidade de troca iónica e elevada área superficial, decorrente da morfologia mesoporosa que apresentam. Nesta tese, são apresentados estudos de caracterização, de nanofios e nanotubos de titanato dopados e intercalados com cobalto, usando diferentes técnicas instrumentais. Neste âmbito, a microscopia eletrónica de aberração corrigida juntamente com a espectroscopia de energia dispersiva de raios X(EDX), foram utilizadas para averiguar a morfologia, estrutura e composição química das nanoestruturas de titanato. Nos estudos de microscopia eletrónica, e de forma a minimizar os danos criados pelo feixe de eletrões, foram aplicadas tensões na ordem dos 80 kV. O mapeamento de EDX revelou a distribuição dos vários elementos, incluindo o cobalto utilizado como dopante/intercalante nos nanotubos e nanofios. A razão L_3/L_2 da linha branca na espectroscopia de perda de energia (EELS) foi usada para determinar o estado de oxidação do cobalto nas nanoestruturas alongadas de titanato modificado. As análises efetuadas em partículas isoladas de TNTs e TNWs modificados indicam a presença de cobalto com estado de oxidação misto (2+ e 3+) nas amostras dopadas e com estado de oxidação (2+) nas amostras intercaladas. Estes resultados foram confirmados por medidas de espectroscopia fotoeletrónica de raios X (XPS). Por espectroscopia Raman verificaram-se mudanças significativas nos picos característicos para os casos dos nanofios e nanotubos de titanato dopados ou intercalados com cobalto, quando comparados com os obtidos para as estruturas de referência, TNTs e TNWs. A incorporação de cobalto foi melhor conseguida nas amostras intercaladas de TNTs e TNWs quando comparadas com os TNTs e TNWs dopados.

Os resultados obtidos no decorrer deste trabalho são muito relevantes pois permitem compreender melhor, e mesmo antecipar, o desempenho destas estruturas modificadas, pois torna possível relacionar o desempenho de um determinado material, modificado por incorporação de um metal, com a quantidade, a posição e o estado de oxidação desse mesmo metal na estrutura.

List of Abbreviation

ABF Annular Bright Field

BF Bright Field

BFP Back Focal Plane

CCD Charge Coupled Device

CDF Centered Dark Field

Co-TNT Cobalt doped titanate nanotube

Co-TNW Cobalt doped titanate nanowire

DF Dark Field

DP Diffraction Pattern

EDX Energy-dispersive X-ray spectroscopy

EELS Electron Energy Loss Spectroscopy

ESCA Electron Spectroscopy for Chemical Analysis

GIF Gatan Image Filter

HAADF High Angle Annular Dark Field

HRTEM High Resolution Transmission Electron Microscopy

SAEDP Selected Area Electron Diffraction Pattern

STEM Scanning Transmission Electron Microscopy

TEM Transmission Electron Microscopy

TNT Titanate nanotube

TNT-Co Cobalt intercalated titanate nanotube

TNW Titanate nanowire

TNW-Co Cobalt intercalated titanate nanowire

XPS X-ray photoelectron spectroscopy

List of Figures

| | | |
|-----|--|----|
| 1.1 | The crystal structure of sodium titanate; the black framed area shows the unit cell of the structure. This model is made using VESTA. | 2 |
| 1.2 | Schematic showing the scrolling of the layered titanates to form nanotubes Liu et al. (2016) | 3 |
| 2.1 | Schematic representation of the synthesis of the Co doped TNT and TNW | 7 |
| 2.2 | Schematic representation of the synthesis of the Co intercalated TNT and TNW | 7 |
| 2.3 | The list of samples analysed in this study | 8 |
| 3.1 | Ray diagram of a conventional TEM Holsgrove (2017) | 14 |
| 3.2 | Varying the strength of the intermediate lens can either form a diffraction pattern or an image Williams and Carter (2009) | 15 |
| 3.3 | SAED pattern from single crystalline, polycrystalline and amorphous specimen (Ammrf) | 18 |
| 3.4 | Schematic showing how the objective lens and objective aperture are used in combination to produce BF image, DF image and CDF image. (Deepak et al., 2018) | 19 |
| 3.5 | A schematic diagram of the optical path for STEM. Deepak et al. (2018) . | 20 |
| 3.6 | A schematic diagram of HAADF-STEM and ABF-STEM techniques Deepak et al. (2018) | 21 |
| 3.7 | Titan ChemiSTEM | 23 |
| 3.8 | a). Schematic representation of X-ray generation by e beam irradiation. Deepak et al. (2018) b) A typical EDX spectrum | 24 |

| | | |
|------|--|----|
| 3.9 | Schematic showing how an EELS spectrometer is coupled with a TEM with its components along with the ray diagram showing how a magnetic prism spectrometer disperses and focusses the no-loss and energy-loss electrons in the image plane of the spectrometer Williams and Carter (2009) | 26 |
| 3.10 | A schematic of electron generation by X ray | 27 |
| 3.11 | A schematic of XPS instrumentation | 28 |
| 3.12 | An XPS spectrometer - KRATOS | 28 |
| 3.13 | A schematic of Raman spectroscopy instrumentation Gouadec and Colomban (2007). | 29 |
| 3.14 | Raman spectrometer - Jobin-Yvon T64000 | 31 |
| 4.1 | STEM BF image (left) and HAADF image (right) showing the morphology of TNW | 33 |
| 4.2 | STEM BF image (left) and HAADF image (right) of TNW showing the layers | 33 |
| 4.3 | EDX mapping of TNW | 34 |
| 4.4 | EDX spectrum and quantification results of TNW | 34 |
| 4.5 | STEM HAADF image (left) and BF image (right) showing morphology of TNT | 35 |
| 4.6 | STEM HAADF image (left) and BF image (right) showing interlayers of TNT | 35 |
| 4.7 | EDX mapping of TNT | 35 |
| 4.8 | EDX spectrum and quantification results of TNT | 36 |
| 4.9 | STEM BF image (left) and HAADF image (right) of Co(1%) TNW. | 37 |
| 4.10 | STEM BF image (left) and HAADF image (right) showing the layered structure of Co(1%) TNW. | 37 |
| 4.11 | EDX mapping of Co(1%) TNW. | 37 |
| 4.12 | EDX spectrum and quantification of Co(1%) TNW. | 38 |
| 4.13 | Interlayer spacing and diameter distribution of Co(1%) TNW. | 38 |
| 4.14 | Low magnification images of the Co(5%) TNW sample. | 39 |
| 4.15 | High magnification images of the Co(5%) TNW sample. | 39 |
| 4.16 | EDX maps on a single nanotube of the Co(5%) TNW sample. | 40 |
| 4.17 | EDX spectrum and quantification form Co(5%) TNW sample. | 40 |
| 4.18 | STEM BF image (left) and HAADF image (right) of TNW Co(5%) | 41 |

| | |
|---|----|
| 4.19 High magnification STEM BF image (left) and HAADF image (right) of TNW Co(5%). | 41 |
| 4.20 EDX map on a single wire of TNW Co(5%). | 42 |
| 4.21 EDX spectrum and quantification of TNW Co(5%). | 42 |
| 4.22 Diameter and interlayer spacing measured in TNW Co(5%) sample. | 42 |
| 4.23 STEM BF image (left) and HAADF image (right) of Co(1%)-TNT | 43 |
| 4.24 High magnification STEM BF image (left) and HAADF image (right) of Co(1%)-TNT. | 44 |
| 4.25 EDX map of Co(1%)-TNT. | 44 |
| 4.26 EDX spectrum and quantification of Co(1%)-TNT. | 44 |
| 4.27 STEM BF image (left) and HAADF image (right) of Co(2.5%)-TNT. | 45 |
| 4.28 High magnification STEM BF image (left) and HAADF image (right) of Co(2.5%)-TNT. | 45 |
| 4.29 EDX map of Co(2.5%)-TNT. | 46 |
| 4.30 EDX spectrum and quantification of Co(2.5%)-TNT. | 46 |
| 4.31 Interlayer spacing, outer diameter and inner diameter of Co(2.5%)-TNT. | 46 |
| 4.32 STEM BF image (left) and HAADF image (right) of Co(5%)-TNT. | 47 |
| 4.33 High magnification STEM BF image (left) and HAADF image (right) of Co(5%)-TNT. | 47 |
| 4.34 Low magnification and HR TEM images of Co(5%)-TNT. | 48 |
| 4.35 EDX map of Co(5%)-TNT. | 48 |
| 4.36 EDX spectrum and quantification of Co(5%)-TNT. | 48 |
| 4.37 Interlayer spacing, outer diameter and inner diameter of Co(5%)-TNT. | 49 |
| 4.38 STEM BF image (left) and HAADF image (right) of TNT-Co(1%). | 49 |
| 4.39 High magnification STEM BF image (left) and HAADF image (right) of TNT-Co(1%). | 50 |
| 4.40 EDX map of TNT-Co(1%). | 50 |
| 4.41 EDX spectrum and quantification of TNT-Co(1%). | 51 |
| 4.42 STEM BF and HAADF images of TNT-Co(2.5%). | 51 |
| 4.43 High magnification STEM BF image (left) and HAADF image (right) of TNT-Co(2.5%). | 52 |
| 4.44 EDX map of TNT-Co(2.5%). | 52 |
| 4.45 EDX spectrum and quantification of TNT-Co(2.5%). | 52 |
| 4.46 STEM BF image (left) and HAADF image (right) of TNT-Co(5%). | 53 |

| | |
|--|----|
| 4.47 High magnification STEM BF image (left) and HAADF image (right) of TNT-Co(5%). | 53 |
| 4.48 HRTEM images of TNT-Co(5%). | 54 |
| 4.49 EDX mapping of TNT-Co(5%). | 54 |
| 4.50 Spectrum and quantification of TNT-Co(5%). | 55 |
| 4.51 Interlayer spacing, outer diameter and inner diameter of TNT-Co(5%). | 55 |
| 4.52 Comparison between the doped and intercalated nanostructures: Interlayer spacing and diameter | 56 |
| 4.53 EDS quantification of doped and intercalated titanate nanostructures | 56 |
| 4.54 EELS signal extraction: figure shows spectrum background, edge and the cross section Gatan | 57 |
| 4.55 Background modelling Gatan | 57 |
| 4.56 EELS elemental mapping of Co(5%)-TNW sample. | 58 |
| 4.57 EELS spectrum and quantification details of intercalated TNT-Co(5%) | 59 |
| 4.58 EELS spectrum and quantification of intercalated TNT-Co(5%) | 59 |
| 4.59 EELS spectrum and quantification of intercalated TNW-Co(5%) | 60 |
| 4.60 EELS spectra of TNW-Co(5%) | 60 |
| 4.61 Co L_3/L_3 ratio (Pearson et al., 1988). | 61 |
| 4.62 Co L_3/L_3 ratio | 62 |
| 4.63 Co $L_{2,3}$ edge of cobalt(5%) intercalated and doped titanate nanowires | 62 |
| 4.64 Co L_3/L_3 ratio Wang et al. (2000) | 62 |
| 4.65 Co2p XPS spectra of doped Co(5%)-TNT and Co(5%)-TNW | 63 |
| 4.66 Co2p XPS spectra of intercalated TNT-Co(5%) and TNW-Co(7.5%) | 64 |
| 4.67 XPS quantification results of intercalated TNW's and TNT's | 64 |
| 4.68 XPS quantification result of (5% cobalt) doped TNT and TNW | 65 |
| 4.69 Raman spectra of titanate nanotube (TNT) and doped and intercalated titanate nanotube | 65 |
| 4.70 Raman spectra of titanate nanowire(TNW) and doped and intercalated titanate nanowires | 67 |

Contents

| | |
|---|-----------|
| List of Figures | xi |
| 1 Introduction | 1 |
| 1.1 An overview | 1 |
| 1.2 Outline of the thesis | 3 |
| 2 Synthesis and Characterization of Samples | 5 |
| 2.1 Synthesis | 5 |
| 2.1.1 Synthesis of the TNT/TNW amorphous precursor | 5 |
| 2.1.2 Synthesis of Co doped TNT/TNW amorphous precursor | 5 |
| 2.1.3 TiO ₂ and Co-TiO ₂ Nanoparticle Synthesis | 6 |
| 2.1.4 TNW and Co-TNW synthesis | 6 |
| 2.1.5 TNT and Co-TNT synthesis | 6 |
| 2.1.6 Co-intercalated TNW and TNT synthesis | 6 |
| 2.1.7 Samples analysed in this study | 8 |
| 2.2 Characterization details | 8 |
| 2.2.1 Electron Microscopy | 8 |
| 2.2.2 XPS | 9 |
| 2.2.3 Raman | 9 |
| 3 Characterization Techniques | 11 |
| 3.1 Transmission Electron Microscopy | 11 |
| 3.1.1 Overview of Transmission Electron Microscopy | 11 |
| 3.1.2 Electron Optics in the TEM | 13 |
| 3.1.3 Aberrations | 14 |
| 3.1.4 Beam Sample Interactions | 16 |
| 3.1.5 Electron Diffraction | 16 |

| | | |
|----------|--|-----------|
| 3.1.6 | Image | 17 |
| 3.1.7 | Bright Field and Dark Field Imaging | 18 |
| 3.1.8 | High Resolution Transmission Electron Microscopy (HRTEM) | 19 |
| 3.1.9 | Scanning Transmission Electron Microscopy (STEM) | 20 |
| 3.1.10 | Aberration Corrected TEM/STEM | 22 |
| 3.1.11 | Spectroscopic Techniques in TEM | 23 |
| 3.2 | X-ray photoelectron spectroscopy (XPS) | 25 |
| 3.3 | Raman spectroscopy | 27 |
| 4 | Results and Discussions | 32 |
| 4.1 | Electron Microscopy of TNW and TNT | 32 |
| 4.1.1 | TNW | 32 |
| 4.1.2 | TNT | 32 |
| 4.2 | Electron microscopy of Co doped titanate nanowires | 36 |
| 4.2.1 | Co(1%)-TNW | 36 |
| 4.2.2 | Co(5%)-TNW | 36 |
| 4.3 | Co Intercalated titanate nanowires | 39 |
| 4.3.1 | TNW-Co(5%) | 41 |
| 4.4 | Co doped titanate nanotubes | 43 |
| 4.4.1 | Co(1%)-TNT | 43 |
| 4.4.2 | Co(2.5%)-TNT | 43 |
| 4.4.3 | Co(5%)TNT | 45 |
| 4.5 | Co intercalated titanate nanotubes | 47 |
| 4.5.1 | TNT-Co(1%) | 47 |
| 4.5.2 | TNT-Co(2.5%) | 49 |
| 4.5.3 | TNT-Co(5%) | 51 |
| 4.6 | Comparison between the doped and intercalated nanostructures | 56 |
| 4.7 | EELS Analysis | 56 |
| 4.7.1 | EELS elemental mapping | 58 |
| 4.7.2 | EELS quantification | 58 |
| 4.8 | Cobalt valence in titanate nanostructures by EELS | 59 |
| 4.9 | X-ray photoelectron spectroscopy | 63 |
| 4.10 | Raman spectroscopy | 65 |
| 5 | Conclusions | 68 |

Chapter 1

Introduction

1.1 An overview

Nanostructures have been the focus of research in the past few decades due to their unique properties. An important application which nanomaterials could find is in the field of catalysis. The high surface area unique to nanomaterials is the main reason behind this. Among various catalysis, photocatalysis for degradation of organic pollutants holds an important position in the current era as it is important to maintain a clean environment [Matsuoka and Anpo \(2010\)](#). Titanium oxide, TiO_2 , is the most extensively used semiconducting catalyst for this application due to its properties such as low toxicity, earth abundance and strong oxidizing abilities for the decomposition of organic pollutants [Schneider et al. \(2014\)](#) [Nakata and Fujishima \(2012\)](#). The photocatalytic properties of TiO_2 are derived from the formation of photogenerated charge carriers (hole and electron) which occurs upon the absorption of ultraviolet light corresponding to the band gap. The photocatalytically active polymorphs, anatase and rutile, have a band gap of 3.2 eV and 3 eV, respectively. In addition to the photocatalytic decomposition of organic pollutants, it is an important material in the field of energy production, viz., photocatalytic water splitting, dye sensitized/quantum dot sensitized solar cells and batteries [Hashimoto et al. \(2005\)](#) [McDaniel et al. \(2013\)](#) [Li et al. \(2015\)](#). Nanotubular TiO_2 is an important morphology as it reduces the recombination of holes and electrons generated by photo-absorption as the half-thickness of the nanotube wall is less than the carrier diffusion length in TiO_2 [Bavykin and Walsh \(2009\)](#). The TiO_2 nanotube arrays consequently have the potential to achieve higher photocatalytic activity for the decomposition of organic pollutants. The general approaches to the synthesis of TiO_2 nanotubes are chemical (template) synthesis, electrochemical approaches (e.g., anodizing

of Ti), and the alkaline hydrothermal method [Bavykin and Walsh \(2009\)](#)[Sergiu P. Albu et al. \(2007\)](#). Titanate nanotubes (TNTs), such as that of $\text{Na}_2\text{Ti}_3\text{O}_7$, are investigated as alternatives to TiO_2 , as they combine the properties of TiO_2 nanoparticles with the properties of layered titanates such as cation exchange ability and open mesoporous morphology with higher specific surface area [Bavykin and Walsh \(2009\)](#). The most common synthesis method for titanate nanotubes involve alkaline hydrothermal synthesis with Ti precursors, for example, TiO_2 nanoparticles. This has the benefit that it is a single step synthesis method and relatively low hydrothermal temperatures are sufficient to achieve an essentially complete conversion of the initial raw materials to titanate nanotubes. Titanates consist of sheets of TiO_6 octahedra with H^+ or cations such as Na^+ in the interlayer space as shown in [Figure 1.1](#). [Figure 1.2](#) shows a schematic representation of the scrolling of the layered titanate to form nanotube.

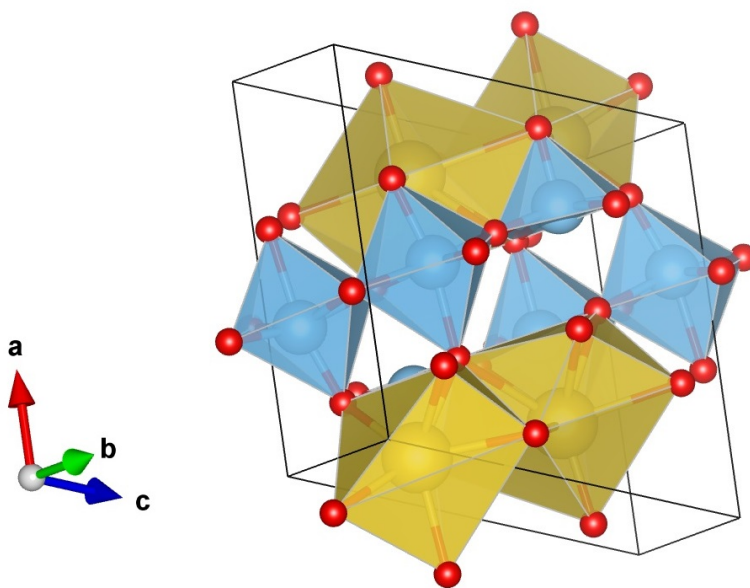


Figure 1.1: The crystal structure of sodium titanate; the black framed area shows the unit cell of the structure. This model is made using [VESTA](#).

Since TNTs have good ion-exchange properties, one method of catalyst deposition involves preliminary ion-exchange of catalyst precursor in the cationic form with protons within nanotubular titanates. This allows atomic-scale distribution of metal cations in the titanate lattice, achieving higher metal loading relative to adsorption of the precursor on the surface.

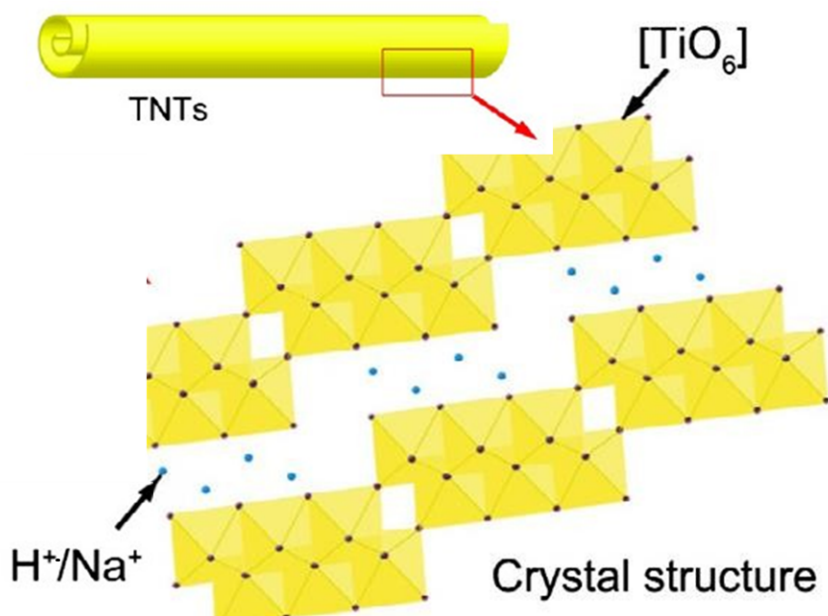


Figure 1.2: Schematic showing the scrolling of the layered titanates to form nanotubes [Liu et al. \(2016\)](#)

1.2 Outline of the thesis

In the case of titanate nanotubes and nanowires, the main challenge is the precise determination of structure. The exact determination of crystal structures of nanotubes as well as their exact stoichiometry is still incomplete because of several intrinsic difficulties posed by the nanostructures, including their small crystallite size and the wrapping of the structures along a certain crystallographic axis, both resulting in broadening of the diffraction signals. The low weight of hydrogen atoms also results in difficulties in locating their precise positions and population inside the crystals. The introduction of additional cations to generate catalytic properties results in an increase in the level of complexity. The structure, composition and morphology of the material play a significant role in their catalytic activity. In this context, this study is aimed at employing a combination of techniques including electron microscopy, Raman and X-ray photoelectron spectroscopy (XPS) to determine the morphology, composition and structure of the titanate nanostructures and also to estimate the various aspects of transition metal dopant/intercalant in the titanate nanostructures. The samples under consideration are cobalt modified TNTs and TNWs which are prepared by cation exchange of the hydrothermally synthesized TNTs and TNWs as well as doped TNTs and TNWs. Recently spectroscopic investigations using XPS and Raman spectroscopy on cobalt modified TNT samples showed that the presence of the Co cations and its concentration

influences the optical and photocatalytic properties ([Barrocas et al., 2016](#)). Photocatalytic experiments using a mixture of three organic pollutants showed that Co doped TNTs and ion exchanged TNTs are better catalysts compared to pristine TNTs although the catalytic activities were different for the cation exchanged and doped TNTs.

In the present project it is expected that a detailed experimental study using such techniques would provide new insights into the structural and compositional aspects which influences the catalytic properties.

Chapter 2

Synthesis and Characterization of Samples

2.1 Synthesis

The samples for this study were provided by Dr. Beatriz Barrocas and Prof. Olinda C. Monteiro from Center for Chemistry and Biochemistry and Center for Structural Chemistry, Faculty of Sciences, University of Lisbon, Portugal. The synthesis methods employed are given below.

2.1.1 Synthesis of the TNT/TNW amorphous precursor

Titanate nanotubes (TNT) and titanate nanowires (TNW) samples were prepared from an amorphous precursor. This amorphous precursor was prepared using a reported procedure [Bem et al. \(2012\)](#), [Barrocas et al. \(2016\)](#). In short, TiCl_3 solution (20 wt.% in 20–30 wt.% HCl) diluted in a ratio of 1:2 in 2 M HCl solution was prepared. To this solution, a 4 M NH_4OH solution was added drop-by-drop under vigorous stirring, until complete precipitation of a white solid. This suspension was kept overnight at room temperature. The product was filtered and washed with distilled water several times. The white precursor thus obtained was used to directly produce the TNW sample. This precursor was also utilized to prepare TiO_2 nanoparticles that were further used for TNT synthesis.

2.1.2 Synthesis of Co doped TNT/TNW amorphous precursor

To synthesize a Co doped TNT precursor, the required molar amount (5%) of cobalt is added to the titanium trichloride solution using the following procedure: 0.170 g of

metallic cobalt powder was dissolved in ca. 1 mL of conc. HNO_3 . The deep purple solution obtained was heated to evaporate the solvent and ca. 2mL of HCl (37%) solution was added to evaporate the residual nitrates formed. Then the solution was diluted with 2 M HCl to obtain a 100 mL of final volume. This solution was added to the 50 mL of the titanium trichloride solution. This on precipitation with the 4M ammonia solution gives the CoTNT precursor as a greenish grey solid.

2.1.3 TiO_2 and Co- TiO_2 Nanoparticle Synthesis

As previously reported ([Barrocas et al., 2016](#)), the crystallization of the precursor to obtain TiO_2 nanoparticles was performed in an autoclave at 200°C , for 6 h in an aqueous suspension. After being washed, the TiO_2 nanoparticles or the CoTiO_2 nanoparticles were dried and stored.

2.1.4 TNW and Co-TNW synthesis

The samples were synthesized using a hydrothermal approach. The syntheses was performed in an autoclave system (160°C , 24 hours) using 10 g of amorphous precursor in ca. 70 mL of a NaOH 10 M aqueous solution. After cooling until room temperature, the powders were washed several times with water until the pH of the filtrate solution was 7, and afterwards dried at 60°C

2.1.5 TNT and Co-TNT synthesis

The samples were synthesized using a hydrothermal approach. The syntheses were performed in an autoclave system (160°C , 24 hours) using 10 g of the previously prepared TiO_2 sample (for the TNT) and 10 g of the previously prepared Co- TiO_2 (for CoTNT synthesis) in ca. 70 mL of a NaOH 10 M aqueous solution. After cooling until room temperature, the powders were washed several times with water until the pH of the filtrate solution was 7, and afterwards dried at 60°C [Ferreira et al. \(2013\)](#)

2.1.6 Co-intercalated TNW and TNT synthesis

The Co-intercalated titanate nanotubes were synthesized by adding the required amount of Co to 1 g of TNT or TNW in 60 mL of cobalt nitrate aqueous solution. The resulting suspension was stirred for 7 h at room temperature. Further, the suspensions were

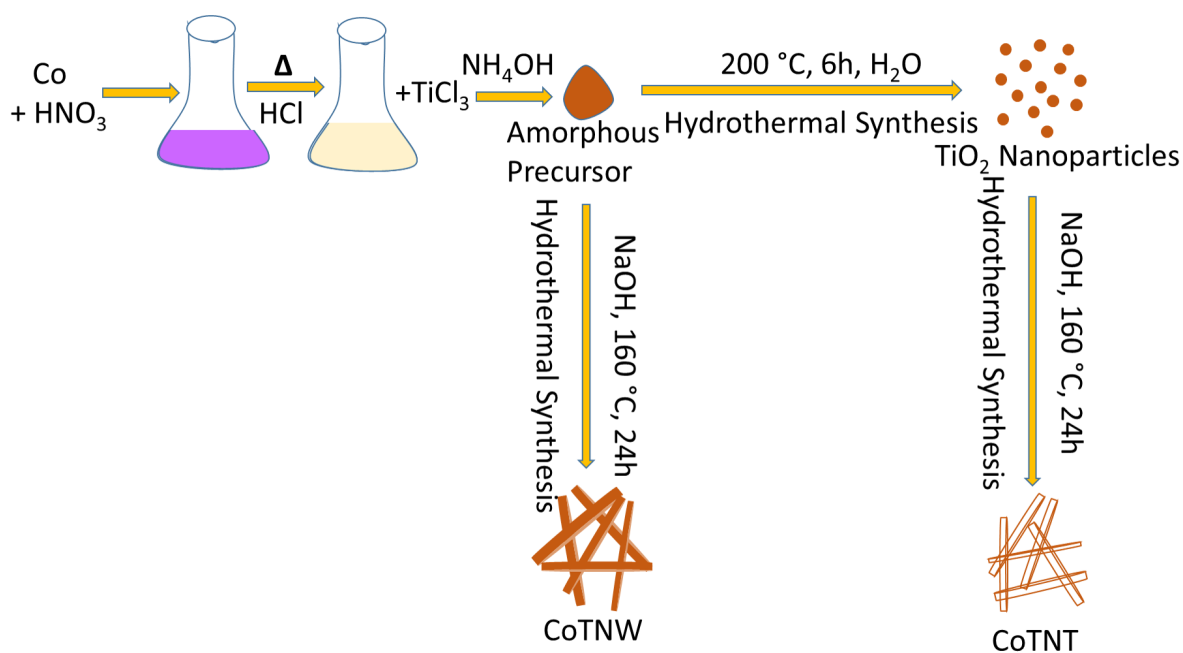


Figure 2.1: Schematic representation of the synthesis of the Co doped TNT and TNW

thoroughly rinsed with deionized water to remove the remaining cobalt ions. The obtained Co intercalated sample was identified as TNT/Co(5%) or TNW/Co(5%). Afterwards, the solids were dried and stored [Barrocas et al. \(2016\)](#)

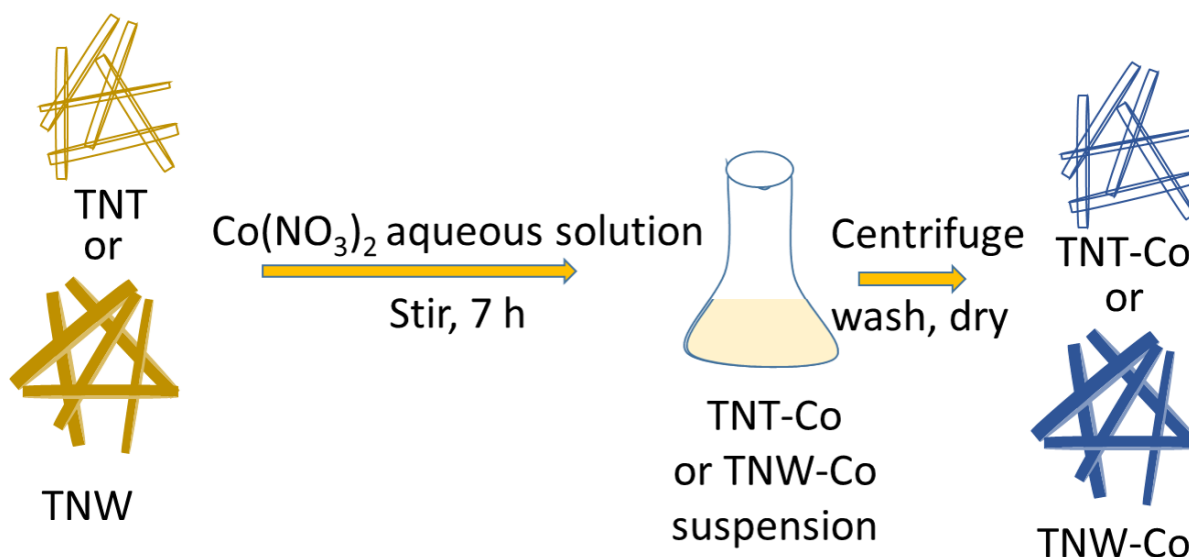


Figure 2.2: Schematic representation of the synthesis of the Co intercalated TNT and TNW

2.1.7 Samples analysed in this study

The samples which were analysed in this study are shown in the table below in figure 2.3. The samples include, reference titanate nanowires and titanate nanotubes, cobalt doped titanate nanowires and titanate nanotubes, and intercalated cobalt titanate nanotubes and titanate nanowires.

| 1 st Set | 2 nd Set | 3 rd Set | 4 th Set | 5 th Set |
|---------------------|---------------------|---------------------|---------------------|---------------------|
| TNT | Co(5%)-TNT | TNW-Co(1%) | TNT | Co(5%)-TNT |
| Co(1%)-TNT | TNW | TNW-Co(2.5%) | TNT-Co(1%) | Co(5%)-TNW |
| Co(5%)-TNT | Co(1%)-TNW | TNW-Co(5%) | TNT-Co(2.5%) | Co(2.5%)-TNT |
| TNT-Co(5%) | Co(5%)-TNW | TNW-Co(7.5%) | TNT-Co(5%) | TNW-Co(5%) |
| | | TNW-Co(10%) | TNT-Co(7.5%) | |
| | | | TNT-Co(10%) | |
| | | | Co(1%)-TNT | |
| | | | Co(5%)-TNT | |

TNT : Titanate nanotubes **Co-TNT** : Co doped titanate nanotubes
TNW : Titanate nanowires **TNT-Co** : Co intercalated titanate nanotubes
Co-TNW : Co doped titanate nanowires
TNW-Co : Co intercalated titanate nanowires

Figure 2.3: The list of samples analysed in this study

2.2 Characterization details

2.2.1 Electron Microscopy

Transmission Electron Microscopy (TEM) and Scanning Transmission Electron Microscopy (STEM) were performed on a Titan ChemiSTEM with probe Cs corrector and Titan Themis 80-300 microscopes with probe and image Cs corrector and monochromator. Samples for electron microscopy were prepared by dispersing the powder in distilled water by ultrasonication and drying a drop of this dispersion onto a lacey carbon supported Cu grid. Necessary measures were taken to minimise the contamination during imaging, including heating the samples (> 120 min) under controlled temperature (> 45°C-60°C) in a vacuum chamber, followed by plasma cleaning to remove any left out hydrocarbons and also by carrying out electron microscopy work at a lower accelerating voltage. All the electron microscopy work reported were carried out at 80 kV.

Scanning Transmission Electron Microscopy (STEM) was performed using spot size 7

with a probe current of ~ 130 pA at a convergence angle, α of 21 mrad.

Electron Energy Loss Spectroscopy (EELS) was performed in STEM mode using the same experimental conditions on a GIF quantum spectrometer with a collection angle, β of ~ 5 mrad. The EELS spectrum was acquired with an exposure of 0.2s, summed to 200 frames with a total sum time of 40s with gain normalisation.

EDX was acquired on a SuperX EDX detector attached to this microscope. The EDX maps in STEM mode were acquired by recording the spectrum at each pixels while scanning a region of interest. The total times for acquiring maps was approximately 5 min. Bruker Esprit software was used for acquisition and analysis.

2.2.2 XPS

XPS spectra were recorded on a Kratos axis ultra HSA using monochromatic Al X-ray (1486.6 eV). The high voltage used is 15kV(90W). Charge neutralizer was on during the acquisition. The spectra were analysed with integral peak measurements, without modelling the structure, and with a simple background model (Shirley). This facility is part of CEMUP, University of Porto.

XPS spectra were also recorded on a ESCALAB 250Xi X-ray Photoelectron Spectrometer (XPS) Microprobe with a monochromated micro-focused Al K-Alpha at INL.

2.2.3 Raman

Jobin-Yvon T64000 has a triple-monochromator spectrometer and has the possibility of using micro and macroanalysis systems. In the microanalysis system the laser beam is focused on the surface of the sample through a microscope lens (Olympus BH2-UMA), in an area of the order of 3-4 μm^2 and in backscattering geometry (the incident and scattered beams make an angle of $\sim 180^\circ$ between each other) screen (AH-SPS) which allows visualization of the micro-region of the sample which was focussed. Raman scattered spectra were obtained using the most intense stripes of Argon laser (Coherent Innova 92 Ar +) of wavelength 514 nm. When the laser was on the sample surface, to avoid increase in temperature, laser power was kept below 0.5 to 5 mW. All the spectra were obtained in micro-Raman and at room temperature ($T = 21^\circ\text{C}$), and under the conditions used, the resolution is approximately 1 cm^{-1} .

Raman measurements was also done in backscattering configuration at room

temperature with a Horiba Jobin-Yvon HR800 UV spectrometer at the Department of Physic and i3N, University of Aveiro.

Chapter 3

Characterization Techniques

3.1 Transmission Electron Microscopy

Transmission electron microscopy is a powerful tool to characterize nanostructures. In this section, an overview of the transmission electron microscope is described, with emphasis on various imaging modes and spectroscopy techniques used in this study.

One of the reasons for characterizing materials by transmission electron microscopy (TEM) is because of the high spatial resolution as well as analytical resolution. This is a unique technique where structural, morphological and chemical information from the same region can be obtained with high spatial resolution down to atomic scale.

3.1.1 Overview of Transmission Electron Microscopy

A transmission electron microscope (TEM) is an instrument for imaging specimens at high resolutions. It uses a beam of electrons accelerated to sufficient energy so that when incident on a very thin sample (<100nm), electrons are transmitted through it. Conventional TEM work on the same principle as light microscopes but utilise a beam of electrons, rather than using a light source. The first TEM was built by Ernst Ruska and Max Knoll in 1931 ([Williams and Carter, 2009](#)). The invention of the TEM resulted in superior resolution in imaging beyond that could be achieved by optical microscope. Due to the limitations of using light for imaging, optical microscopes are constrained by the resolution and diffraction limits of the wavelengths of visible light.

For any optical system, the theoretical diffraction limited resolution, d_0 , is given by Rayleigh's criterion [3.1](#). This criterion describes the smallest resolvable distance between two points. λ is the wavelength of the illuminating source and NA is the numerical

aperture($NA = n \sin \theta$ where n is the refractive index of the medium and θ is the collection semiangle).

$$d_0 = \frac{0.61\lambda}{NA} \quad (3.1)$$

From equation (3.1), it can be seen that d_0 is proportional to wavelength and therefore to improve the resolution an illumination source with a shorter wavelength can be employed, such as electrons. de Broglies relation gives the relation between the wavelength of the electron and its momentum as given below.

$$\lambda = \frac{h}{p} = \frac{h}{mv} \quad (3.2)$$

where λ is the de Broglie wavelength, h is Plancks constant, p is the momentum, m is the mass and v is the velocity. Therefore, by increasing the momentum of an electron beam its wavelength can be decreased. Thus by employing electrons accelerated by high potential difference a resolution limit above that attainable by visible light can be achieved. In the TEM, when an electron (with charge e) passes through a potential difference V , its kinetic energy will be equal to the energy of the field i.e. eV (energy in electron volts)

$$\frac{mv^2}{2} = eV \quad (3.3)$$

Substituting a rearranged version of (3.2) into (3.3), gives:

$$\frac{1}{2} m \left(\frac{h}{m\lambda} \right)^2 = eV \quad (3.4)$$

And rearranging (3.4) gives the non-relativistic electron wavelength:

$$\lambda = \frac{h}{p} = \frac{h}{(2meV)^{1/2}} \quad (3.5)$$

However, relativistic effects cannot be ignored because at an accelerating voltage of 100 kV , the velocity of electrons is greater than half the speed of light. To account for this, we consider the relativistic form of the kinetic energy, E_k :

$$E_k = mc^2 - m_0c^2 \quad (3.6)$$

where m_0 is the rest mass of an electron and c is the speed of light. As the kinetic energy is determined by the accelerating voltage ($E_k = eV$) m can be given by:

$$m = \frac{eV + m_0c^2}{c^2} \quad (3.7)$$

Substituting (3.7) for m in (3.5) gives the relativistic electron wavelength:

$$\lambda = \frac{h}{[2m_0eV(1 + \frac{eV}{2m_0c^2})]^{1/2}} \quad (3.8)$$

For a TEM operating with an accelerating voltage of 200 kV, the theoretical wavelength of the electrons will be 2.51 pm, much smaller than the wavelength of visible light (400 nm for blue light). Hence, the electron beam can reach a theoretical resolution limit smaller than atoms themselves. However, due to the aberrations which are present in the optics of a TEM, the resolution obtained in TEM is much lower than that of the theoretical resolution.

The main components of the TEM are shown schematically, along with the ray diagram, in figure 3.1. The main components are: the electron gun (source of electrons); condenser lenses (electromagnetic lenses to collimate the beam); objective lens (to focus and initially magnify the image); apertures (to limit the diameter of the electron beam); intermediate lens; projector lens; viewing screen and detectors to collect the signals. The important parameters which determine the nature and the quality of the image or spectrum obtained with a TEM, are the probe size, convergent angle, electron energy and the electron probe current [Williams and Carter \(2009\)](#).

3.1.2 Electron Optics in the TEM

In a TEM, the first set of electromagnetic lenses that the electrons pass through after emission from the gun are the condenser lenses, C1 and C2. The C1 lens controls the spot size of the beam, creating a crossover of the electrons from the gun lens. The C2 lens controls the convergence angle of the beam and can be used to create a parallel or a convergent beam depending on the mode of operating the TEM. The next set of electromagnetic lenses that the electrons pass through in the TEM are the objective lenses. The sample is located in between the upper and lower pole pieces of the objective lens. The purpose of the objective lens is to focus the beam onto the sample and to form an initial inverted image of the sample.

The intermediate lens further down the TEM column is used to magnify the initial image formed by the objective lens onto the viewing screen (imaging mode), or project

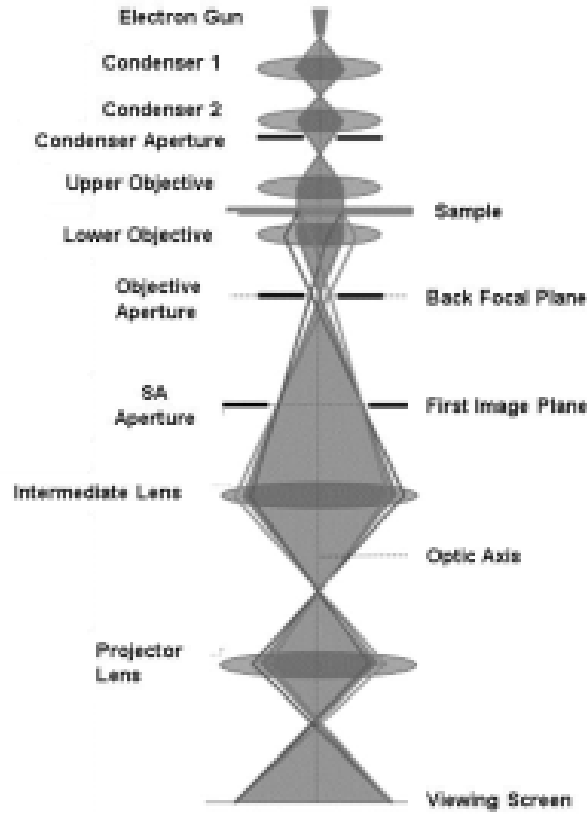


Figure 3.1: Ray diagram of a conventional TEM [Holsgrove \(2017\)](#)

the diffraction pattern formed on the back focal plane (BFP) of the objective lens onto the viewing screen (diffraction mode), shown schematically in figure 3.2

3.1.3 Aberrations

There are many kinds of lens defects affecting the performance of the TEM. The most significant are spherical aberration, chromatic aberration and astigmatism. In an ideal TEM (or any optical system) every point on the object will be reproduced in the image, but in reality the electrons which are closer to the optical axis are not focused to the same point as electrons further from the optical axis. This defect within the electromagnetic lenses is known as spherical aberration (C_s). The diameter of the spherically distorted disk of intensity d_{sph} in terms of the collection semiangle of the lens, β , and the spherical aberration coefficient, C_s , of the lens can be written as [Williams and Carter \(2009\)](#):

$$d_{sph} = \frac{1}{2} C_s \beta^3 \quad (3.9)$$

Chromatic aberration C_c , arises due to the electron beam not being monochromatic. This spread of energies in the electrons may be due to fluctuations in the gun voltage

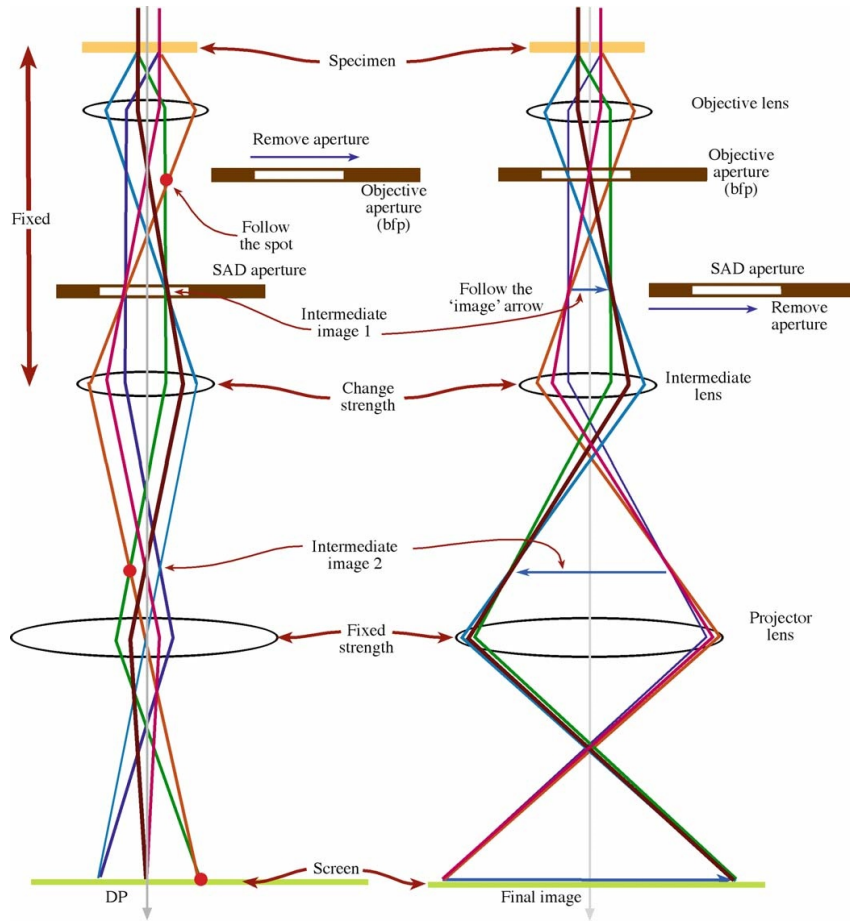


Figure 3.2: Varying the strength of the intermediate lens can either form a diffraction pattern or an image [Williams and Carter \(2009\)](#)

causing an energy spread in the electrons leaving the source, or, different energy losses due to interactions with the sample. Like spherical aberration, the diameter of the chromatic disc of least confusion, d_{chr} , can be expressed as:

$$d_{chr} = C_c \left(\frac{\Delta E}{E_0} \right) \beta^3 \quad (3.10)$$

Where ΔE is the energy loss, E_0 the incident energy and C_c is the chromatic aberration coefficient of the lens [Williams and Carter \(2009\)](#). Chromatic aberrations in a lens results in electrons of different energies being brought to focus at different points along the optic axis. Astigmatism is another type of aberration in the TEM which occurs when electrons sense a non-uniform magnetic field as they spiral down the electron column. Astigmatism arises due to defects in the soft-iron pole pieces, which is practically impossible to machine to be of perfectly cylindrically symmetric, or due to contamination on apertures causing charge build up which deflect the beam [Williams and Carter \(2009\)](#). Astigmatism can distort the image by an amount d_{ast} given by:

$$d_{ast} = \beta \Delta f \quad (3.11)$$

Where Δf is the maximum difference in focus induced by the astigmatism. Astigmatism is easily corrected by using stigmators, which are small octupoles that introduce a compensating field to balance out the inhomogeneities in the magnetic field.

The effect of C_s and C_c can be overcome by using aberration correctors which will be discussed later.

3.1.4 Beam Sample Interactions

As the accelerated electrons are passed through the sample various interactions can occur. Firstly, an electron may pass through the sample unchanged. However, most likely the electrons will be scattered by the Coulomb forces generated by the nuclei and orbiting electrons of the sample. These electrons can either be scattered elastically (meaning that the energy lost by the primary electron is either zero or too small to be detected) or inelastically (meaning the energy loss of the primary electron big enough to be detected in the microscope). Elastic scattering occurs mainly from interactions with atomic nuclei (or the whole electrostatic field of the atom) and is responsible for diffraction from crystalline samples, used to extract structural information of a specimen. Meanwhile, inelastic scattering mainly involves electron-electron interactions and can be exploited for chemical analysis, for example by electron energy loss spectroscopy (EELS). The inelastic scattering of a primary electron also leads to the generation of X-rays which can be detected using energy dispersive X-ray (EDX) detectors to obtain the composition of a specimen.

3.1.5 Electron Diffraction

Electron diffraction is the result of Bragg scattering as the electron beam passes through a crystalline sample. Crystals act as three-dimensional gratings allowing the waves (electrons) to be scattered from the lattice planes separated by lattice constant, d . When the scattered waves interfere constructively, they remain in phase and the path difference between the two waves undergoing interference is given by Bragg's law:

$$2d_{hkl} \sin \theta \approx n\lambda \quad (3.12)$$

where θ is the scattering angle of the wave and n is the integer multiple of the wavelength (or order of reflection). The collective effect of scattering from successive crystallographic planes of the crystal lattice (described by Miller notation, hkl) increases the amount of constructive interference and intensifies the resultant reflections in the diffraction pattern (DP). DP is angular distribution of scattered electrons. In TEM, an aperture (metal strip with holes to limit the beam size) can be inserted to generate a DP from a selected area of the sample (called selected area electron diffraction, SAED). The distance in reciprocal space, r_{hkl} , between a particular reflection and the reflection from the direct beam (000) is related to the interplanar distance as:

$$\frac{r_{hkl}}{L} = \tan 2\theta \quad (3.13)$$

Selected Area Electron Diffraction

Most of the forward scattering signals can be used to form a selected area diffraction pattern in screen or CCD by using a selected area aperture in the TEM. Based on the selected area diffraction pattern (SAEDP) obtained in the TEM, we can identify the crystalline nature (single crystal, polycrystalline, amorphous) of the specimen, figure 3.3. SAED can be used to obtain the crystallographic information of the specimen. However, there are two severe limitations when we try to use the SAEDP. One is that we have to be very cautious in interpreting SADPs from areas which are $< \sim 500$ nm in diameter because the information in the pattern may not be limited to that region. For an intermediate-voltage high resolution TEM with a very low spherical aberration (Cs), the region analyzed by SAED may be limited to $< \sim 100$ nm in diameter, which is still too large for examining many nanoscale systems, such as, nanoscale particles, defects in crystal, thin films as well as secondary phase precipitates which have an important influence on the properties of materials. Another limitation is that the SADPs contain only rather imprecise 2D crystallographic information because the Bragg condition is relaxed for thin specimens Williams and Carter (2009) Deepak et al. (2018).

3.1.6 Image

The spacial distribution of scattered electron is seen as contrast in images. The electron wave can change both its amplitude and its phase as it passes through the specimen and this can give rise to image contrast. Generally, two kinds of images can be

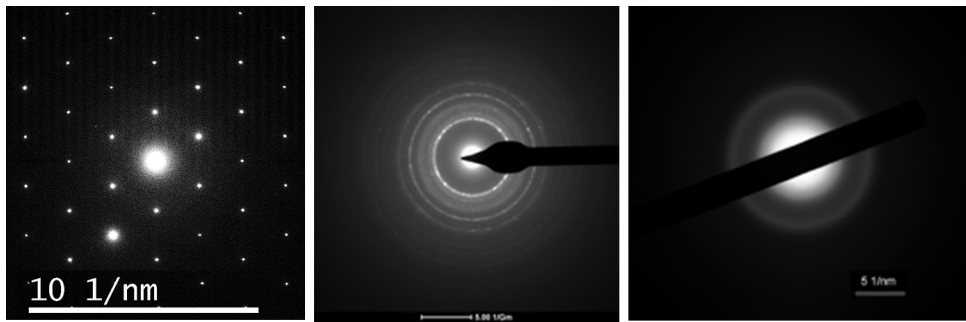


Figure 3.3: SAED pattern from single crystalline, polycrystalline and amorphous specimen (Ammrf)

obtained from electron microscopy, one is amplitude contrast image and the other is phase contrast image. The amplitude contrast includes mass-thickness contrast, Z -contrast and diffraction contrast and usually it is used for the imaging of secondary phase in matrix, defects in materials and low magnification morphology. The phase contrast is used mainly for atomic resolution imaging. When the SADP is projected on to the viewing screen or CCD, it will contain a bright central spot that contains the direct beam electrons and some scattered electrons. Two most basic imaging operations: bright-field and dark-field imaging can be performed by using these patterns in the TEM.

3.1.7 Bright Field and Dark Field Imaging

In order to view an image, an aperture called the objective aperture is inserted into the back-focal plane (BFP) of the objective lens. The bright field (BF) image is formed from the direct electron beam whereas the dark field (DF) image is formed with a specific off-axis scattered beam. The more off-axis the electrons are, the greater the aberrations and astigmatism they suffer. In order to reduce the aberrations and astigmatism as much as possible, a special DF image called centered dark-field (CDF) is employed, where the incident beam is tilted and the scattered beam emerges on the optic axis. Figure 3.4 is the schematic showing how the objective lens and objective aperture are used in combination to produce BF image, DF image and CDF image. The images can be magnified by the intermediate lenses of the microscope.

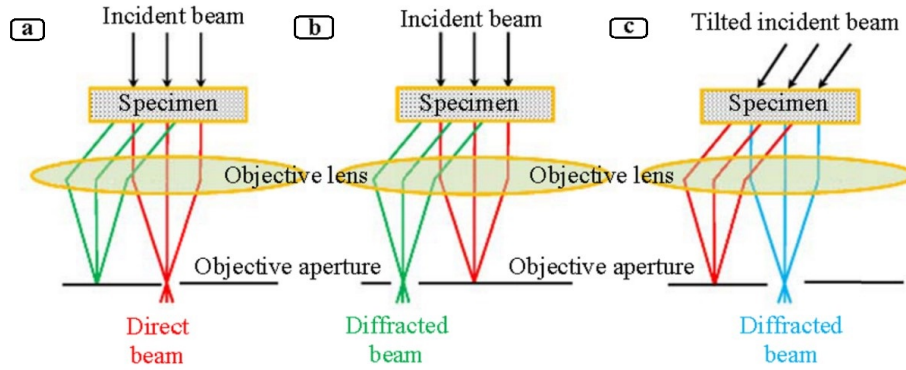


Figure 3.4: Schematic showing how the objective lens and objective aperture are used in combination to produce BF image, DF image and CDF image. (Deepak et al., 2018)

3.1.8 High Resolution Transmission Electron Microscopy (HRTEM)

HRTEM is one of the most important aspects of TEM. It is used to obtain the crystallographic detail of the specimen at atomic scale. From the atomic-scale HRTEM image, atomic arrangement in the crystal, crystal orientation and defects can be obtained. (Spence and Crewe, 1981) While the mass-thickness contrast and diffraction contrast can be seen in BF and DF images, the image contrast of HRTEM can be attributed to the phase contrast. The electron beam interacts with the electrostatic potential of the crystal and an exit wave $q(r)$ is produced from the bottom surface of the specimen. The exit wave $q(r)$ contains the information of crystal projection potential (r) and it is used as an object wave for the following objective lens. After the exit wave $q(r)$ passes through the objective lens, it experiences a Fourier transformation and a diffracted wave $Q(H)$ is formed on the back focal plane of the objective lens. Now, we enter the reciprocal space. After that, the diffracted wave $Q(H)$ experiences the Fourier transformation once again through multiplying by the contrast transfer function $T(H)$ and the object wave (r) is obtained for imaging. It is worthy to note that the contrast transfer function $T(H)$ is related to chromatic aberration, spherical aberration, focal shift and the divergence of electron beam. It is an oscillating function and vary between +1 and -1. When $T(H)$ is negative, positive phase contrast results, meaning that atoms would appear dark against a bright background. When $T(H)$ is positive, negative phase contrast results, meaning that atoms would appear bright against a dark background. When $T(H) = 0$, there is no detail in the image for this value of u . This is applicable when C_s is positive. Therefore, the

biggest challenge for HRTEM is the interpretation of image. In order to identify the atoms in most of the HRTEM image, image simulation based on atomic model, thickness, focus, stigmatism and coma is carried out. From the matched results between the experimental and simulated images, the atom species in HRTEM image can be confirmed [Williams and Carter \(2009\)](#).

3.1.9 Scanning Transmission Electron Microscopy (STEM)

In STEM imaging, a fine probe of electron (converged beam) is scanned over the specimen in contrast to the use of parallel beam in TEM. Figure 3.5 shows a simplified schematic of the STEM optical configuration. The condenser lenses focuses a beam to form a fine probe, and then the scan coils are used to scan the probe over a thin electron-transparent specimen in a raster and the scattered signals can be detected using various detectors and plotted as a function of probe position to form magnified images in STEM. The STEM image quality depends on the probe; the important parameters are the probe current, probe size and the convergence semiangle.

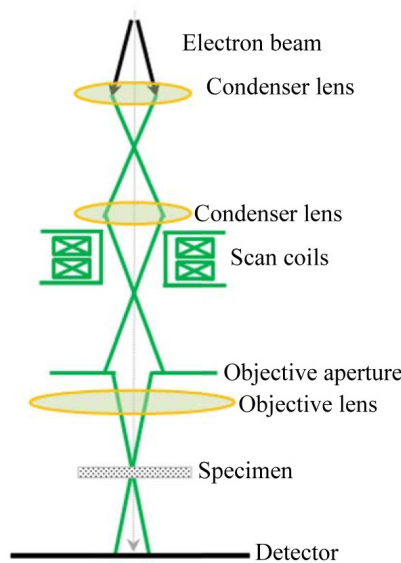


Figure 3.5: A schematic diagram of the optical path for STEM. [Deepak et al. \(2018\)](#)

The most significant advantage for STEM is that, the influence of chromatic aberration observed in TEM is absent in STEM images. This advantage makes STEM ideal to deal with thicker samples in comparison to TEM. The reason is the fact that STEM doesn't use lenses to form the image. The resolution in STEM is limited by the beam dimensions, which is affected by the aberrations. By using a probe corrected electron microscope, resolution that can be attained is up to ~ 0.08 nm at 200 kV and ~ 0.06 nm at 300 kV.

Another potential advantage is that there is a wide range of possible signals available in the STEM, especially the annular bright field (ABF) [Ishikawa et al. \(2011\)](#)([Huang et al., 2011](#)) and high annular angle dark field (HAADF) [Pennycook and Jesson \(1991\)](#) techniques. Figure 3.6 show the schematic diagram of HAADF-STEM and ABF-STEM techniques.

The HAADF-STEM imaging technique utilizes the electrons scattered to relatively high angles (>50 mrad). It can help in distinguishing the composition of an atomic column as the contrast in HAADF-STEM images are directly proportional to $\sim Z^{1.4}$ (Z : atomic number) [Pennycook and Jesson \(1991\)](#). On the other hand, the ABF-STEM imaging technique utilizes the scattered electrons collected from the sample at relatively low collection angles and it is very sensitive to light elements, even to the lightest element, hydrogen. The combination of the atomic-number sensitivity, light-element sensitivity and high resolution, makes advanced STEM an extremely useful tool to the comprehensive study of many different kinds of materials.

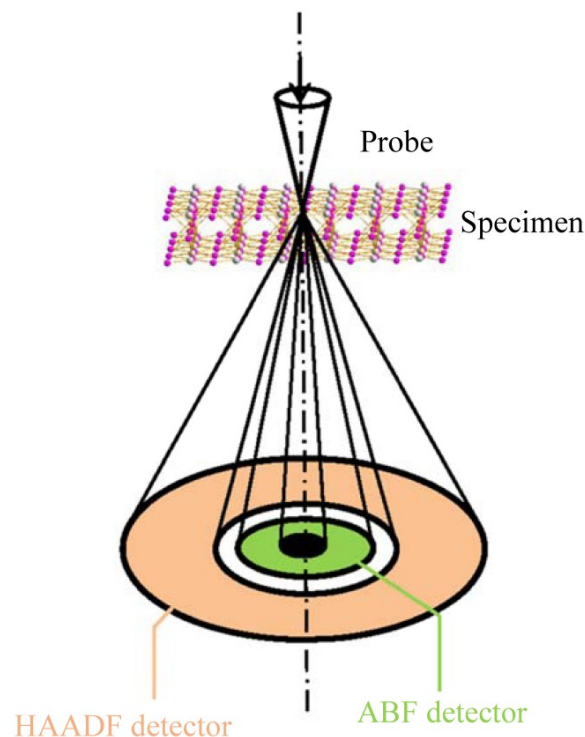


Figure 3.6: A schematic diagram of HAADF-STEM and ABF-STEM techniques [Deepak et al. \(2018\)](#)

3.1.10 Aberration Corrected TEM/STEM

One major goal of electron microscopy is to be able to acquire images that are directly interpretable and provide new important information about the materials under study. However, because of unavoidable imperfections in the manufacture of electromagnetic lenses, most conventional TEMs suffer from a variety of aberrations that diminish the obtainable resolution. A few of the major ones are spherical aberration, chromatic aberration, and astigmatism. The most severe is spherical aberration (C_s), which causes image delocalization, or an inability to define the specific location of a feature, where the image of a point is represented as a blurred disk. This is due to the inhomogeneous forces that the lens (objective for conventional TEM and condenser for STEM) transfers to off-axis electron beams, and the extent of blurring depends on both the magnitude of the spherical aberration coefficient (C_s) and the objective lens strength. The smearing/delocalization limits the resolution of the TEM and the ability to interpret an image properly. To minimize the effects of delocalization, it is critical to image as close to the Scherzer defocus as possible. The Scherzer defocus is the optimal objective lens condition for a given microscope and limits the effect of delocalization:

Spherical aberration correction was first theorised by Scherzer in 1947 and made possible in the TEM in 1997 [Haider et al. \(2009\)](#). A C_s corrector can compensate for the distortion in the lens by using multi-pole lenses in series with the objective lens. There are two types of C_s correctors: the quadrupole-octupole corrector and the hexapole corrector. By producing a negative C_s , the corrector compensates for the positive C_s in the objective lens, resulting in zero C_s . In the case of chromatic aberrations, the defocus spread due to chromatic aberration is given by $C_c = dE/E_o$, where C_c is the chromatic-aberration coefficient of the lens, dE is the energy loss of the electrons and E_o is the initial beam energy. In order to overcome C_c and achieve an information limit better than $(0.1 \text{ nm})^{-1}$, TEMs are additionally equipped with a monochromator. The ability to correct C_c has also been made possible within the last decade with the design of C_c correctors [Krivanek et al. \(2009\)](#). At present, aberration-corrected electron microscopes obtain sub-Angstrom resolution. Figure 3.7 shows an FEI Titan ChemiSTEM transmission electron microscope, which is a state of the art electron microscope capable of doing this.

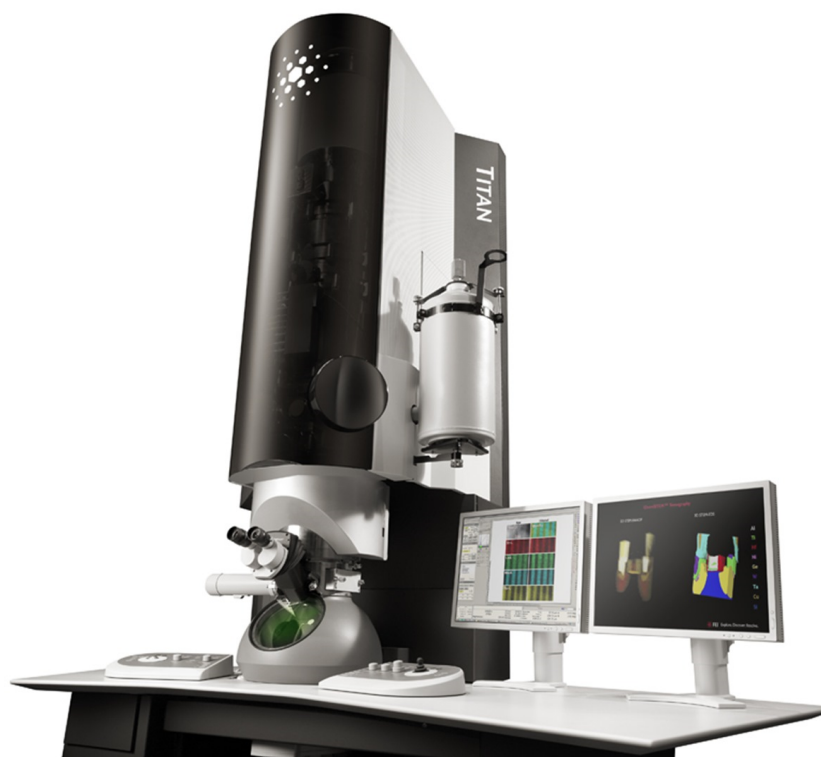


Figure 3.7: Titan ChemiSTEM

3.1.11 Spectroscopic Techniques in TEM

In TEM, the most common spectroscopic techniques include energy dispersive X-ray spectroscopy and electron energy loss spectroscopy. These transform electron microscopy to analytical electron microscopy.

Energy-Dispersive X-ray Spectroscopy (XEDS/EDX/EDS)

Characteristic X-rays are generated from the elements present in the specimen when the electron beam strikes the specimen. These X-rays can be detected by a semiconductor detector and identified as to which elements they belong to. The X-ray counts as a function of the energy (in keV) form an EDX spectrum as shown in figure 3.8. EDX can be used to find the chemical composition of materials, quantify the specific elements and show element composition distribution over a region of interest. However in some cases the peaks due to different elements overlap resulting in difficulty in identification/quantification and also the lightest elements cannot be detected, which sometimes limits the application of EDX. However, EDX can provide fundamental compositional information for a wide variety of materials and it is routinely used along with TEM/STEM imaging.

EDX in STEM mode can be used for mapping the composition of a region of interest.

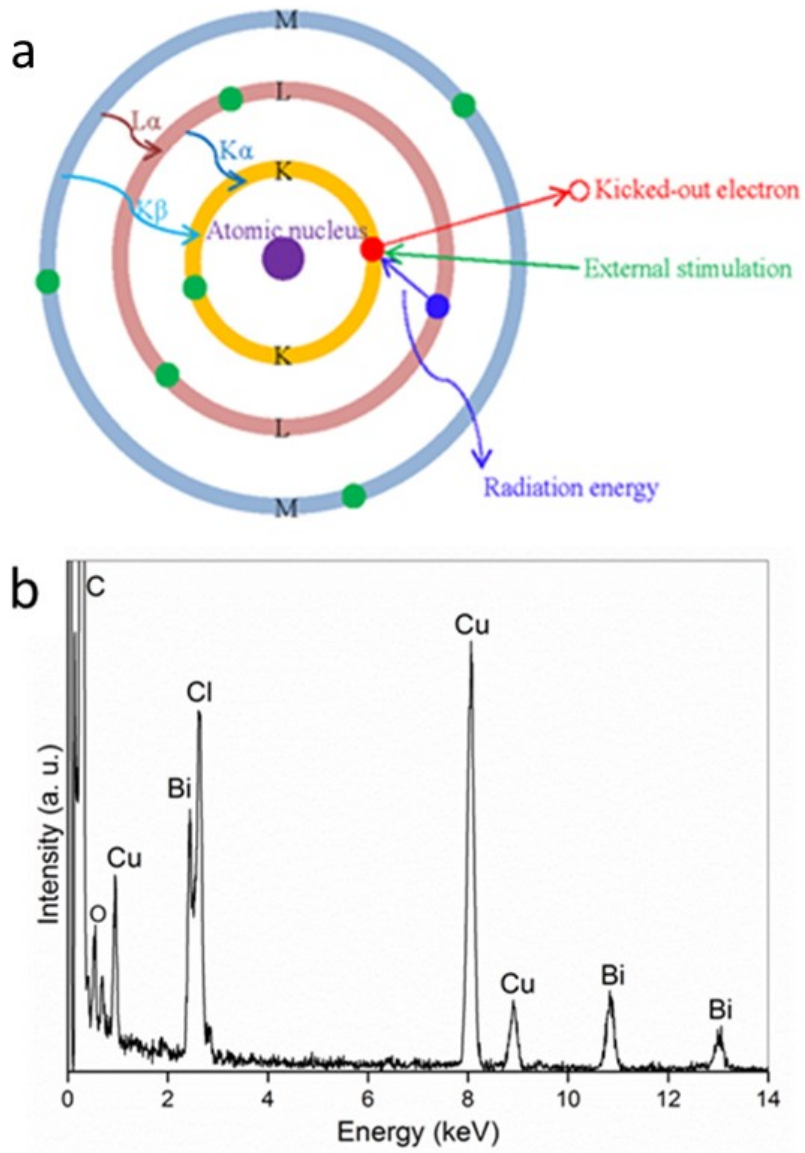


Figure 3.8: a). Schematic representation of X-ray generation by e beam irradiation. Deepak et al. (2018) b) A typical EDX spectrum

In this technique of spectrum imaging, a complete spectrum is collected at every pixel and the various X-ray peaks could be used for obtaining chemical maps during post processing.

Electron Energy Loss Spectroscopy (EELS)

When the electrons pass through the specimen, the transmitted electrons will lose a measurable amount of energy. These electrons as a function of the energy lost form a spectrum. This spectrum is referred to as EELS spectrum. Compared with EDX, EELS is particularly sensitive to lighter elements and it is useful for thinner TEM samples. EELS is a more difficult technique, but is a useful tool to measure the thickness of specimen, chemical bonding, electronic structure and atomic composition. EELS involves the energy analysis of inelastically scattered electrons from a nearly monochromatic electron beam due to interaction with electron-transparent specimen. Typically a magnetic prism disperses these electrons according to energy, subsequent to which a spectrometer located at the correct position can collect electrons of a specific energy as shown in figure 3.9 [Egerton \(2011\)](#) [Williams and Carter \(2009\)](#). Electron energy loss occurs due to excitations of various internal energy modes-typically electronic (with ΔE in the UV-vis region) and vibrational (IR region)-in the nanoparticle or in molecular adsorbates on the specimen surface. For example, EELS can be used to measure surface plasmon spectra for nanoparticles and vibrational spectra of molecules adsorbed on nanoparticles. The high spatial resolution of EELS can be used to map out surface plasmons across a nanoparticle. High resolution EELS (HREELS) is a variant of EELS with energy resolution in the 100 *meV* range. As in the case of EDX, spectrum imaging can be achieved using various features in EELS spectrum when EELS is carried out in the STEM mode.

3.2 X-ray photoelectron spectroscopy (XPS)

X-ray photoelectron spectroscopy (XPS) is a surface characterization technique useful to obtain elemental composition, chemical state and electronic state of the constituent elements in a material. Kai Siegbahn, won the Nobel Prize in physics in 1981 for developing XPS in the 1960s, which used to be known as Electron Spectroscopy for Chemical Analysis (ESCA). XPS works based on the principle of photoelectric effect. XPS spectra are obtained by irradiating a material with a beam of X-rays of known energy and measuring the kinetic energy and number of electrons that escape from the top few nm of the material being analysed. The core electron present in the atom are held

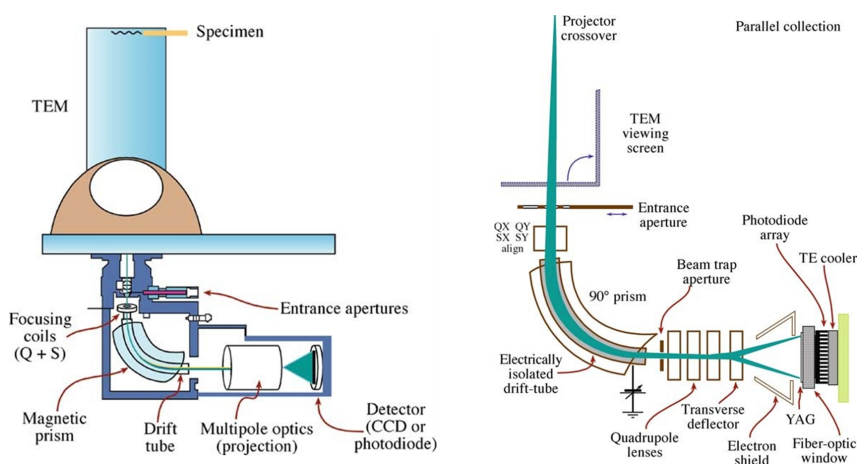


Figure 3.9: Schematic showing how an EELS spectrometer is coupled with a TEM with its components along with the ray diagram showing how a magnetic prism spectrometer disperses and focusses the no-loss and energy-loss electrons in the image plane of the spectrometer [Williams and Carter \(2009\)](#)

by the characteristic binding energy. When an X-ray beam of sufficient energy hits on the sample surface, the core electron will escape from the atom and emit out of the surface as shown in Figure 3.10. The excess energy counts for the kinetic energy of the electrons emitted. As the energy of an X-ray used is known, and the XPS measures the kinetic energy of emitted electrons, the electron binding energy of each of the emitted electrons can be determined by using an equation that is based on the work of Einstein:

$$E_{binding} = E_{photon} - (E_{kinetic} + \phi) \quad (3.14)$$

where $E_{binding}$ is the binding energy (BE) of the electron, E_{photon} is the energy of the X-ray photons being used, $E_{kinetic}$ is the kinetic energy of the electron as measured by the instrument and ϕ is the work function dependent on both the spectrometer and the material. A typical XPS spectrum is a plot of the number of electrons detected versus the binding energy of those electrons. Each element produces a characteristic set of XPS peaks at binding energy values that directly identify each element that exists on the surface of the material being analysed. The number of detected electrons in each of the characteristic peaks is directly related to the amount of element within the XPS sampling volume. To generate atomic percentage values, each of the XPS signal must be corrected by dividing its signal intensity by a relative sensitivity factor and normalized over all of the elements detected. XPS detects only those electrons that have actually escaped from the sample into the vacuum of the instrument, and reach the detector. In order to escape from the sample into vacuum, a photoelectron must travel through the

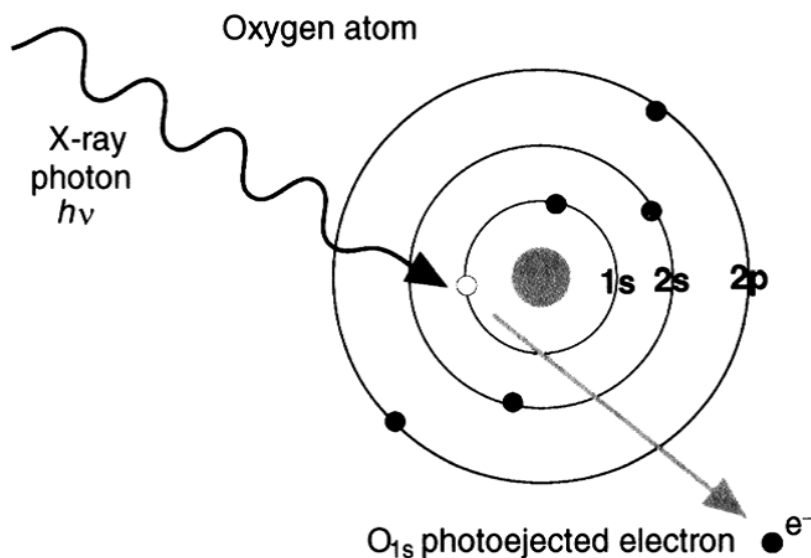


Figure 3.10: A schematic of electron generation by X ray

sample. This causes the surface sensitivity of XPS. The ability to extract chemical state information from the topmost few nm of any surface makes XPS a unique and valuable tool for understanding the chemistry of any surface. In this context, chemical state refers to the local bonding environment of a species under study. The local bonding environment of a species is affected by its formal oxidation state, its nearest-neighbour atom and its bonding hybridization to the nearest-neighbour. For example, while the nominal binding energy of the C1s electron is 284.6 eV, subtle shifts in the actual binding energy, the so-called chemical shift, provide the chemical state information. A simple representation of the operation of XPS is shown in Figure 3.11. An XPS spectrometer is shown in Figure 3.12

3.3 Raman spectroscopy

Raman spectroscopy is a vibrational spectroscopic techniques used to provide information on molecular vibrations and crystal structures. In this technique, the sample is irradiated with a laser light source, and the Raman scattered light is recorded on a CCD camera. A schematic of the Raman instrumentation is shown in Figure 3.13.

The characteristic pattern in a Raman spectrum is used as fingerprints to obtain various details of the sample, including polymorphs, local crystallinity, orientation and stress.

When light is scattered by matter, almost all of the scattering is an elastic process (no

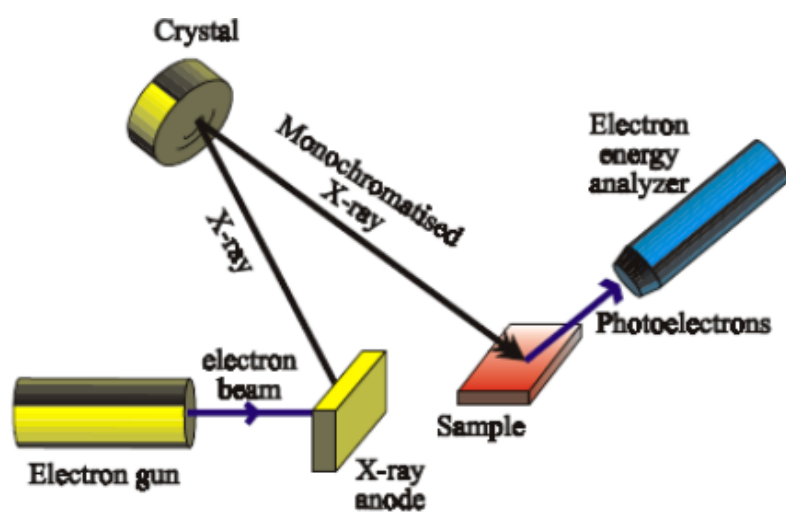


Figure 3.11: A schematic of XPS instrumentation

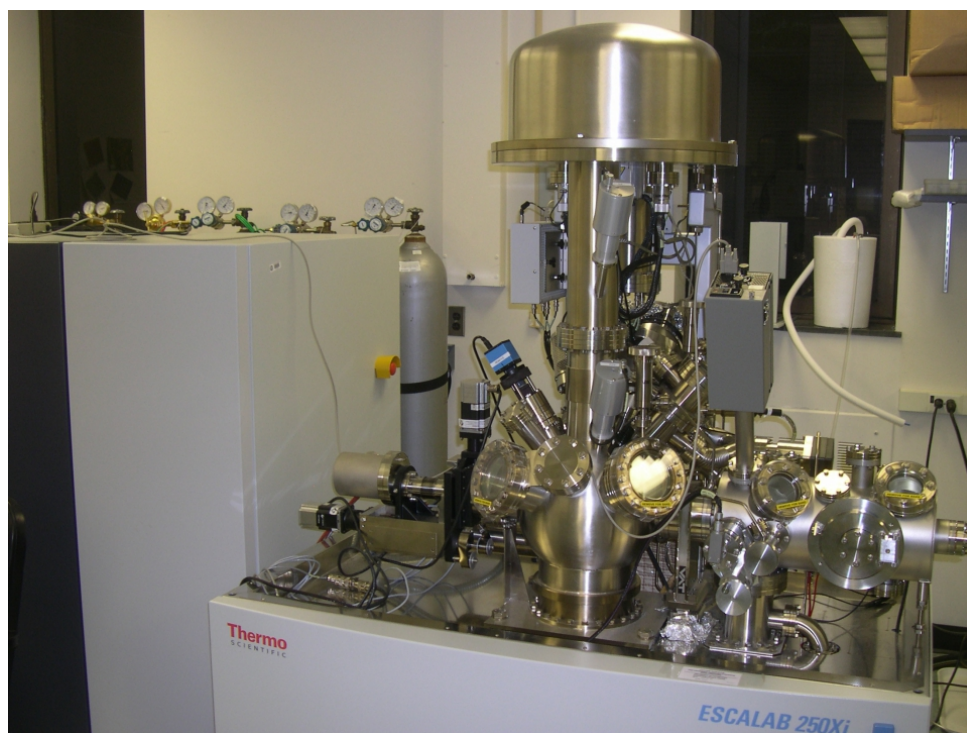


Figure 3.12: An XPS spectrometer - KRATOS

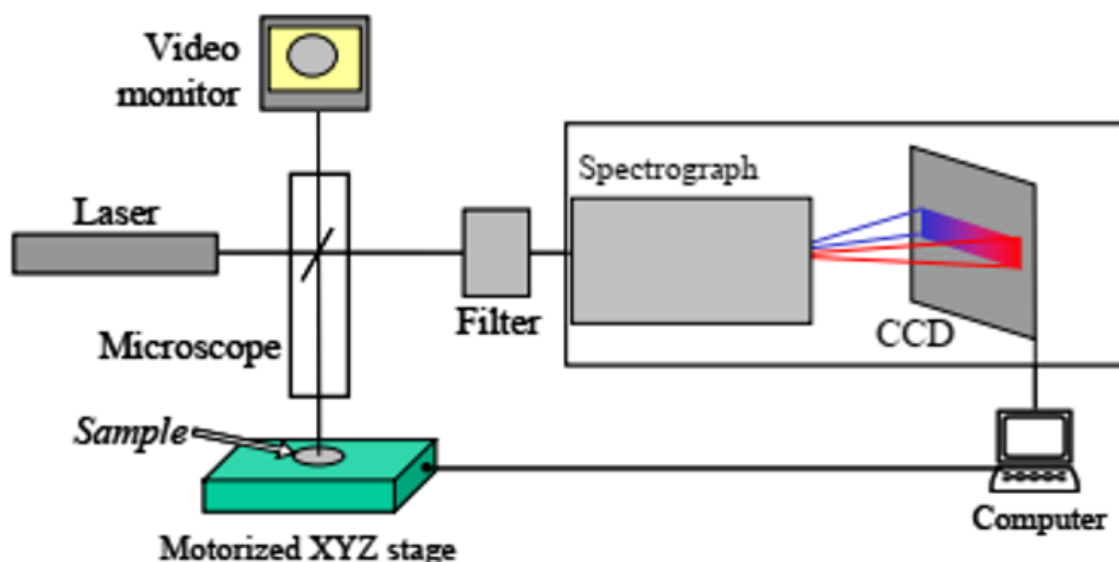


Figure 3.13: A schematic of Raman spectroscopy instrumentation [Gouadec and Colombari \(2007\)](#).

energy loss) and it is called as Rayleigh scattering. However, a very small percentage of inelastic scattering can occur resulting in a scattered light with different energy than that of the incident light. This inelastic scattering of light was first observed experimentally by C V Raman in 1928, and it is named after him as Raman scattering (Raman effect). The Raman spectrum is expressed in a form of intensity of scattered light versus wavenumber (the reciprocal of wavelength).

In Raman spectroscopy, wavenumber is commonly used because it is linearly related with energy and makes the Raman spectrum independent of excitation wavelength. For example, the Raman peak of crystalline silicon appears at a wavenumber of 520 cm^{-1} independent of the excitation wavelength used. However, if you use wavelength as the horizontal axis, the measured Raman shift of silicon appears at 547.14 nm when 532 nm excitation is used and 818.41 nm when 785 nm excitation is used [Nanophoton](#). To understand the Raman effect, consider what happens to a molecule when it is placed in a static electric field. The molecule will be distorted, the positive nuclei being attracted towards the negative pole of the field while the electrons will be attracted towards the positive pole of the field. This separation of charge causes an induced electric dipole moment to be set up in the molecule. The molecule is said to be polarised. The size of this induced dipole, μ , depends on both the magnitude of the applied field, E , and on the

ease with which the molecule can be distorted. It therefore is the case that

$$\mu = \alpha E \quad (3.15)$$

where α is the polarizability of the molecule. When a molecule is subjected to a beam of electromagnetic radiation of frequency ν , the electric field experienced by each molecule varies according to the equation

$$E = E_0 \sin 2\pi \nu t \quad (3.16)$$

The induced dipole also undergoes oscillations of frequency :

$$\mu = \alpha E = \alpha E_0 \sin 2\pi \nu t \quad (3.17)$$

Such an oscillating dipole emits radiation of its own oscillation frequency, the classical explanation of Rayleigh scattering. If, in addition, however, the molecule undergoes some internal motion, such as vibration or rotation which changes the polarizability periodically, then the oscillating dipole will have superimposed on it the vibrational or rotational oscillation. For example consider a vibration of frequency ν_ν which changes the polarizability.

$$\alpha = \alpha_0 + \beta \sin 2\pi \nu_\nu t \quad (3.18)$$

where α_0 is the equilibrium polarizability and β represents the rate of change of polarizability with the vibration. Therefore

$$\mu = \alpha E = (\alpha_0 + \beta \sin 2\pi \nu_\nu t) E_0 \sin 2\pi \nu t \quad (3.19)$$

The above equation can be written as

$$\mu = \alpha_0 E_0 \sin 2\pi \nu t + \frac{1}{2} \beta E_0 \{ \cos 2\pi(\nu - \nu_{nu})t - \cos 2\pi(\nu + \nu_{nu})t \} \quad (3.20)$$

From this equation it can be seen that the dipole not only oscillates at the exciting frequency ν , but also has frequency components $\nu \pm \nu_\nu$. These frequency components are the origin of the Stokes and anti-Stokes shifted Raman scattering. Radiation scattered with a frequency lower than that of the incident beam is referred to as Stokes radiation while that at a higher frequency is referred to as anti-Stokes radiation. It should be noted that if the vibration (or rotation) does not alter the polarizability, then $\beta = 0$ and the dipole oscillates only at the frequency of the incident radiation. So in order to be Raman

active a molecular rotation or vibration must cause some change in the component of the molecular polarizability.

This means that intense Raman scattering occurs from vibrations which induce a large distortion of the electron cloud around the molecule. A peak appearing in the Raman spectrum is due to a specific molecular vibration or lattice vibration. Peak position shows the specific vibrational mode of each molecular functional group of the material. The same vibrational modes for each functional group will show a shift in peak position due to the environment of the functional group, thus it is said the Raman spectrum shows the molecular fingerprint of the target.

In addition to the position, the shape of the Raman peak is also important as it can give information on the crystallinity of the sample. Whether there is much or little crystallinity can be read from the width of the peak. Any residual stress present in the crystal can be evaluated from the direction and amount of shift of the Raman peak. A photo of Raman spectrometer is shown in Figure

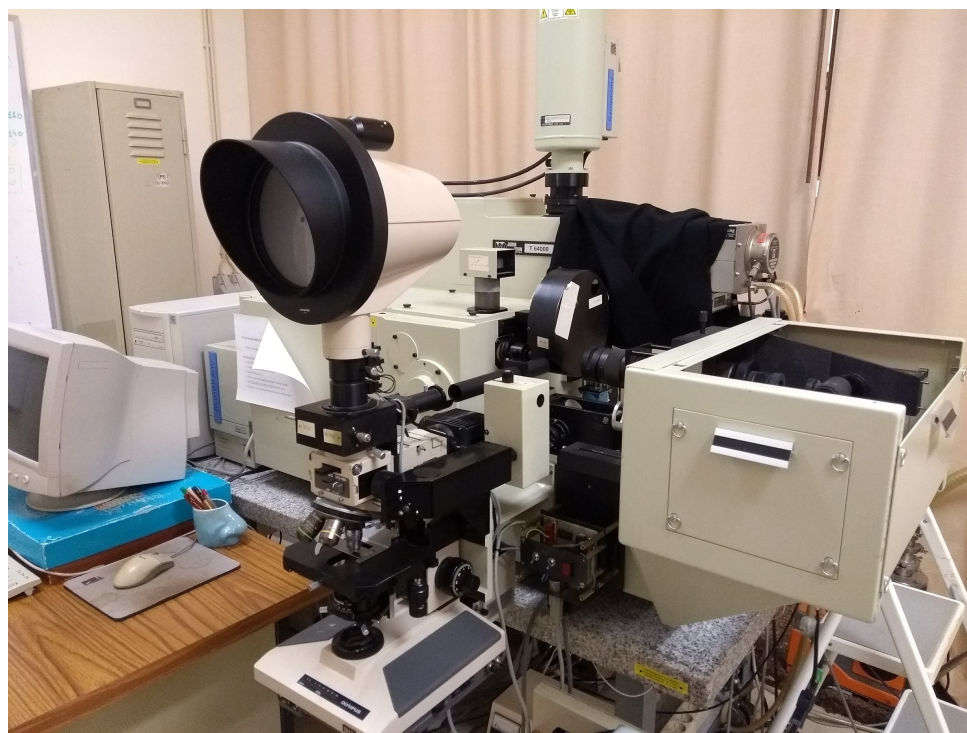


Figure 3.14: Raman spectrometer - Jobin-Yvon T64000

Chapter 4

Results and Discussions

4.1 Electron Microscopy of TNW and TNT

4.1.1 TNW

Figure 4.1 shows the STEM images of the reference sodium titanate nanowire sample without any modification confirming the wire-like morphology of the TNW sample. Figure 4.2 shows the high magnification STEM images of the sample with average interplanar distance of 0.73 nm. The (001) d spacing of monoclinic $\text{Na}_2\text{Ti}_3\text{O}_7$ (PDF number: 00-031-1329) is expected to be 0.84 nm. The decrease in interplanar spacing could be due the presence of some amount of H^+ instead of Na^+ , as in the case of $\text{Na}_x\text{H}_{2-x}\text{Ti}_3\text{O}_7$ previously reported Bem et al. (2012). The amount of H^+ depends on the pH of the synthesis. EDX maps showing the distribution of Ti, O and Na are shown in Figure 4.3. The corresponding spectrum and quantification obtained from it are shown in Figure 4.4.

4.1.2 TNT

The morphology and composition of the TNT sample was observed under STEM. Figure 4.5 shows the low magnification images confirming the tube morphology. The high magnification images of the sample is shown in Figure 4.6 revealing the multilayered tube walls with a interlayer spacing of 0.76 nm. The d spacing is smaller compared to (001) of $\text{Na}_2\text{Ti}_3\text{O}_7$ (PDF number: 00-031-1329). Figure 4.7 shows the EDX mapping on a single TNT showing the distribution of Ti, O and Na. The EDX spectrum and quantification are shown in Figure 4.8.

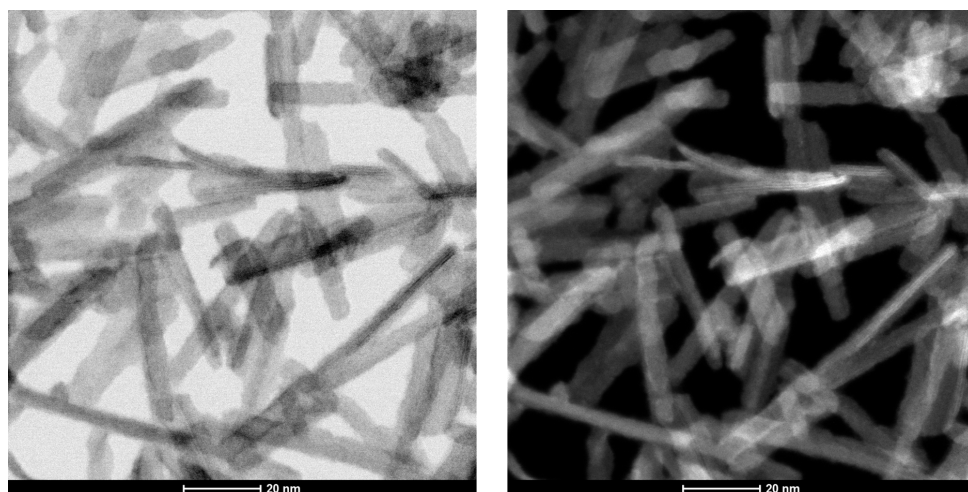


Figure 4.1: STEM BF image (left) and HAADF image (right) showing the morphology of TNW

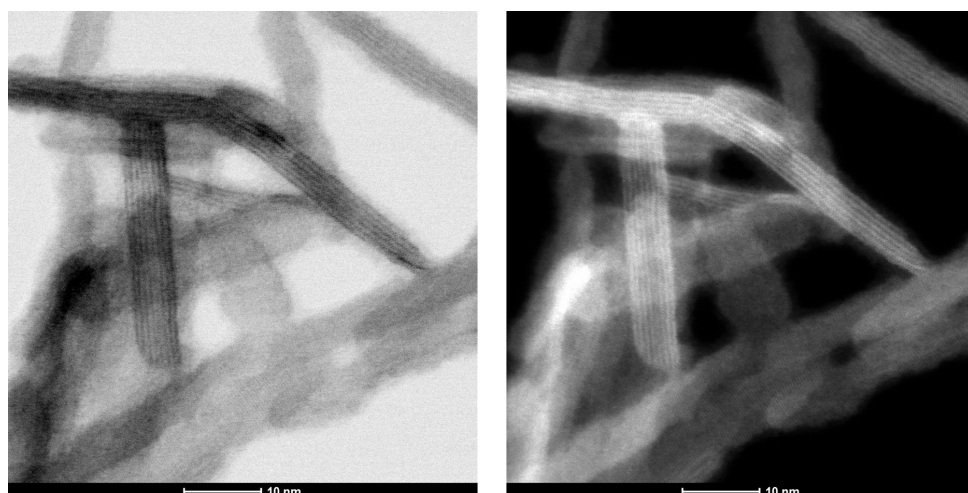


Figure 4.2: STEM BF image (left) and HAADF image (right) of TNW showing the layers

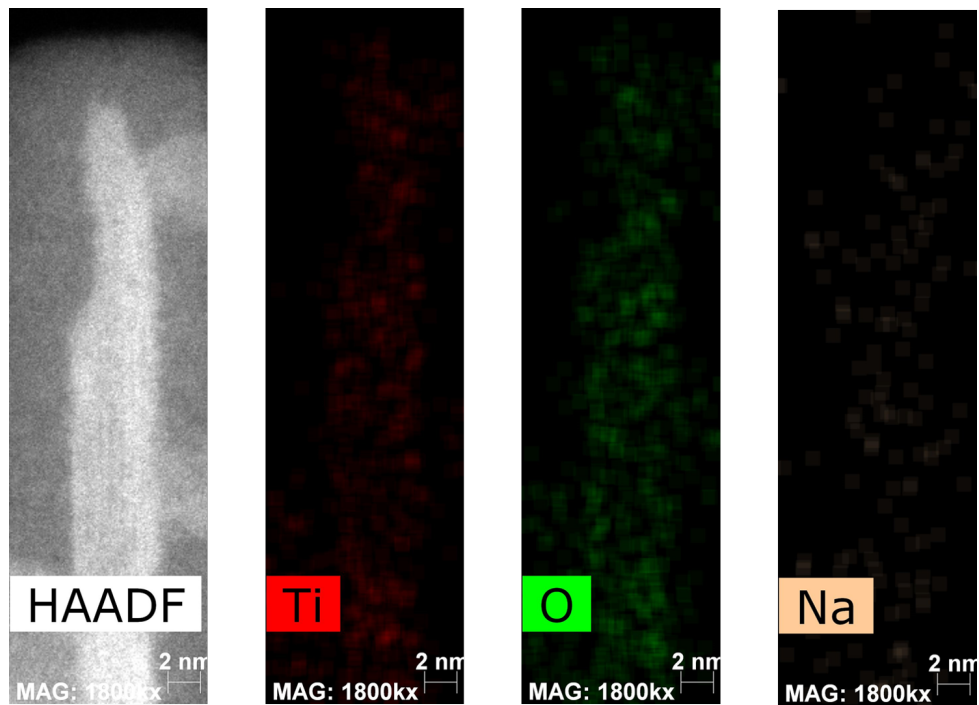


Figure 4.3: EDX mapping of TNW

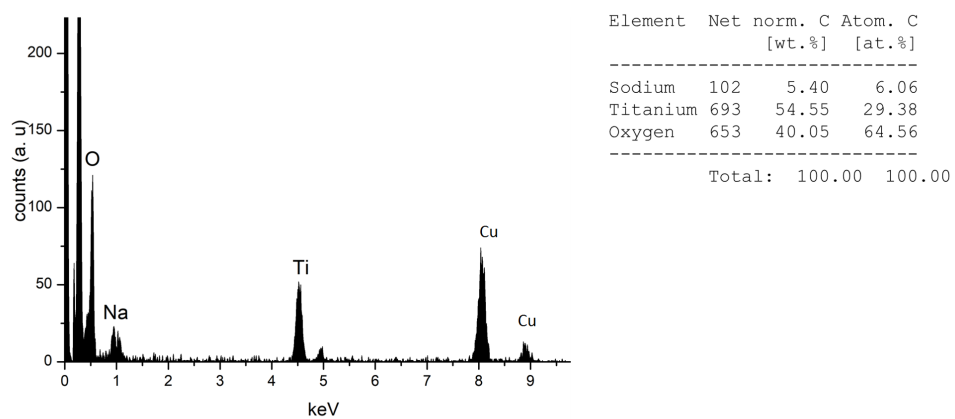


Figure 4.4: EDX spectrum and quantification results of TNW

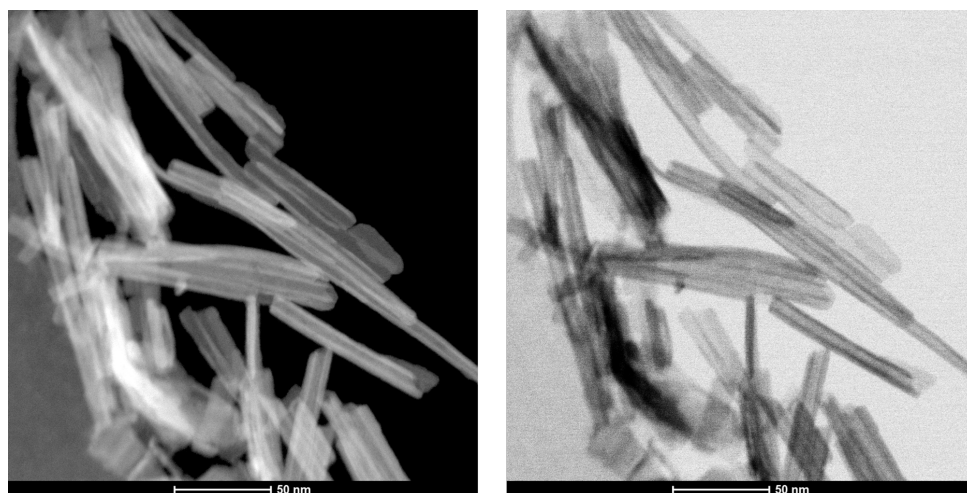


Figure 4.5: STEM HAADF image (left) and BF image (right) showing morphology of TNT

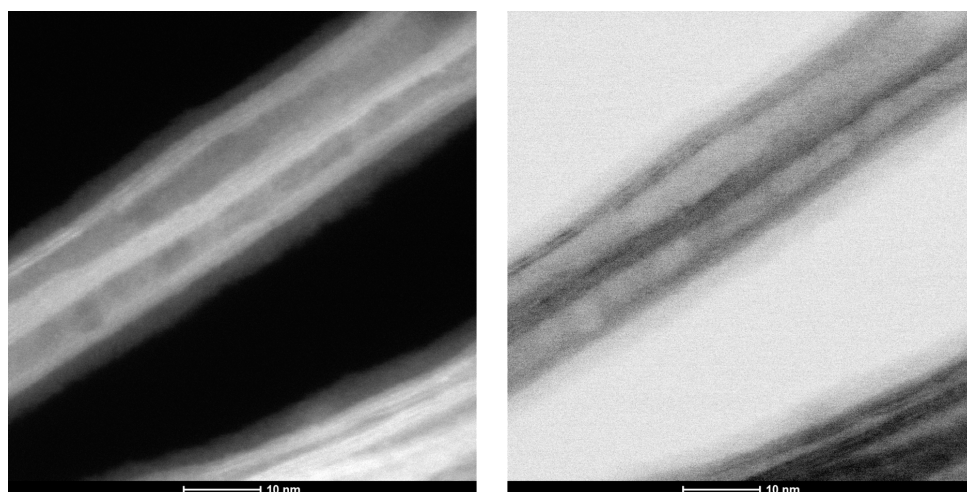


Figure 4.6: STEM HAADF image (left) and BF image (right) showing interlayers of TNT

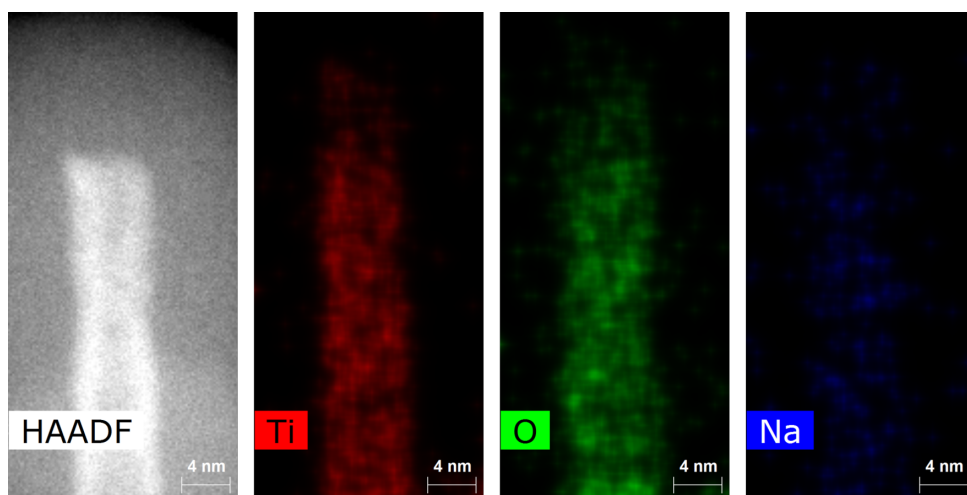


Figure 4.7: EDX mapping of TNT

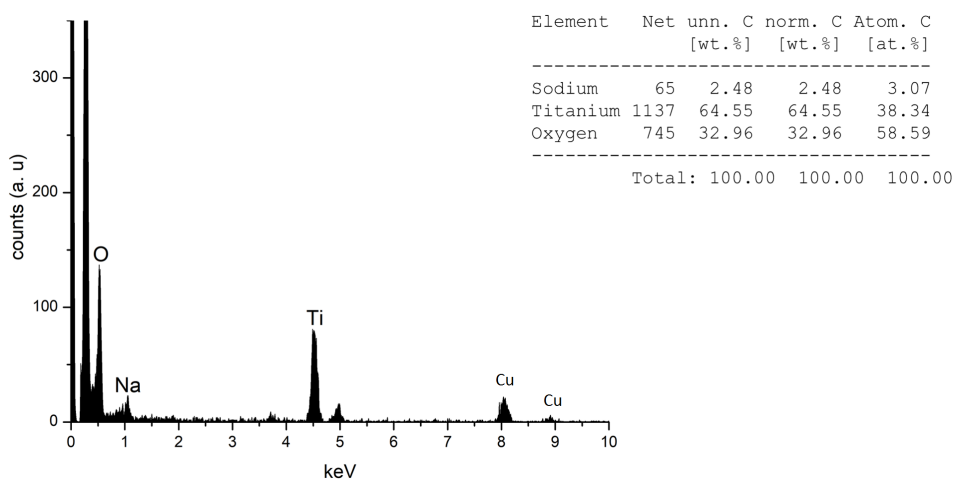


Figure 4.8: EDX spectrum and quantification results of TNT

4.2 Electron microscopy of Co doped titanate nanowires

Modification of titanate nanowires was carried out by doping different quantities of Co. Results of the electron microscopy study on the various doped samples are discussed below.

4.2.1 Co(1%)-TNW

Electron microscopy investigations using STEM imaging and EDX analysis is shown below. Figure 4.9 and Figure 4.10 show the low magnification and high magnification images of the Co(5%) TNW sample. From the images, it can be seen that the morphology is of a nanowire. From the EDX map in Figure 4.11 it can be seen that Co intensity is low. This is due to the small amount of Co present and can be observed as a small peak in the spectrum shown in Figure 4.12. The quantification gives Co as 0.43 at%. The interlayer spacings obtained from HRTEM and STEM are between 0.71 nm and 0.76 nm as shown in 4.13, similar to that of TNW. The diameter of the wires are 3-10 nm.

4.2.2 Co(5%)-TNW

Figure 4.14 and Figure 4.15 shows the low magnification and high magnification images of the Co(5%) TNW sample. From the images, it can be seen that the morphology is of a nanotube rather than of the expected nanowire morphology. From the EDX maps 4.16 and spectrum 4.17 it can be seen that Co is present in the sample. The quantification

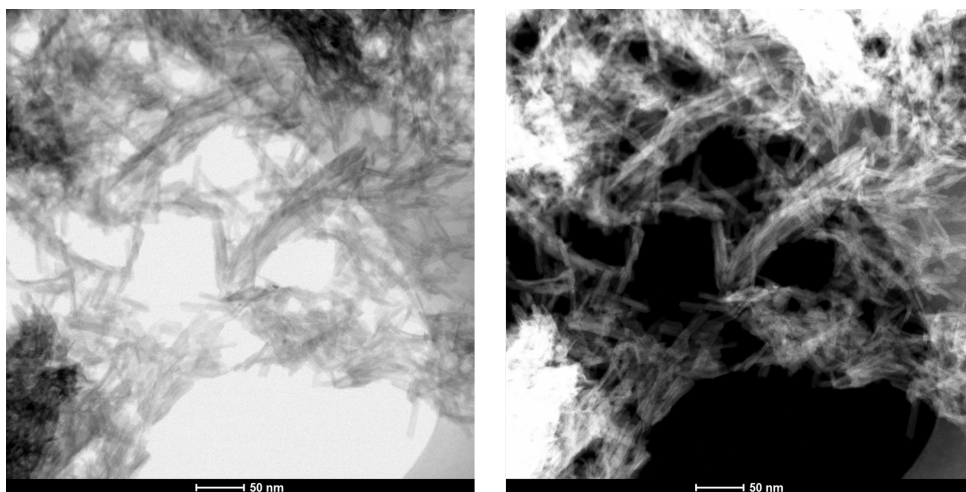


Figure 4.9: STEM BF image (left) and HAADF image (right) of Co(1%) TNW.

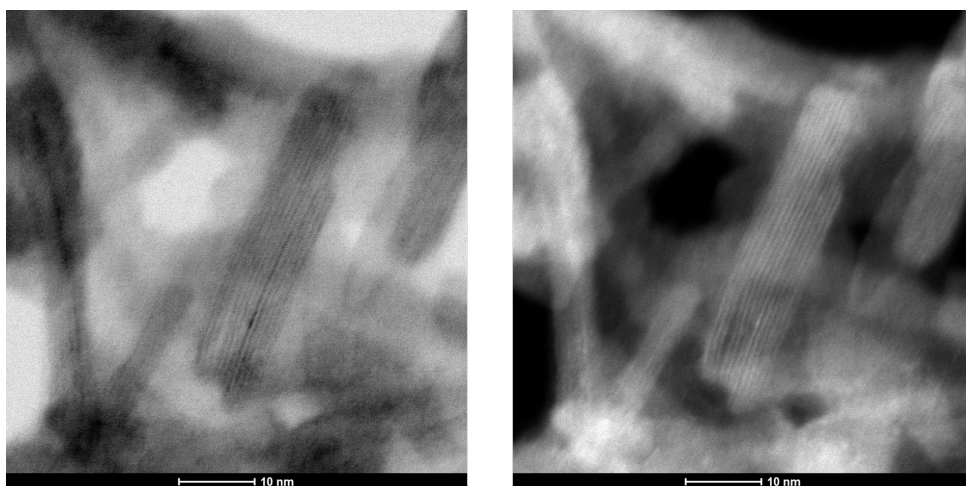


Figure 4.10: STEM BF image (left) and HAADF image (right) showing the layered structure of Co(1%) TNW.

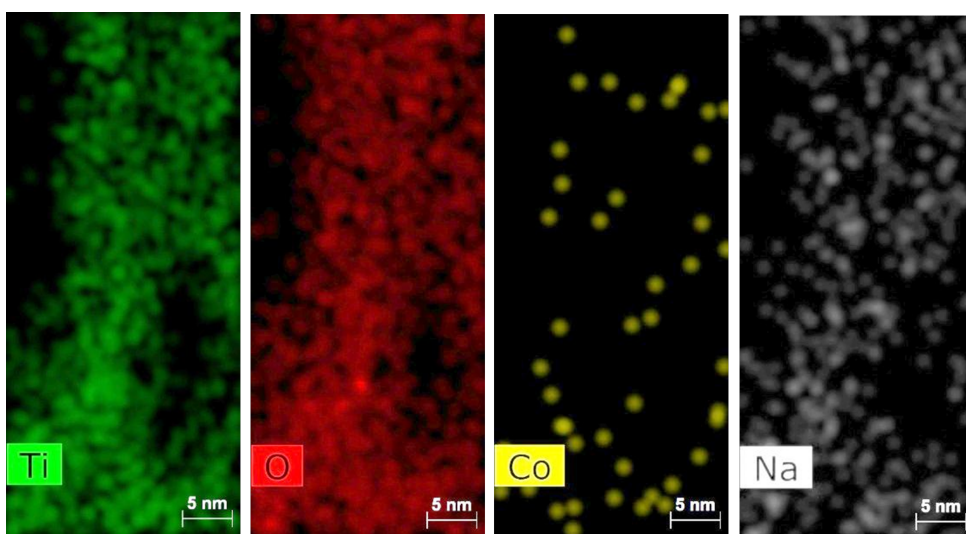


Figure 4.11: EDX mapping of Co(1%) TNW.

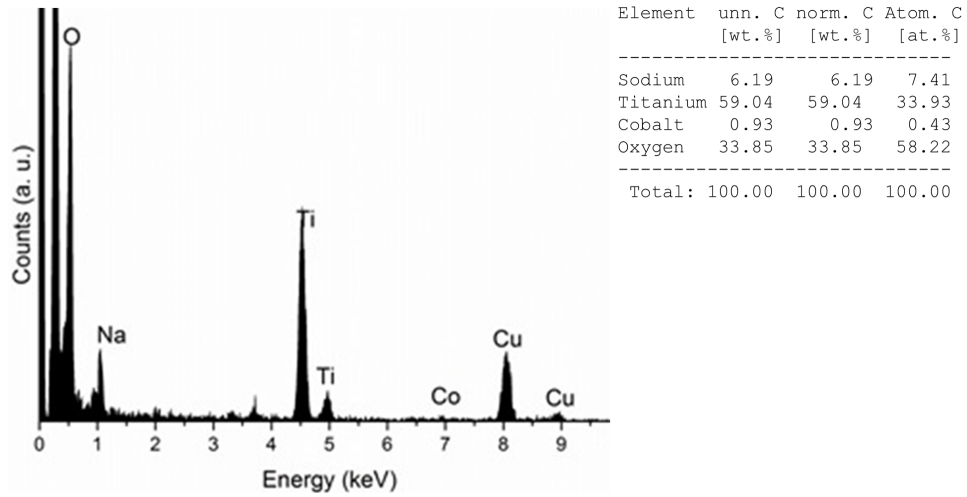


Figure 4.12: EDX spectrum and quantification of Co(1%) TNW.

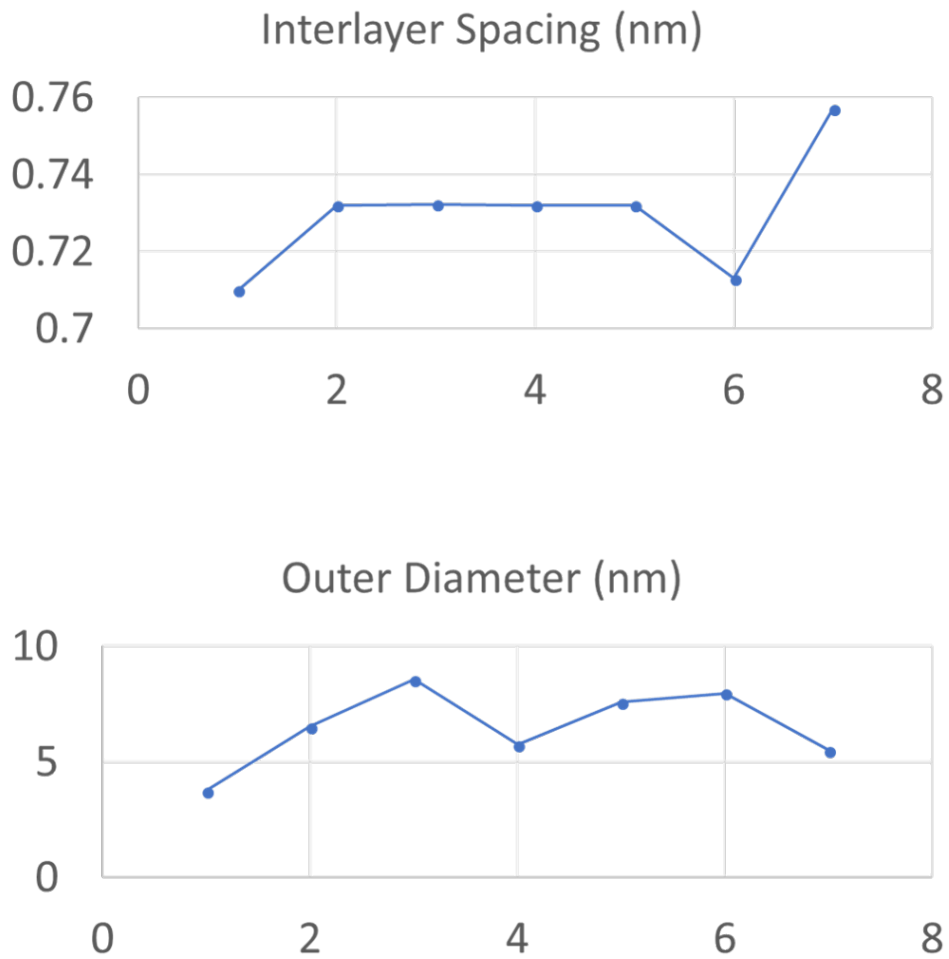


Figure 4.13: Interlayer spacing and diameter distribution of Co(1%) TNW.

gives Co as 1.48 at%.

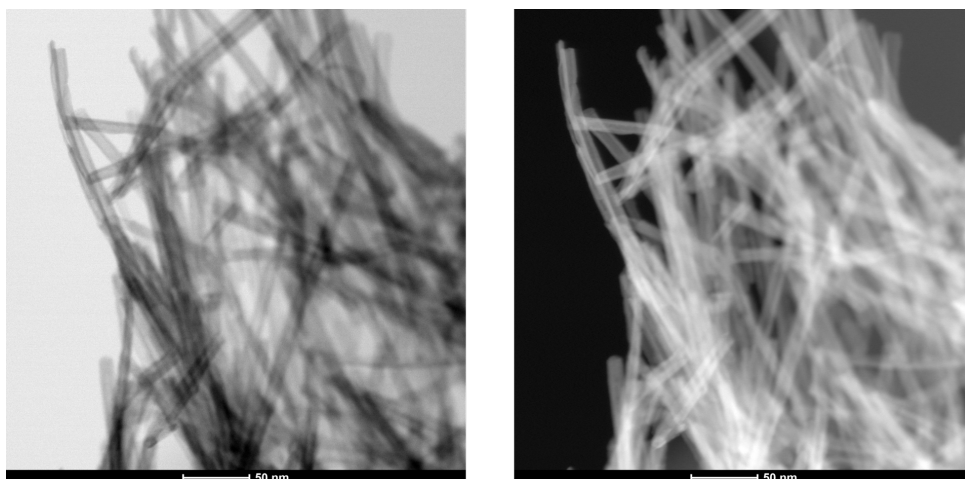


Figure 4.14: Low magnification images of the Co(5%) TNW sample.

In the two samples of Co doped TNW analyzed, Co(1%) TNW and Co(5%) TNW, Co was detected in EDX though the quantities were less than that of the expected values. The nanowire morphology was observed as expected in the case of Co(1%) TNW whereas nanotube morphology was observed for Co(5%) TNW .

4.3 Co Intercalated titanate nanowires

The TNW samples modified by intercalation with cobalt are discussed below.

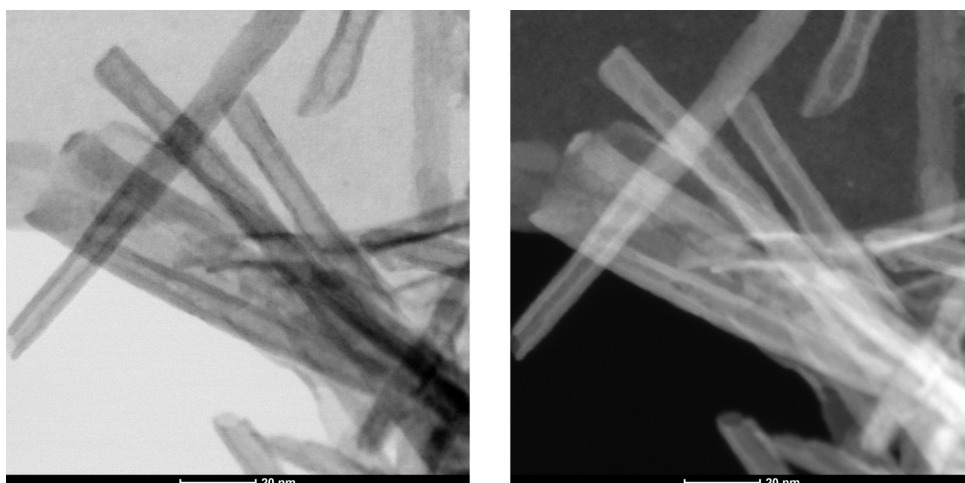


Figure 4.15: High magnification images of the Co(5%) TNW sample.

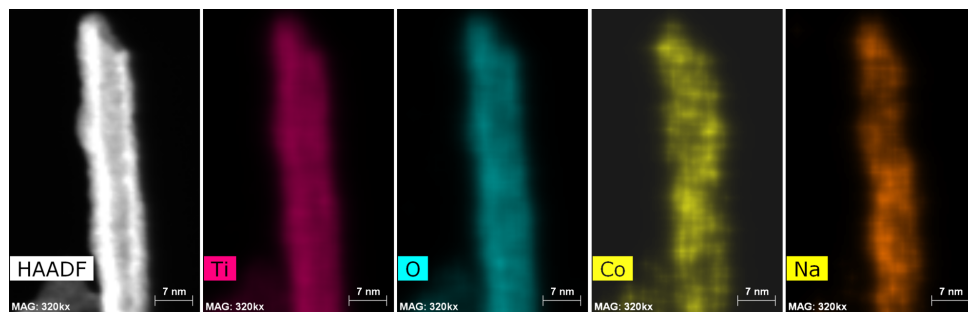


Figure 4.16: EDX maps on a single nanotube of the Co(5%) TNW sample.

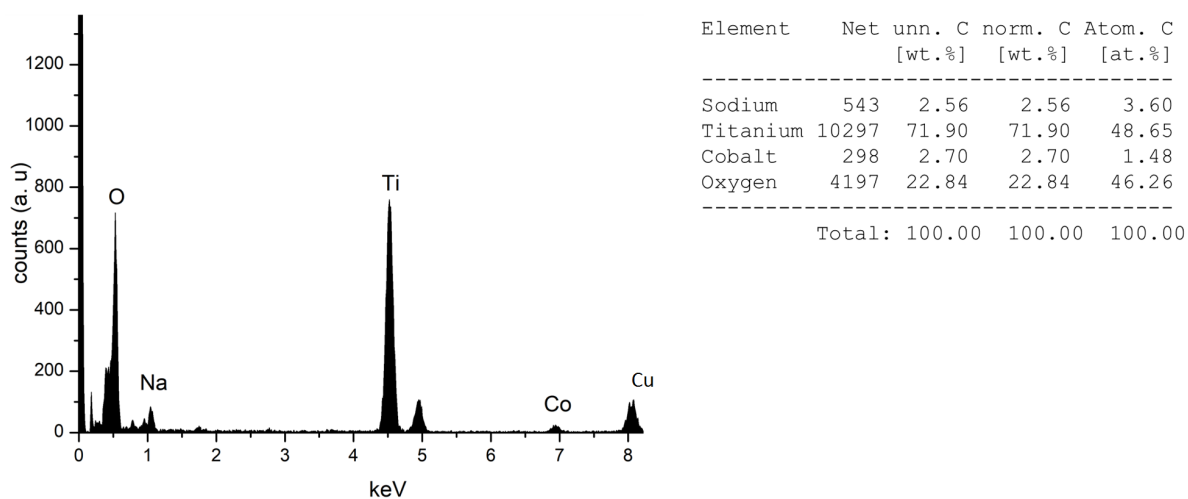


Figure 4.17: EDX spectrum and quantification for Co(5%) TNW sample.

4.3.1 TNW-Co(5%)

Electron microscopy investigations using STEM imaging and EDX analysis on TNW-Co(5%) is shown below. Figure 4.18 and Figure 4.19 shows the low magnification and high magnification images of the TNW Co(5%). From the images, it can be seen that the morphology is of a nanowire as expected from the synthesis. From the EDX maps 4.20 and spectrum 4.21 it can be seen that Co is present in the sample. The quantification gives Co as 3.28 at%. The diameter obtained is between 5 nm and 10 nm and the interlayer spacing obtained is between 0.6 nm and 0.9 nm.

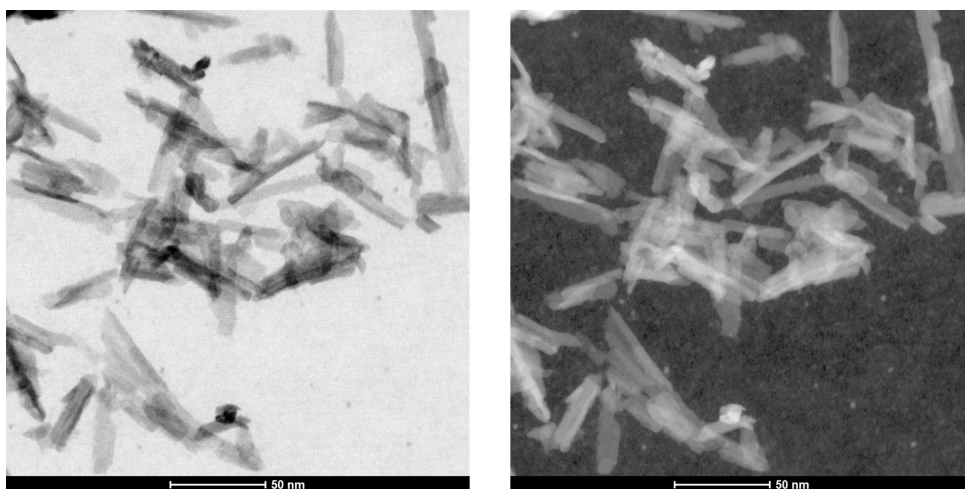


Figure 4.18: STEM BF image (left) and HAADF image (right) of TNW Co(5%)

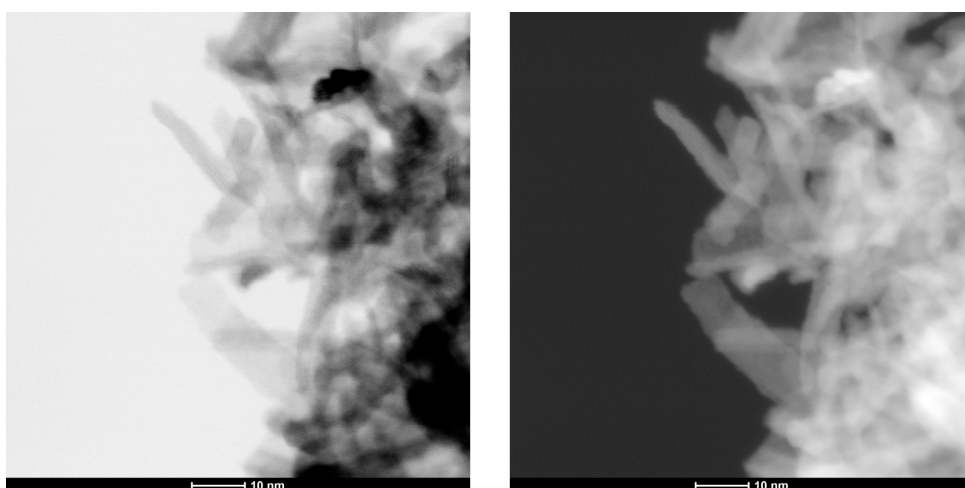


Figure 4.19: High magnification STEM BF image (left) and HAADF image (right) of TNW Co(5%).

The Co intercalated TNW analyzed, TNW Co(5%), shows Co greater than 3%. Therefore we can conclude that Co intercalation is more efficient than Co doping in the case of TNW.

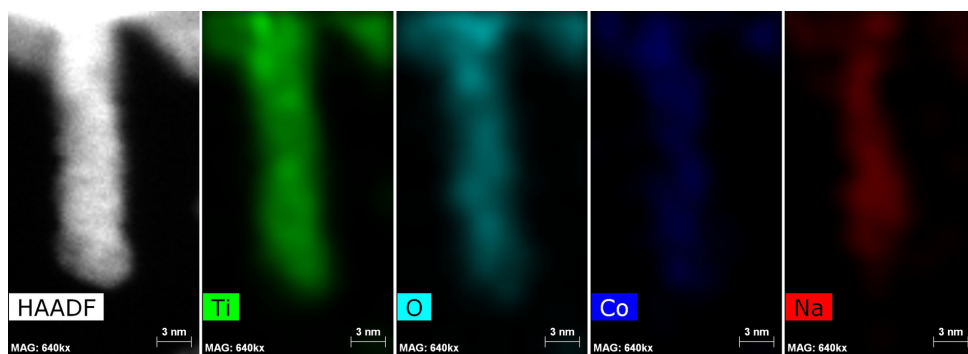


Figure 4.20: EDX map on a single wire of TNW Co(5%).

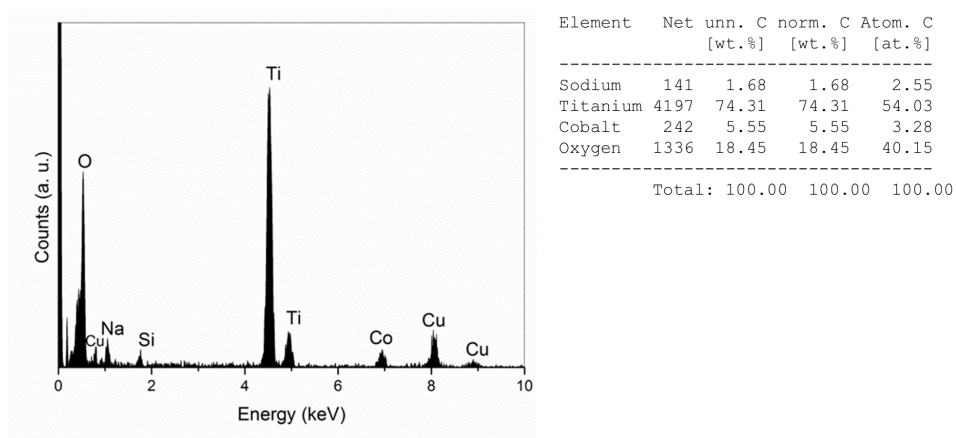


Figure 4.21: EDX spectrum and quantification of TNW Co(5%).

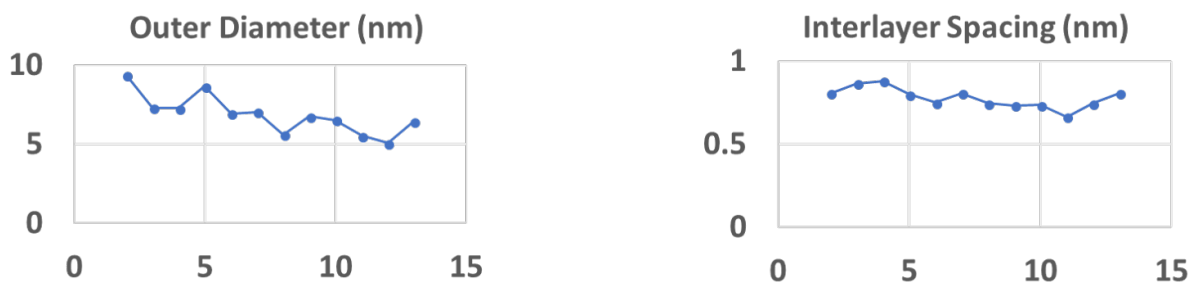


Figure 4.22: Diameter and interlayer spacing measured in TNW Co(5%) sample.

4.4 Co doped titanate nanotubes

The TNT samples modified by doping with cobalt are investigated by electron microscopy and are discussed below.

4.4.1 Co(1%)-TNT

Electron microscopy investigations using STEM imaging and EDX analysis on Co(1%) TNT is shown below. Figure 4.23 and Figure 4.24 shows the low magnification and high magnification images of the Co(1%) TNT. From the images, it can be seen that the morphology is of a nanotube as expected from the synthesis. From the EDX maps 4.25 and spectrum 4.26 it can be seen that Co is present in the sample in small quantities. The quantification gives Co as 0.50 at%.

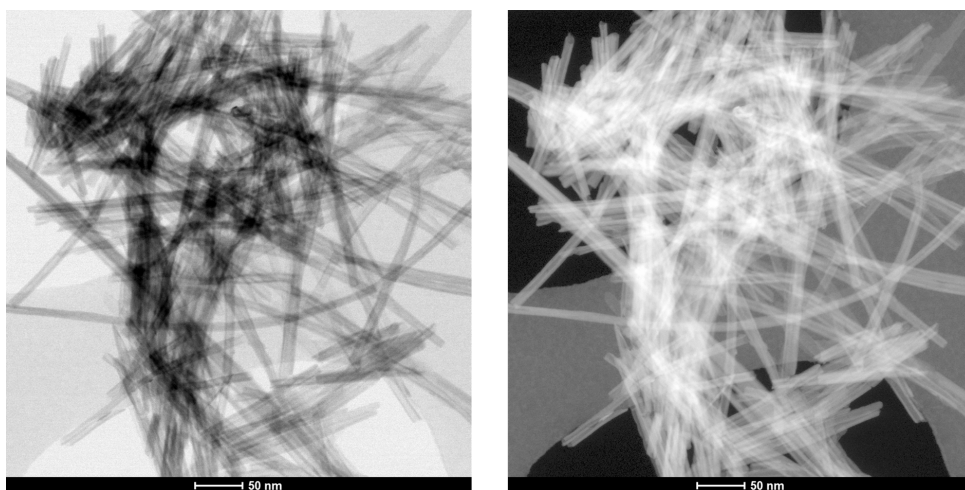


Figure 4.23: STEM BF image (left) and HAADF image (right) of Co(1%)-TNT .

4.4.2 Co(2.5%)-TNT

Electron microscopy investigations using STEM imaging and EDX analysis on Co(2.5%) TNT is shown below. Figure 4.27 and Figure 4.28 shows the low magnification and high magnification images of the Co(2.5%) TNT. From the images, it can be seen that the morphology is of a nanotube as expected from the synthesis. The STEM EDX maps of a single tube showing the elemental distribution of Co, Ti, O and Na are shown 4.29 and from spectrum 4.30 it can be seen that Co is present in the sample in small quantities. The EDX map also confirms the purity of the nanotube sample, as all the peaks observed were identified to be that of Ti, O, Na and Co. The quantification gives Co as 0.37 at% although expected composition was Co 2.5 at%. The interlayer spacing and diameter of

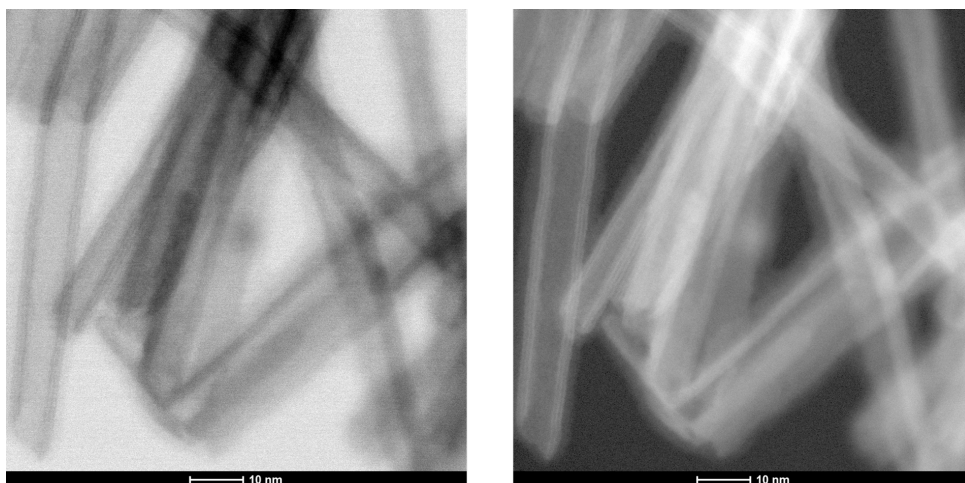


Figure 4.24: High magnification STEM BF image (left) and HAADF image (right) of Co(1%)-TNT.

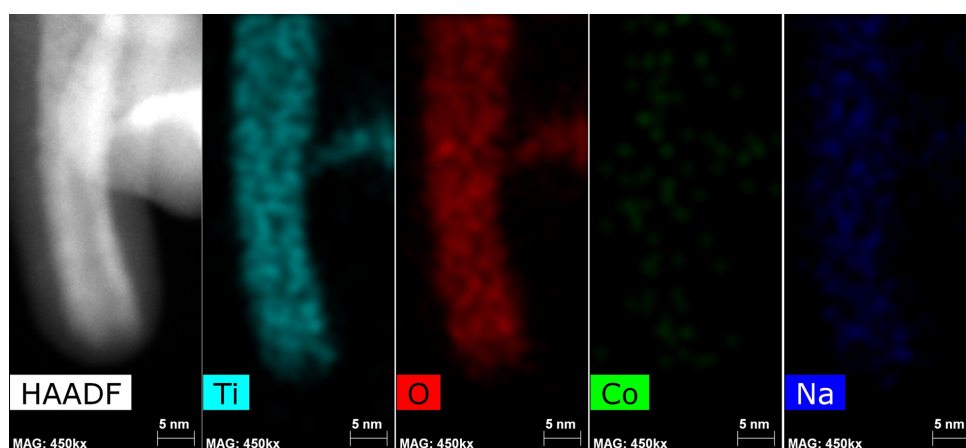


Figure 4.25: EDX map of Co(1%)-TNT.

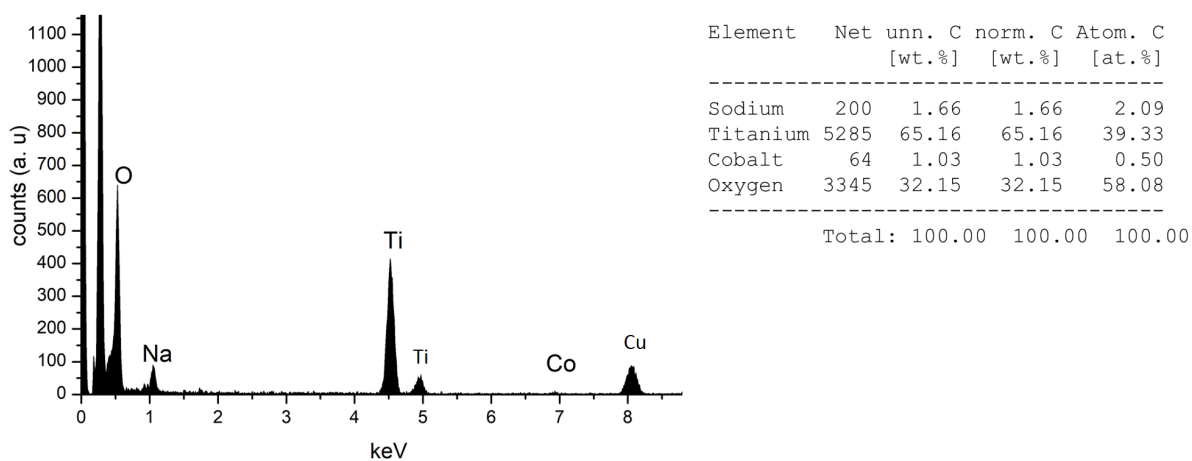


Figure 4.26: EDX spectrum and quantification of Co(1%)-TNT.

nanotubes obtained from HRSTEM and HRTEM image of the specimen are shown in Figure 4.31. The average spacing obtained is 0.76 nm and varies from 0.7 nm to 0.85 nm . HRSTEM image analysis show average diameter of nanotubes as $\sim 9 \text{ nm}$.

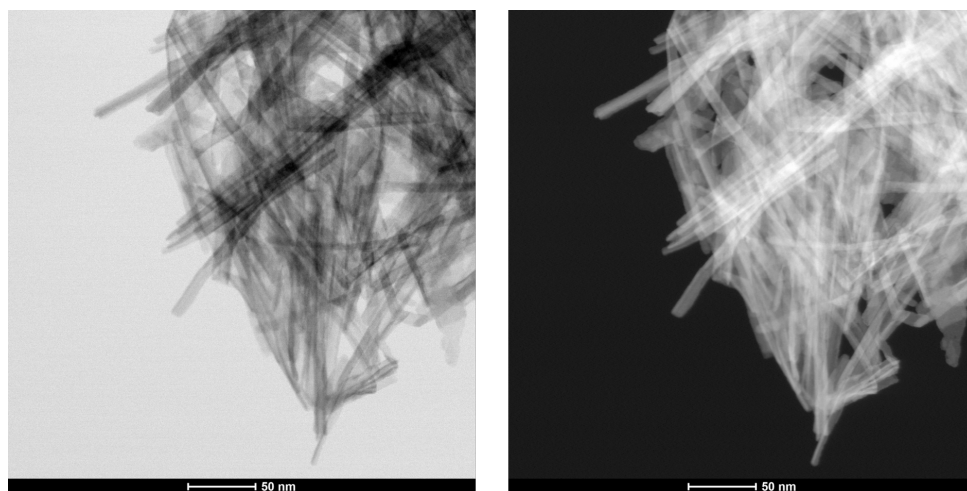


Figure 4.27: STEM BF image (left) and HAADF image (right) of Co(2.5%)-TNT.

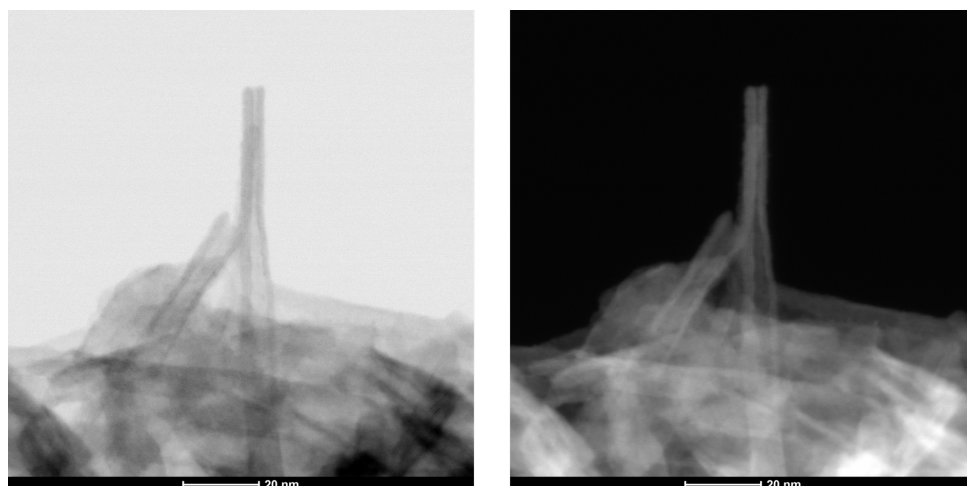


Figure 4.28: High magnification STEM BF image (left) and HAADF image (right) of Co(2.5%)-TNT.

4.4.3 Co(5%)TNT

Electron microscopy investigations using STEM imaging and EDX analysis on Co(5%) TNT is shown below. Figure 4.32 and Figure 4.33 shows the low magnification and high magnification images of the Co(5%) TNT. From the images, it can be seen that the morphology is of a nanotube as expected from the synthesis. TEM images are also shown revealing the (001) planes with average d spacing of 0.69 nm 4.34. From the EDX maps 4.35 and spectrum 4.36 it can be seen that Co is present in the sample in small

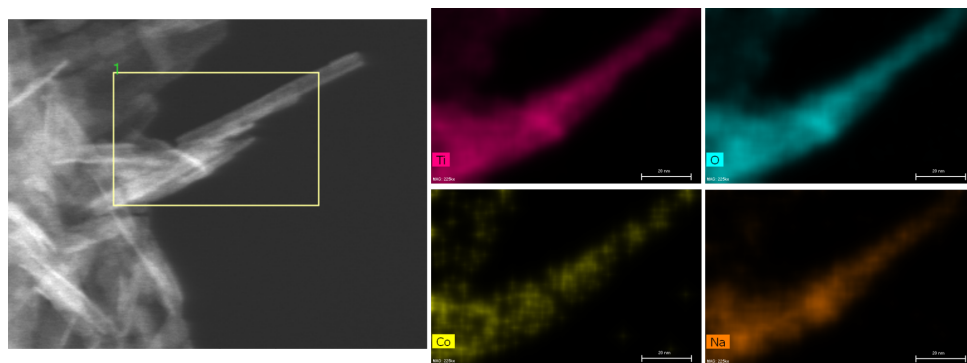


Figure 4.29: EDX map of Co(2.5%)-TNT.

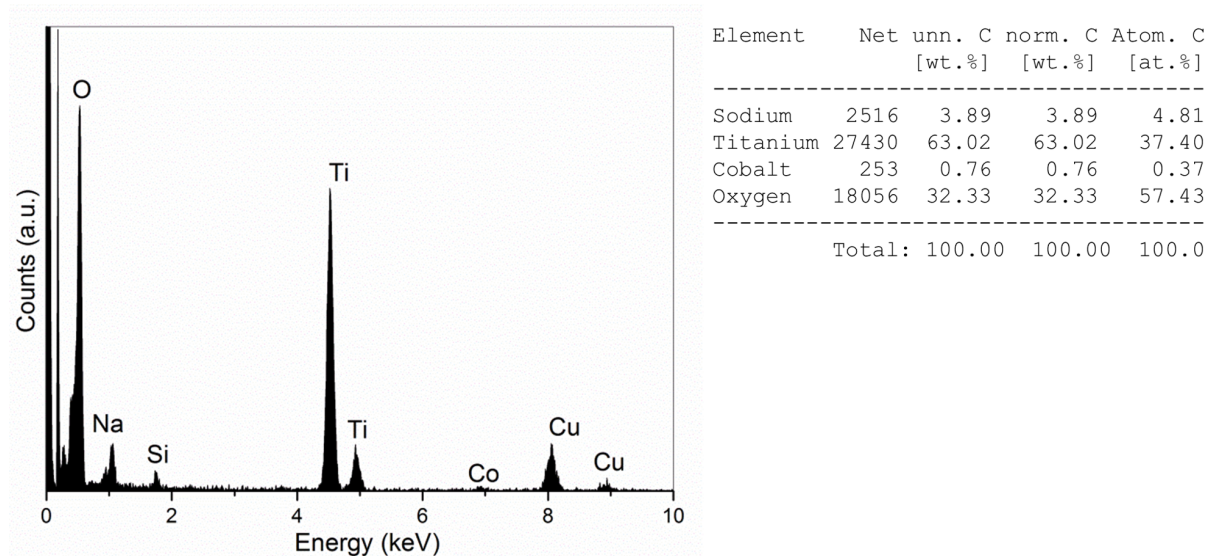


Figure 4.30: EDX spectrum and quantification of Co(2.5%)-TNT.

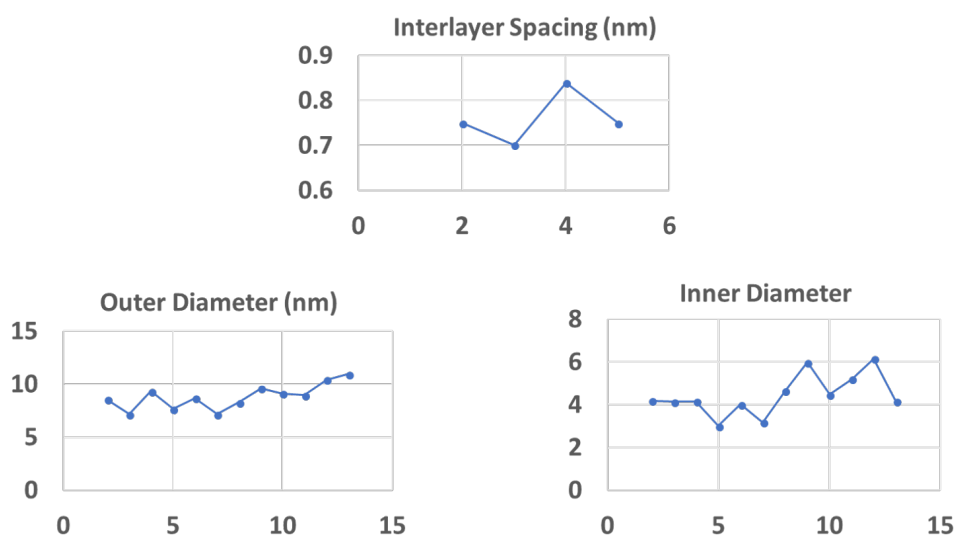


Figure 4.31: Interlayer spacing, outer diameter and inner diameter of Co(2.5%)-TNT.

quantities. The quantification gives Co as 0.53 at%. The interlayer spacings obtained and the diameter distribution are shown in Figure 4.37.

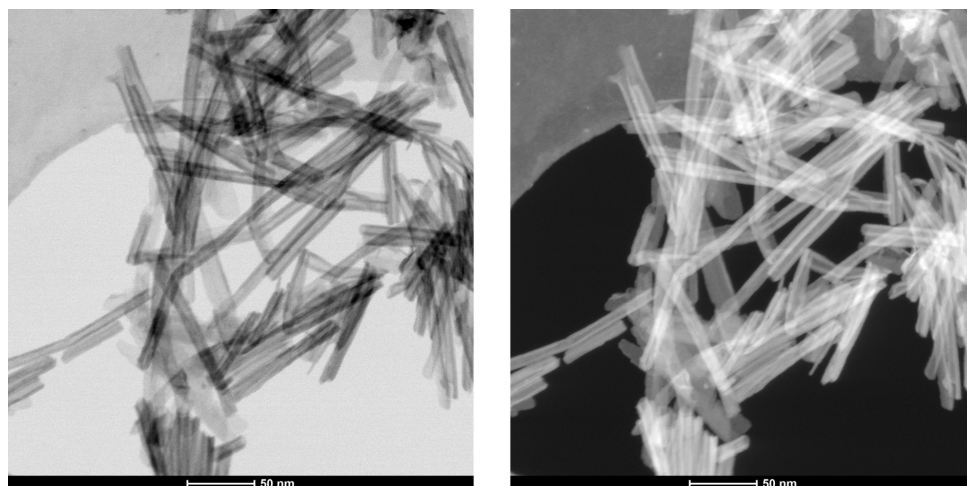


Figure 4.32: STEM BF image (left) and HAADF image (right) of Co(5%)-TNT.

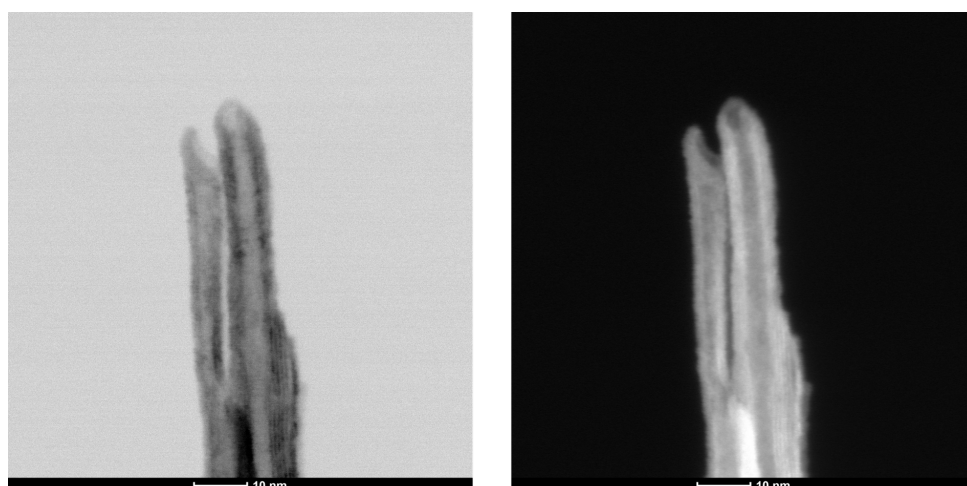


Figure 4.33: High magnification STEM BF image (left) and HAADF image (right) of Co(5%)-TNT.

From the analysis of Co doped TNT samples, we observe that the doping is not achieved to the expected level. Co percentage obtained are less than 1% in all the samples analyzed, including the 5% doped TNT.

4.5 Co intercalated titanate nanotubes

4.5.1 TNT-Co(1%)

Electron microscopy investigations using STEM imaging and EDX analysis on TNT-Co(1%) is shown below. Figure 4.38 and Figure 4.39 shows the low magnification

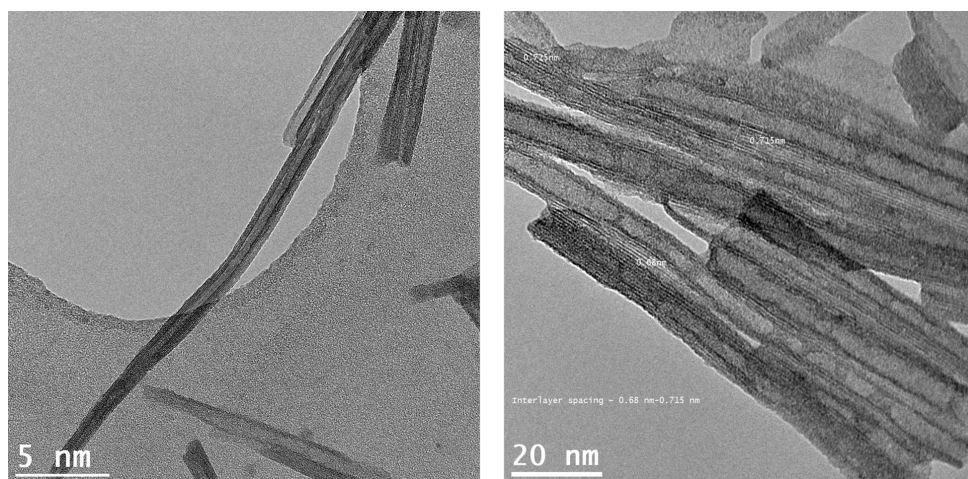


Figure 4.34: Low magnification and HR TEM images of Co(5%)-TNT.

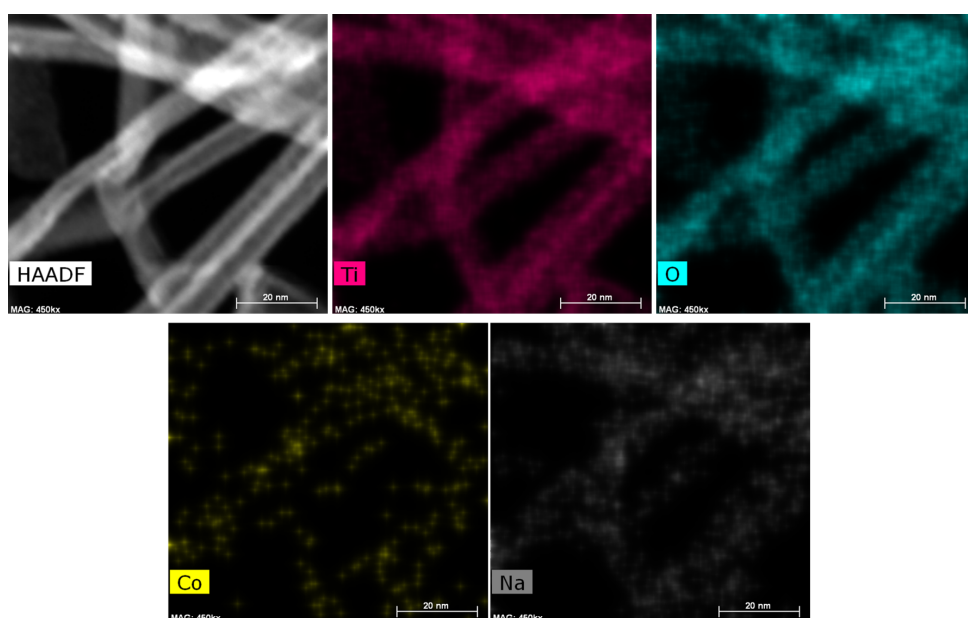


Figure 4.35: EDX map of Co(5%)-TNT.

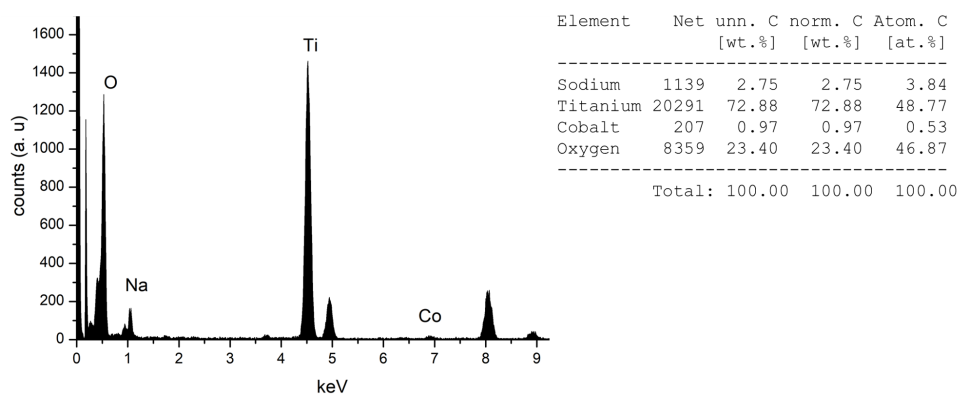


Figure 4.36: EDX spectrum and quantification of Co(5%)-TNT.

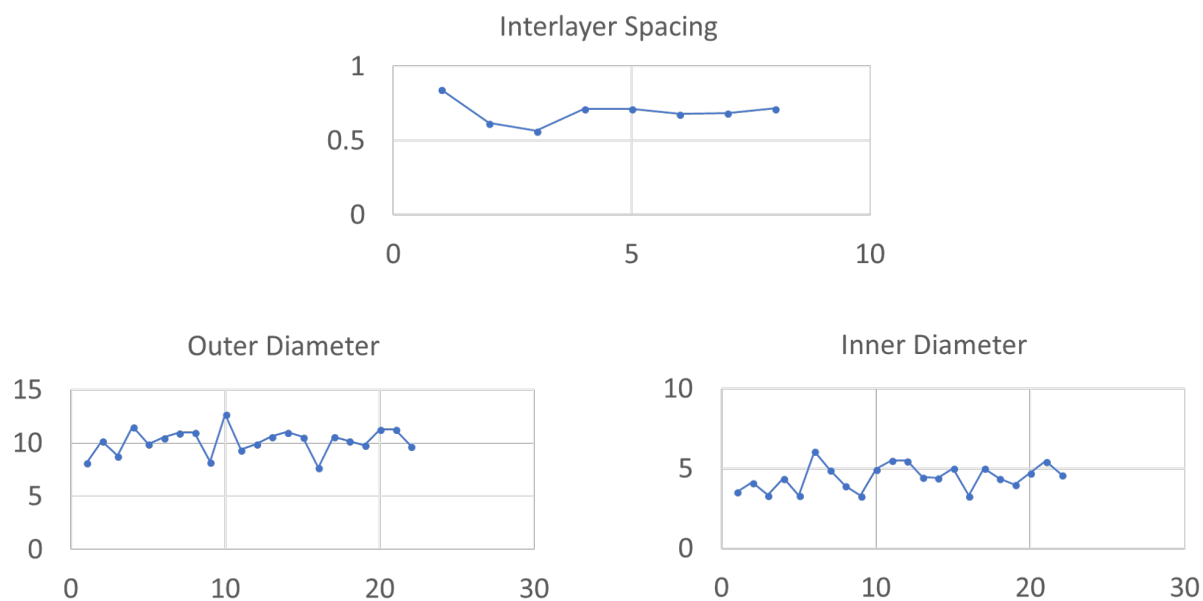


Figure 4.37: Interlayer spacing, outer diameter and inner diameter of Co(5%)-TNT.

and high magnification images of the TNT-Co(1%). From the images, it can be seen that the morphology is of a nanotube as expected from the synthesis. From the EDX maps 4.40 and spectrum 4.41 it can be seen that Co is present in the sample. The quantification gives Co as 1.44 at%.

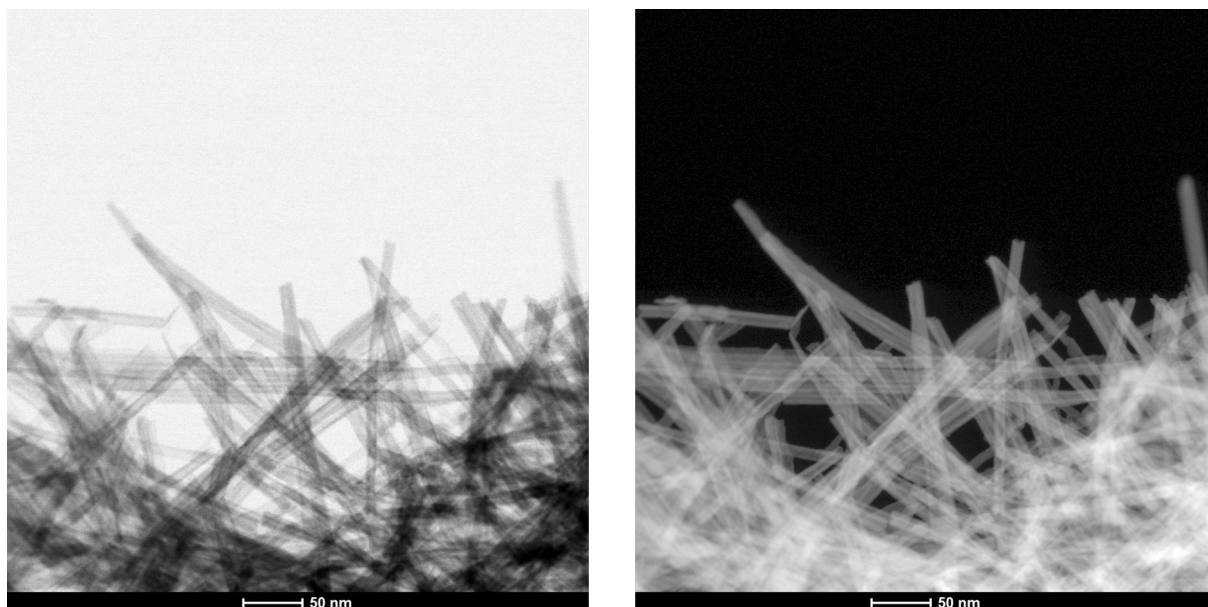


Figure 4.38: STEM BF image (left) and HAADF image (right) of TNT-Co(1%).

4.5.2 TNT-Co(2.5%)

Electron microscopy investigations using STEM imaging and EDX analysis on TNT-Co(2.5%) is shown below. Figure 4.42 and Figure 4.43 shows the low magnification

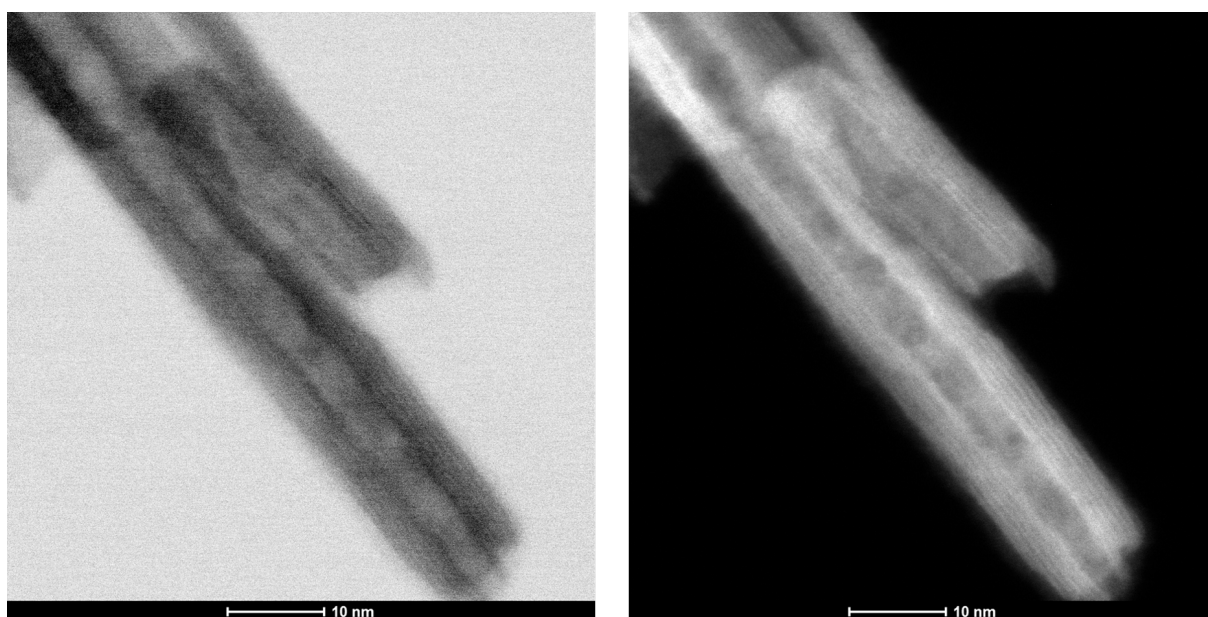


Figure 4.39: High magnification STEM BF image (left) and HAADF image (right) of TNT-Co(1%).

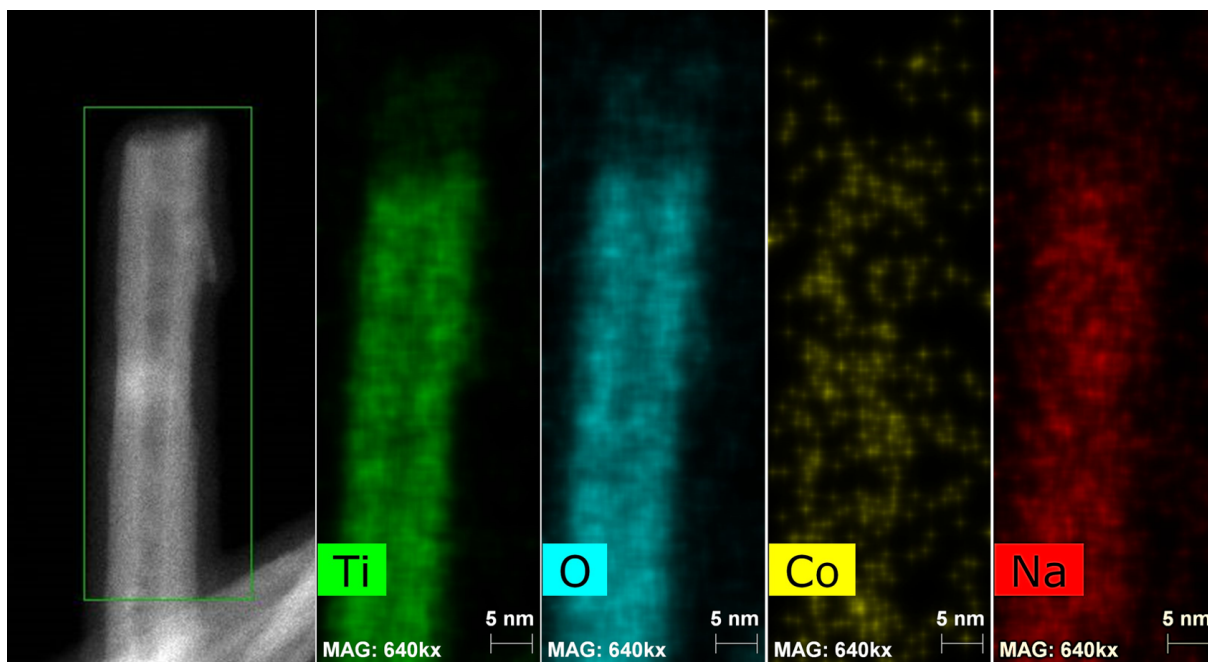


Figure 4.40: EDX map of TNT-Co(1%).

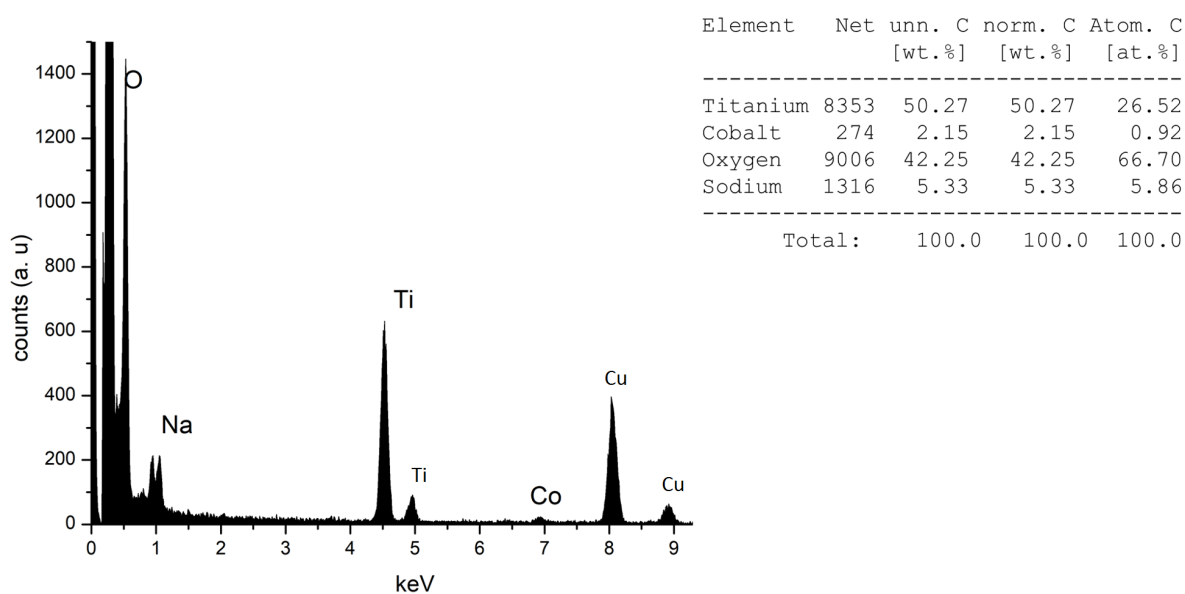


Figure 4.41: EDX spectrum and quantification of TNT-Co(1%).

and high magnification images of the TNT-Co(2.5%). From the images, it can be seen that the morphology is of a nanotube as expected from the synthesis. From the EDX maps [4.44](#) and spectrum [4.45](#) it can be seen that Co is present in the sample. The quantification gives Co as 1.44 at%.

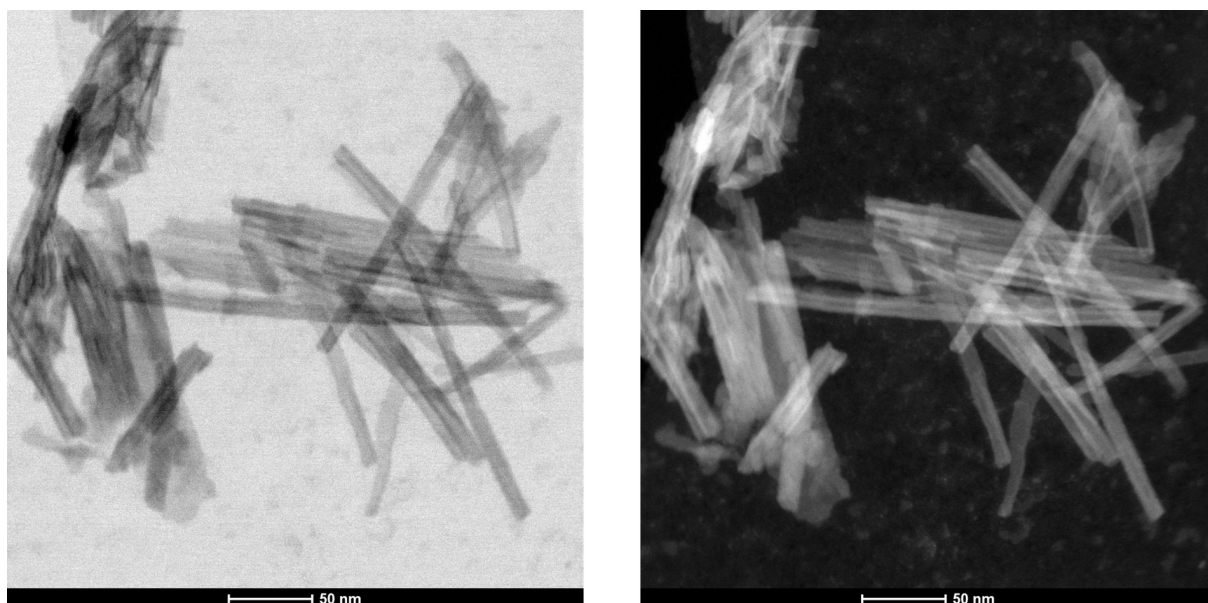


Figure 4.42: STEM BF and HAADF images of TNT-Co(2.5%).

4.5.3 TNT-Co(5%)

Electron microscopy investigations using STEM imaging and EDX analysis on TNT-Co(5%) is shown below. Figure [4.46](#) and Figure [4.47](#) shows the low magnification

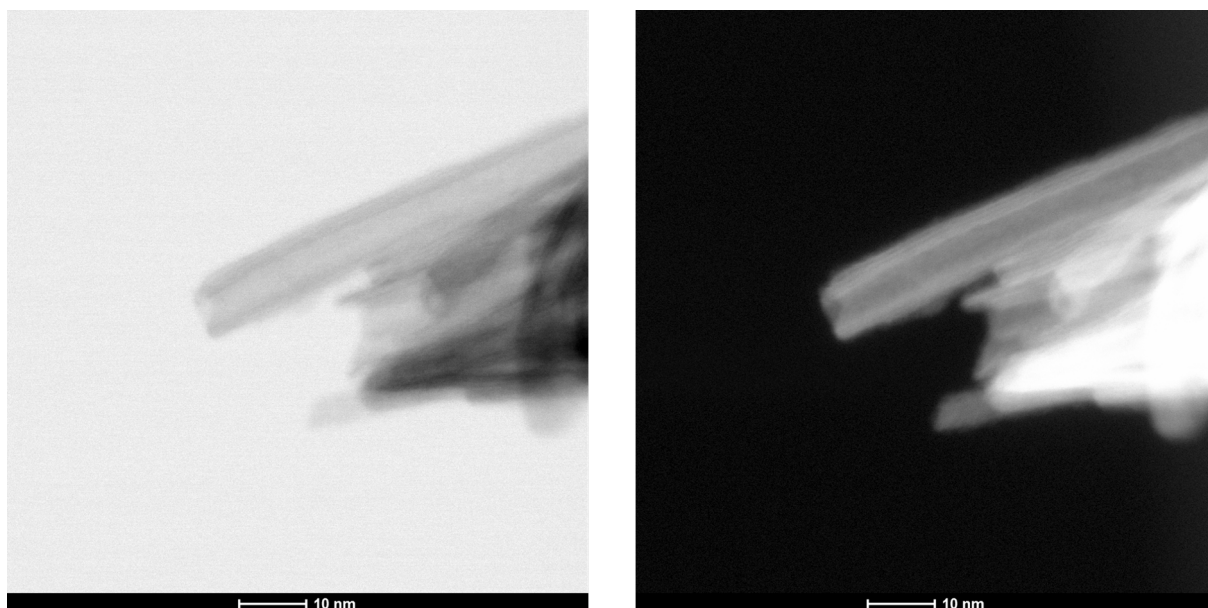


Figure 4.43: High magnification STEM BF image (left) and HAADF image (right) of TNT-Co(2.5%).

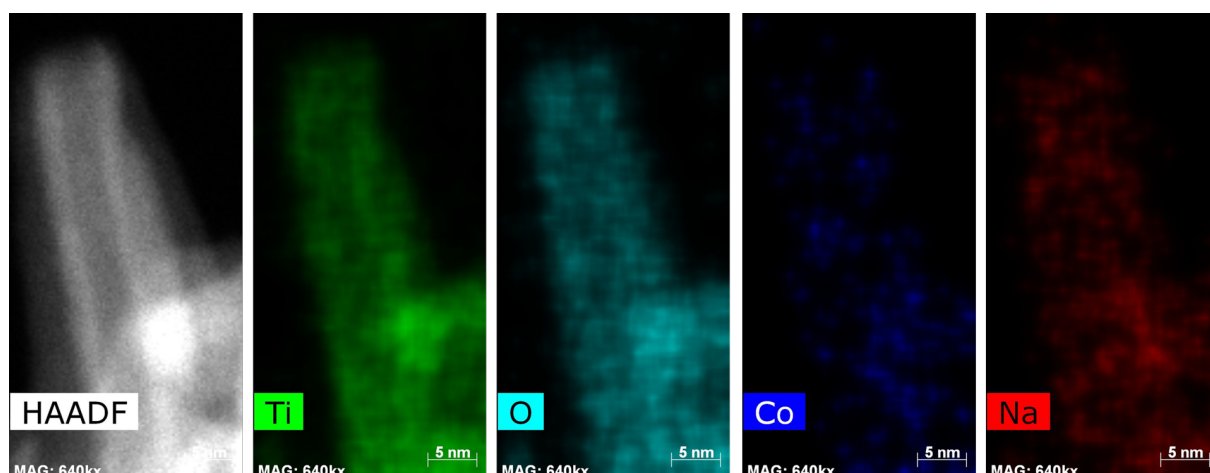


Figure 4.44: EDX map of TNT-Co(2.5%).

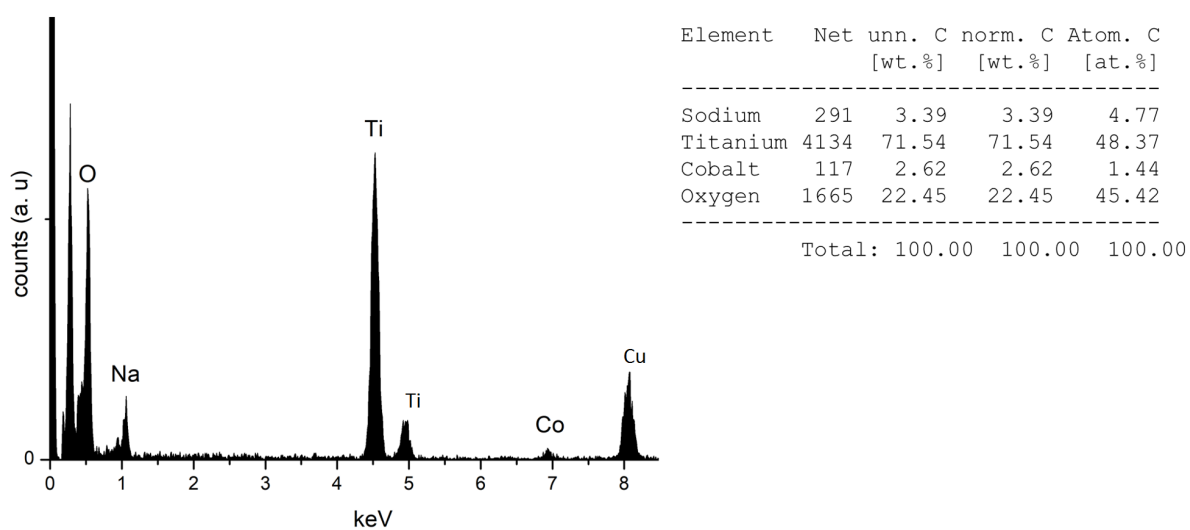


Figure 4.45: EDX spectrum and quantification of TNT-Co(2.5%).

and high magnification images of the TNT-Co(5%). From the images, it can be seen that the morphology is of a nanotube as expected from the synthesis. HRTEM images are shown in 4.48. From the EDX maps 4.49 and spectrum 4.50 it can be seen that Co is present in the sample. The quantification gives Co as 3.37 at%. Interlayer spacings, outer diameter and inner diameter are shown in Figure 4.51

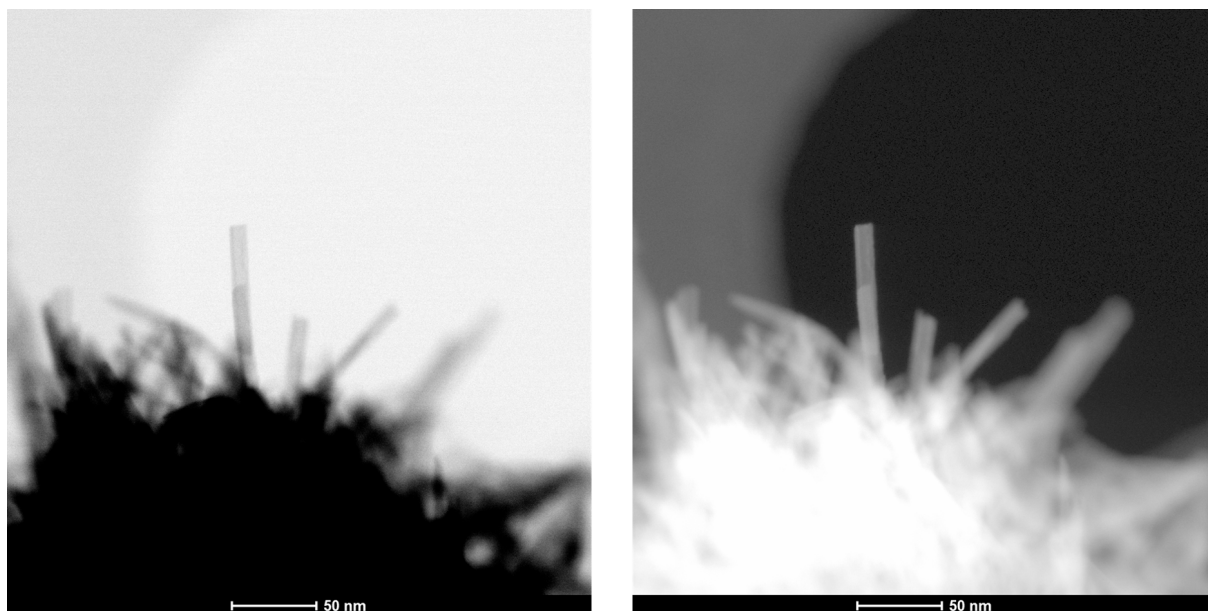


Figure 4.46: STEM BF image (left) and HAADF image (right) of TNT-Co(5%).

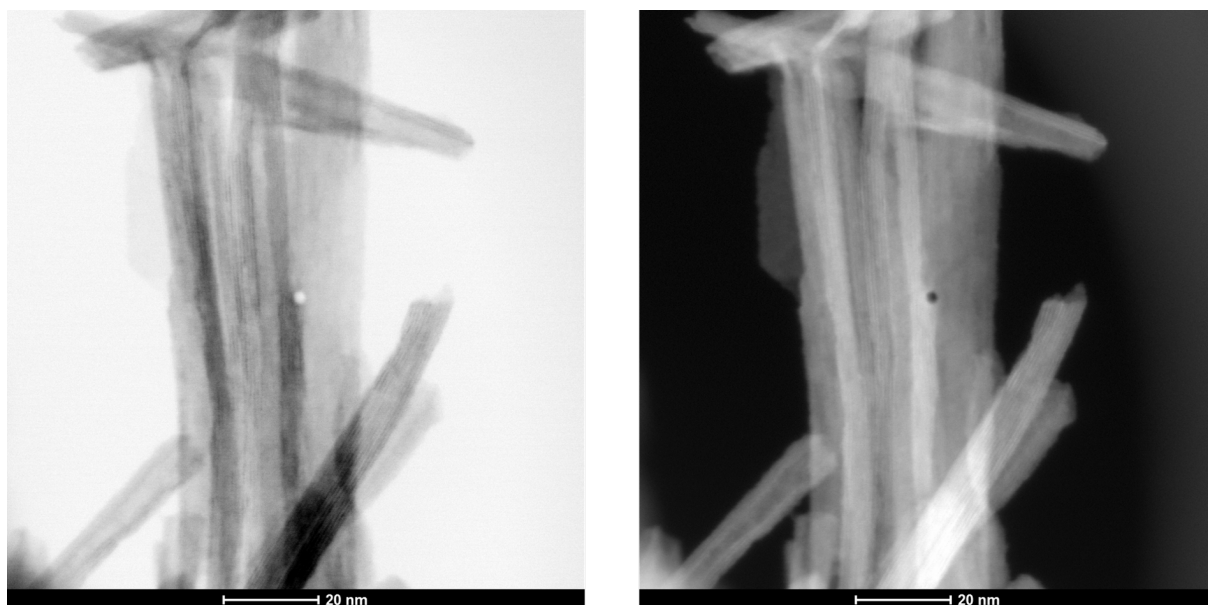


Figure 4.47: High magnification STEM BF image (left) and HAADF image (right) of TNT-Co(5%).

From the analysis of Co intercalated TNT samples, we observe that Co is incorporated into TNT in all the samples analyzed. The intercalation of Co is evidently more efficient

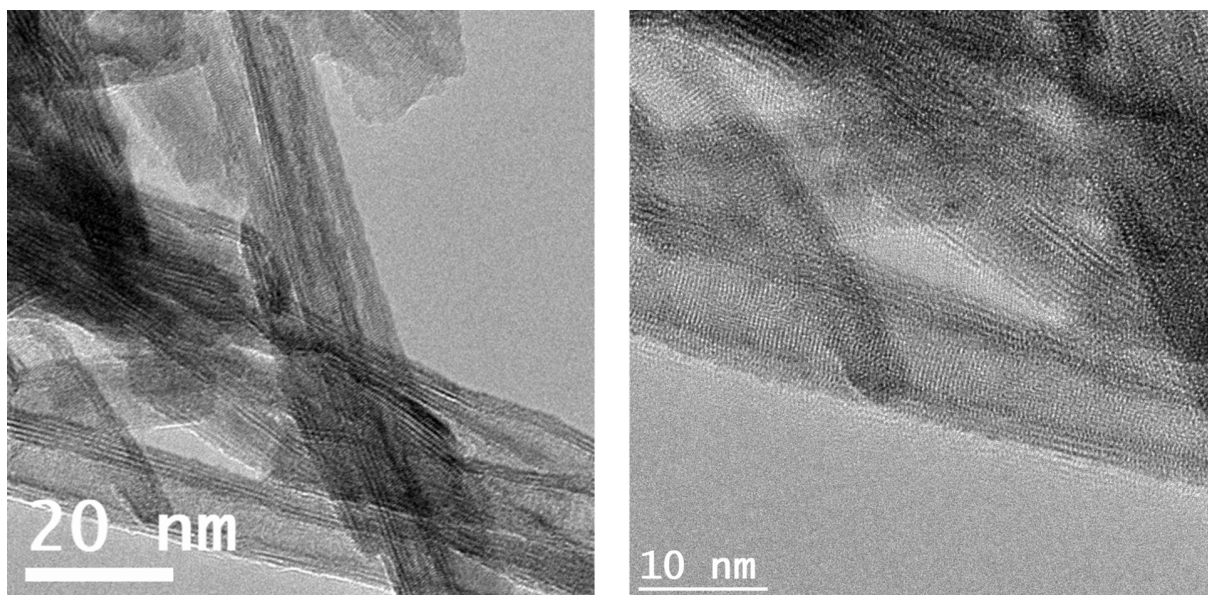


Figure 4.48: HRTEM images of TNT-Co(5%).

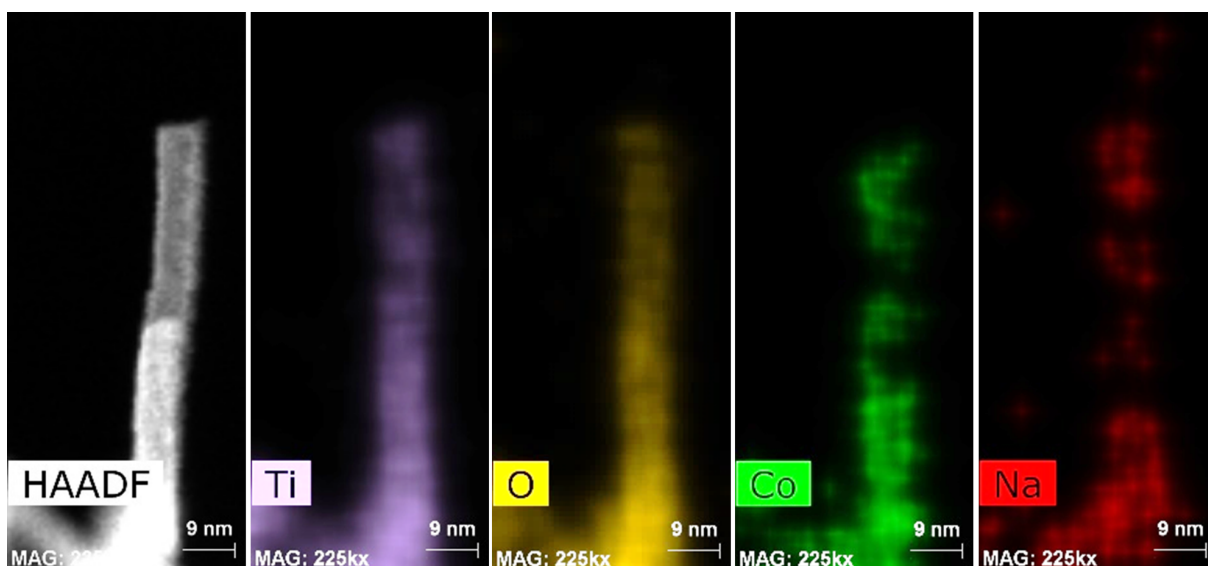


Figure 4.49: EDX mapping of TNT-Co(5%).

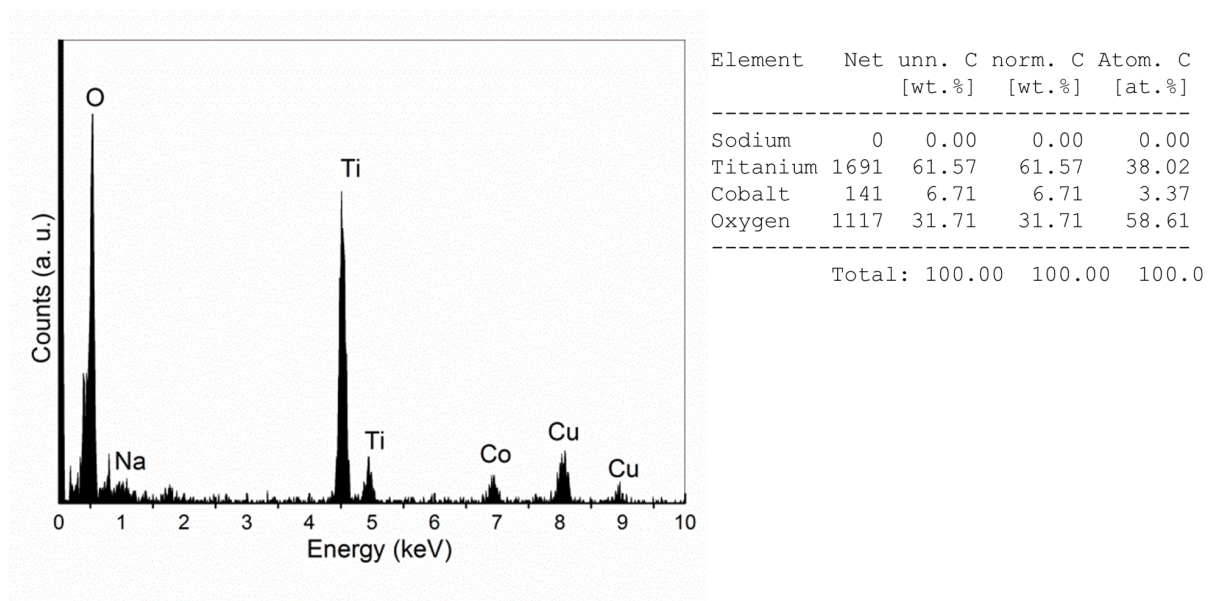


Figure 4.50: Spectrum and quantification of TNT-Co(5%).

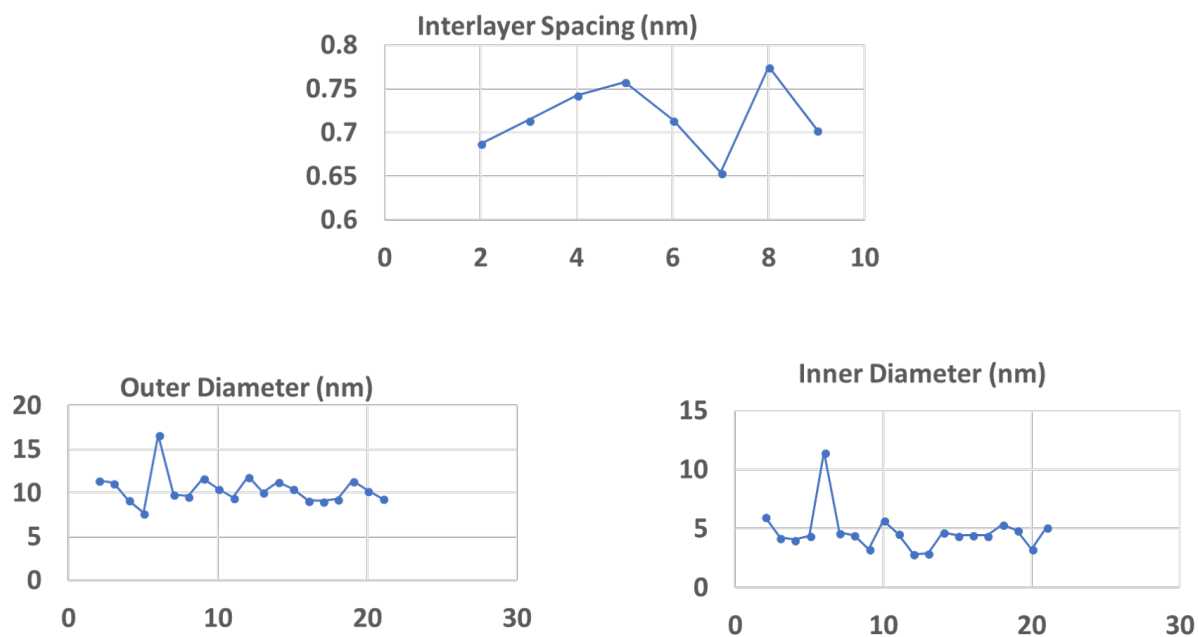


Figure 4.51: Interlayer spacing, outer diameter and inner diameter of TNT-Co(5%).

than Co doping in the case of TNT as well, as that of TNW.

4.6 Comparison between the doped and intercalated nanostructures

The summary of doped Co(2.5%)TNT, doped Co(1%)TNW, intercalated TNT-Co(5%) and intercalated TNW-Co(5%) is shown in the table in figure 4.52. Figure 4.53 shows table with the quantification results from EDX and EELS spectroscopy.

| Sample | Avg Interlayer Spacing (nm) | Avg Dia (nm) | Avg Inner Dia(nm) |
|-------------|-----------------------------|--------------|-------------------|
| TNW | 0.73 | 6.72 | |
| TNT | 0.76 | 9.156 | 3.79 |
| Co(2.5%)TNT | 0.76 | 9 | 4.43 |
| Co(5%)TNT | 0.69 | 10.8 | 4.46 |
| Co(1%)TNW | 0.73 | 6.5 | - |
| Co(5%)TNW | 0.81 | 10.29 | 5.09 |
| TNT Co(5%) | 0.72 | 10 | 4.76 |
| TNW Co(5%) | 0.78 | 7 | - |

Figure 4.52: Comparison between the doped and intercalated nanostructures:Interlayer spacing and diameter

| Sample | EDS (At%) | | | |
|--------------|-----------|-------|-------|------|
| | Co | Ti | O | Na |
| TNW | | 29.38 | 64.56 | 6.06 |
| TNT | | 38.34 | 58.59 | 3.07 |
| Co(1%)TNW | 0.32 | 33.16 | 59.31 | 7.22 |
| Co(5%)TNW | 1.48 | 48.65 | 46.26 | 3.60 |
| Co(1%)TNT | 0.50 | 39.33 | 58.08 | 2.09 |
| Co(2.5%)TNT | 0.37 | 37.40 | 57.43 | 4.81 |
| Co(5%)TNT | 0.53 | 48.77 | 46.87 | 3.84 |
| TNT Co(1%) | 0.92 | 26.52 | 66.70 | 5.86 |
| TNT Co(2.5%) | 1.44 | 48.37 | 45.42 | 4.77 |
| TNW Co(5%) | 3.28 | 54.03 | 40.15 | 2.55 |
| TNT Co(5%) | 3.37 | 38.02 | 58.61 | 0.0 |

Figure 4.53: EDS quantification of doped and intercalated titanate nanostructures

4.7 EELS Analysis

In order to quantify or to extract the edge intensity, we have to fit , extrapolate, and then subtract the background using an appropriate background model [Gatan](#). Figure

4.54 shows a typical spectrum with the parameters which are used for extracting the edge intensity.

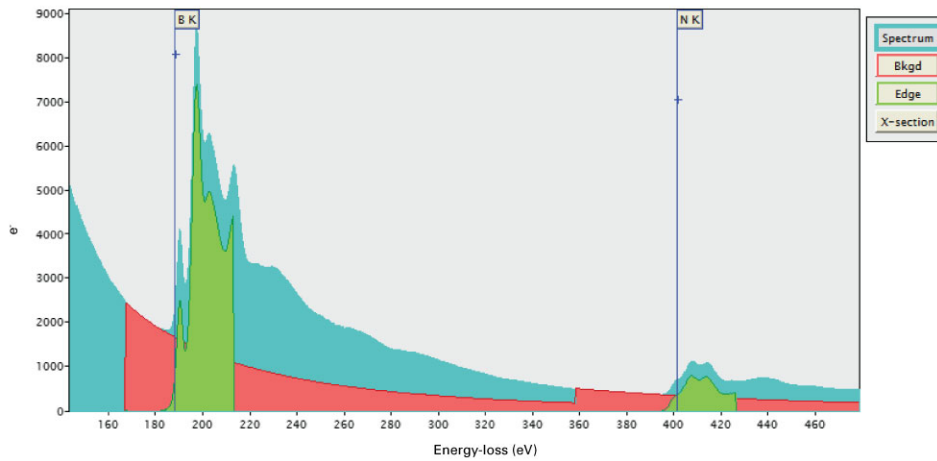


Figure 4.54: EELS signal extraction: figure shows spectrum background, edge and the cross section [Gatan](#)

Background modelling

As discussed earlier we must determine a background model for the raw spectrum. For this a pre edge region for fitting must be identified for determining the other parameters for the fit. This pre edge fit is then extrapolated to estimate the background intensity below the edge signal [Gatan 4.55](#).

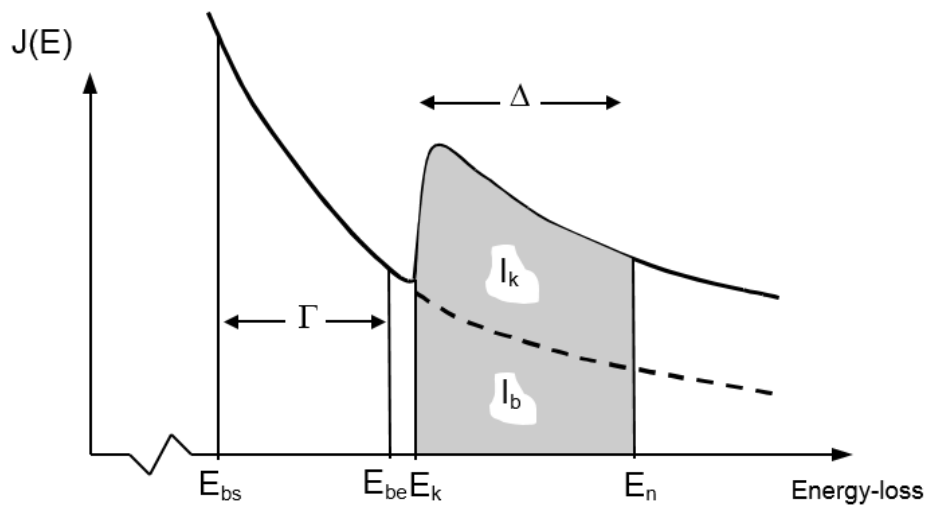


Figure 4.55: Background modelling [Gatan](#)

where,

Γ = background fit window

Δ = signal intensity window

I_b = background intensity

I_k = signal intensity.

A power law is the most common background model which is given by

$$I = AE^{-r} \quad (4.1)$$

where I is the intensity in the channel of energy loss E , and A and r are constants.

4.7.1 EELS elemental mapping

Figure 4.56 shows the EELS elemental mapping of cobalt(5%) doped titanate nanowire (TNW). From the maps we can see that the cobalt is prominent on the wires compared to its surrounding, which suggests that the cobalt was incorporated in the titanate structures. From the titanium map, it appears that titanium is present in the wires as well as in the surrounding matrix. The matrix might be sheets of titanates which did not transform to wires during the synthesis.

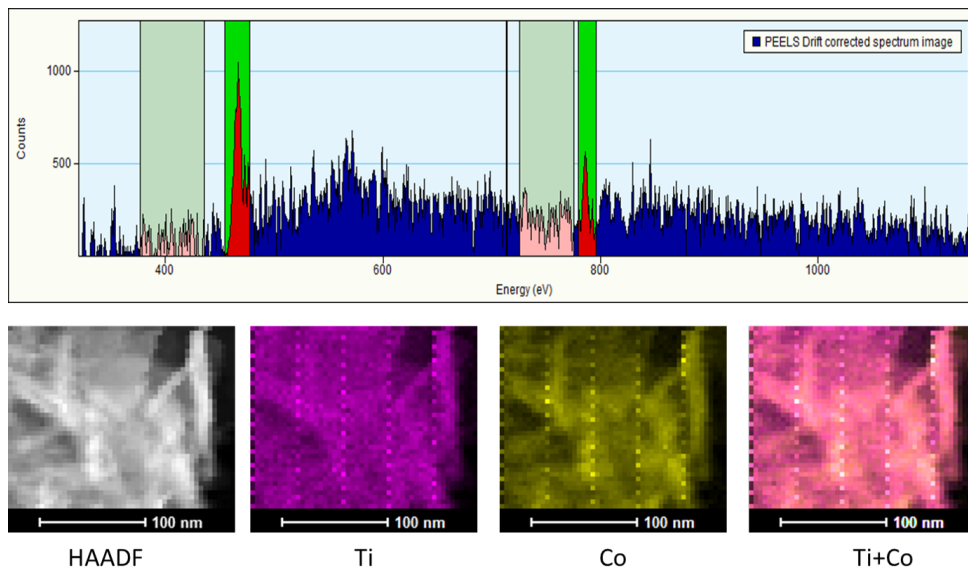


Figure 4.56: EELS elemental mapping of Co(5%)-TNW sample.

4.7.2 EELS quantification

Figure 4.57, shows the EELS quantification details of intercalated TNT-Co(5%)

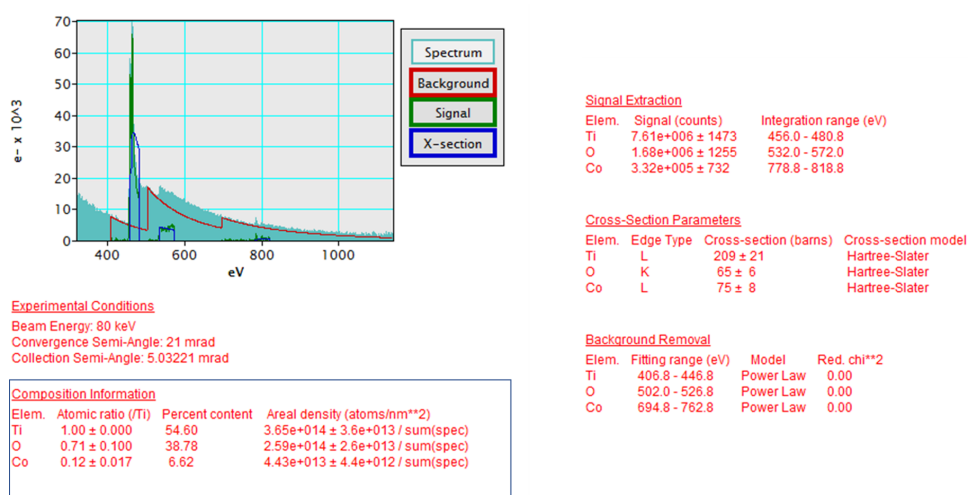


Figure 4.57: EELS spectrum and quantification details of intercalated TNT-Co(5%)

The qualification results for intercalated TNT-Co(5%) and TNW-Co(5%) are shown in figure 4.58 and in figure 4.59.

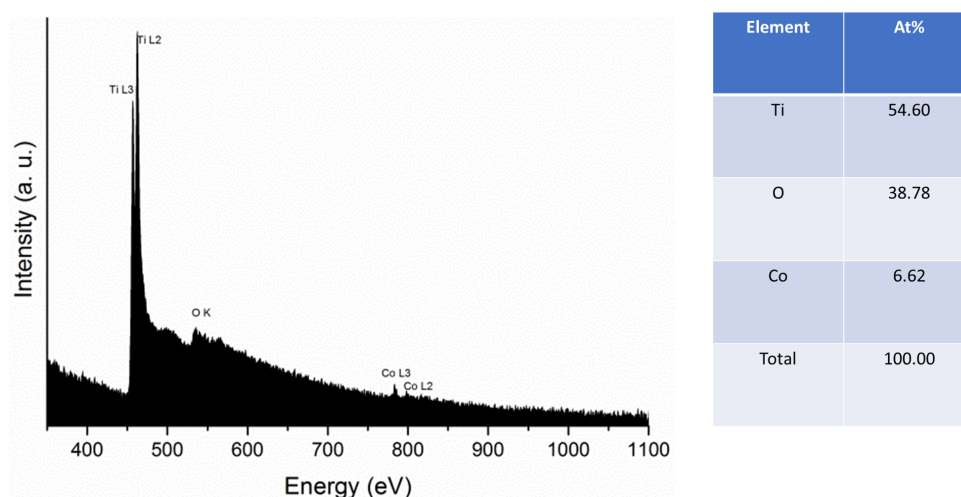


Figure 4.58: EELS spectrum and quantification of intercalated TNT-Co(5%)

4.8 Cobalt valence in titanate nanostructures by EELS

As discussed in the previous chapter electron energy loss spectroscopy (EELS), is a powerful technique for materials characterization at a nanometer spatial resolution, and has been widely used in chemical microanalysis.

In EELS, the L ionization edges of transition-metals and rare-earth elements usually display sharp peaks at the near-edge region, which are known as white lines. For transition metals with unoccupied 3d states, the transition of an electron from 2p state to 3d levels

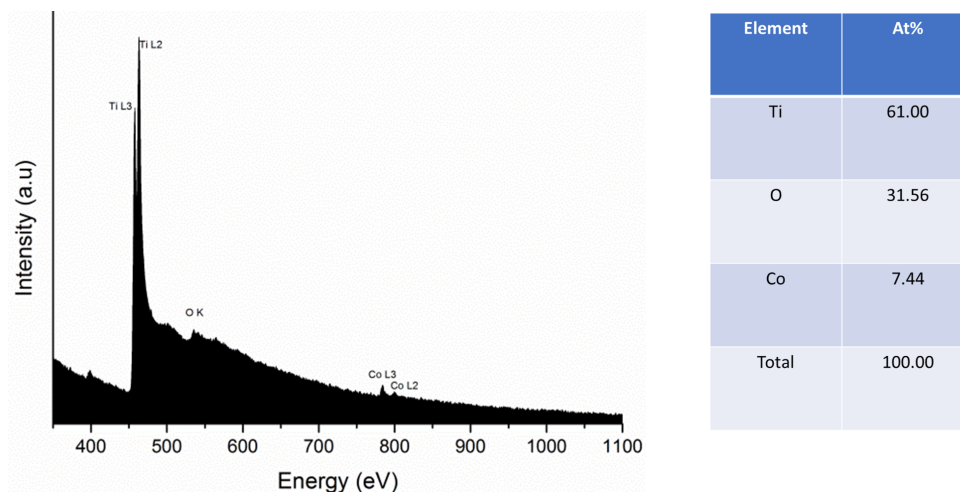


Figure 4.59: EELS spectrum and quantification of intercalated TNW-Co(5%)

leads to the formation of white lines. The $L3$ and $L2$ lines are the transitions from $2p^{3/2}$ to $3d^{5/2}$ and from $2p^{1/2}$ to $3d^{3/2}$, respectively, and their intensities are related to the unoccupied states in the $3d$ bands

For example in figure 4.60 shows EELS spectrum of Co modified Titanate nanostructure acquired at 80 kV using Titan ChemiSTEM transmission electron microscope. The EELS spectra were acquired in probe mode at a magnification which depended on the required spatial resolution and signal intensity.

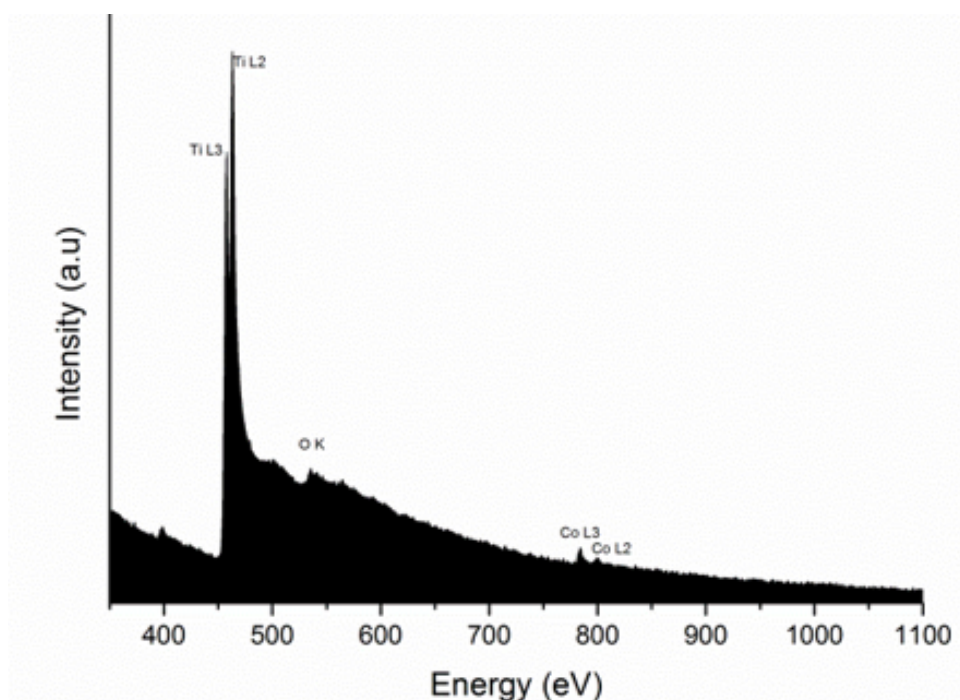


Figure 4.60: EELS spectra of TNW-Co(5%)

The EELS data must be processed first for signal extraction. In general multiple-inelastic-scattering effects due to thickness as well as background need to be

removed before extracting the signal.

In this study we assume that the effects from multiple-inelastic-scattering effects due to thickness is negligible as the samples analysed are less than 10 nm in thickness.

The structure of the EELS spectrum at the $L_{2,3}$ edge is due to the excitations to the bound states and excitations to the continuum. In order to determine the bound states accurately it is necessary to subtract the continuum contribution.

The background subtraction was done following one of the methods from [Pearson et al. \(1988\)](#). In this method a straight line was drawn from the base of the L_3 white line onset to the first minimum, and from there to the intersection of the falling edge of the L_2 white line and the background. The total white line intensity was then obtained by integrating the area under the peaks as shown in figure 4.61.

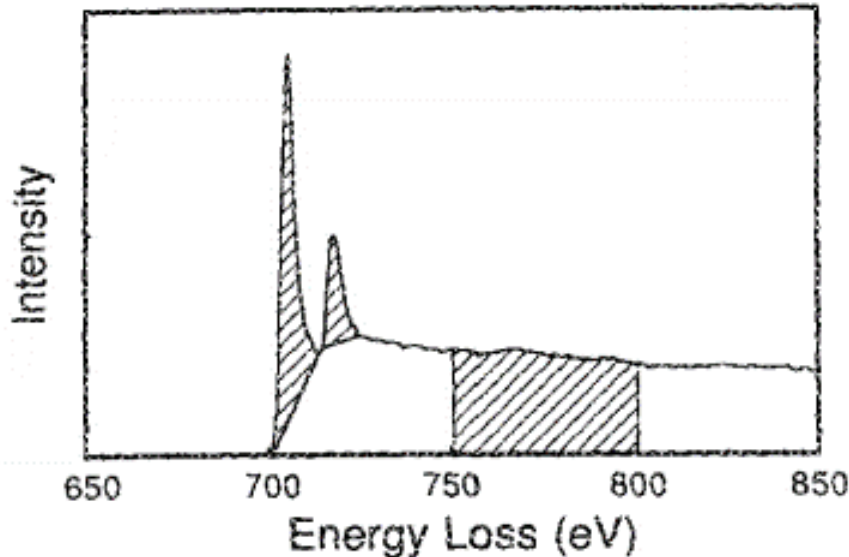
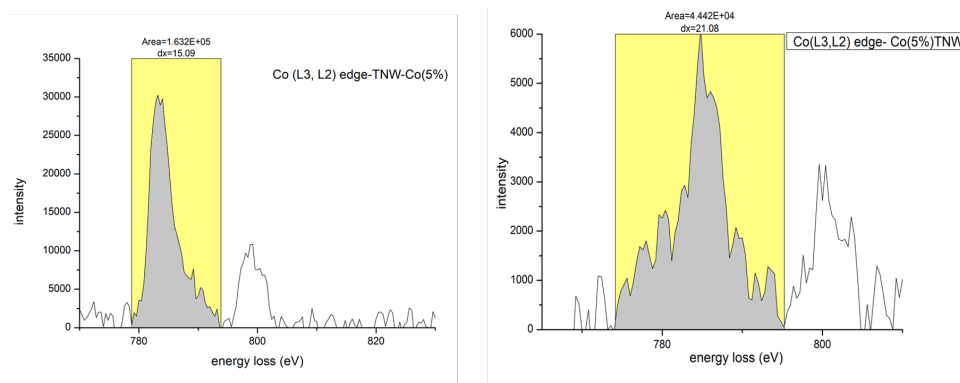
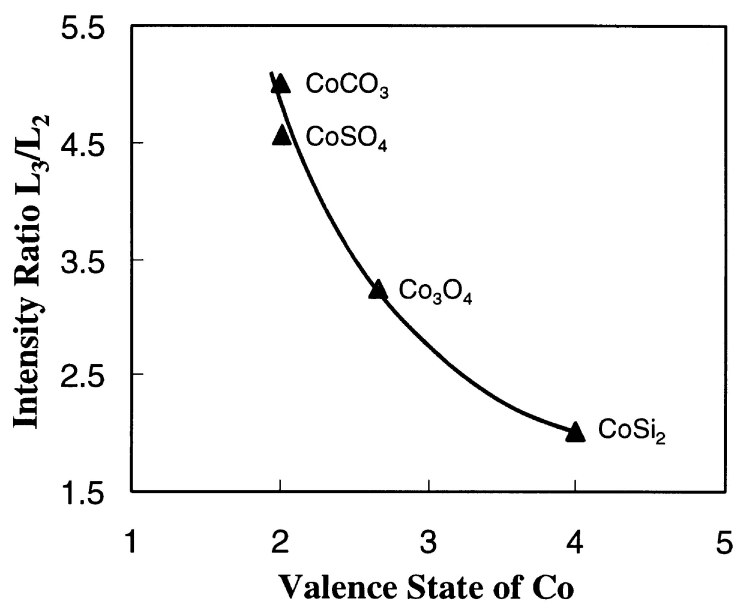


Figure 4.61: Co L_3/L_3 ratio ([Pearson et al., 1988](#)).

The table below in figure 4.62 gives L_3/L_2 for intercalated TNW-Co(5%) and doped Co(5%)-TNW. The processed EELS data is shown below in the figure 4.63 for the intercalated and for the doped titanate nanowires. The L_3/L_2 ratios for a few standard Co compounds are shown in figure 4.64. EELS spectra of Co $L_{2,3}$ ionization edges were acquired from CoSi_2 (with Co^{4+}), Co_3O_4 (with $\text{Co}^{2.67+}$), CoCO_3 (with Co^{2+}) and CoSO_4 (with Co^{2+}). [Wang et al. \(2000\)](#)

Comparison with the experimentally measured intensity ratios of L_3/L_2 for intercalated TNW-Co(5%) and doped Co(5%)-TNW with that of the standard compounds suggests that in the intercalated TNW-Co(5%) sample, cobalt is mostly in 2+ state and for the doped Co(5%)-TNW, cobalt is mainly in a mixed state of Co^{2+} and Co^{3+} .

| Sample | L3 Intensity (Area) | L2 Intensity (Area) | Intensity Ratio L3/L2 |
|------------|---------------------|---------------------|-----------------------|
| TNW-Co(5%) | 1.632E+05 | 4.819E+04 | 3.38 |
| Co(5%)-TNW | 4.442E+04 | 1.570E+04 | 2.83 |

Figure 4.62: Co L₃/L₂ ratioFigure 4.63: Co L_{2,3} edge of cobalt(5%) intercalated and doped titanate nanowiresFigure 4.64: Co L₃/L₂ ratio Wang et al. (2000)

4.9 X-ray photoelectron spectroscopy

In this study, XPS is used to characterize the doped and intercalated titanate nanostructures. One of the main objective of XPS is to identify the location of Co, that is whether it is replacing the Ti in the TiO_6 octahedra or replacing Na between the TiO_6 layers. Another objective is to identify the oxidation state of Co in the titanates. Figure 4.65 shows Co2p XPS spectra of doped (Co5%)-TNT and of doped (Co5%)-TNW. Similarly figure 4.66 shows Co2p XPS spectra of intercalated TNT-Co(5%) and of TNW-Co(7.5%). Previous reports on Co doped titanates show that Co 2p peaks are accompanied by satellite peaks separated by 6 eV in the case of Co^{2+} in octahedral environment. In the samples investigated here, the Co 2p satellites are clearly seen which indicates the presence of Co^{2+} . The presence of Co^{3+} will cause a decrease in intensity of the satellite peaks. This indicates that Co is present as 2+ in the intercalated samples (TNT-Co(5%) and TNW-Co(7.5%)) but as a mixture of Co^{2+} and Co^{3+} in the doped samples (Co(5%)-TNT) and Co(5%)-TNW) [Biesinger et al. \(2011\)](#).

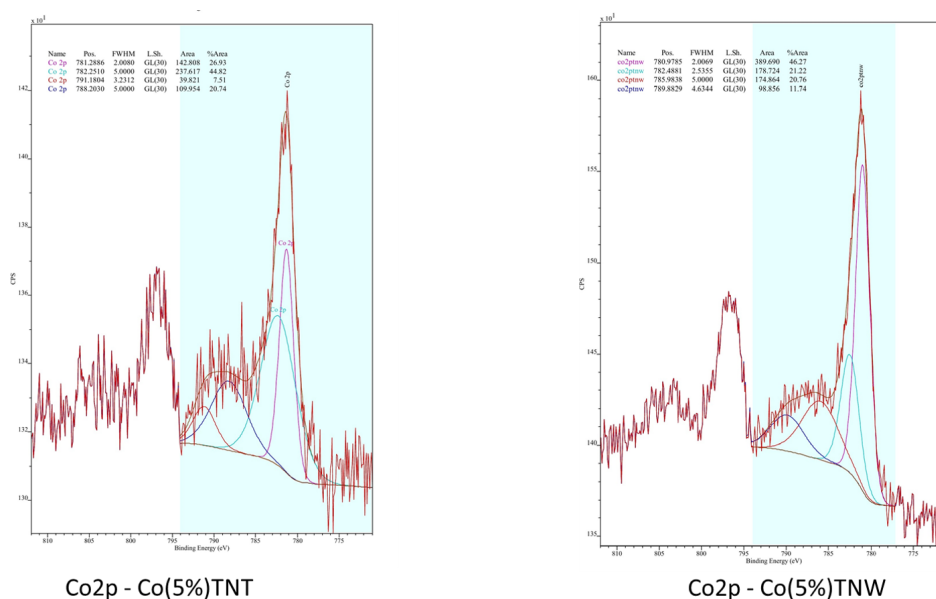


Figure 4.65: Co2p XPS spectra of doped Co(5%)-TNT and Co(5%)-TNW

Titanium binding energies are similar to the binding energies of the 4+ oxidation state of titanium. The XPS quantification data is shown in figure 4.67 for the intercalated samples of TNW and TNT. From the data it is clear that the sodium content is decreasing with increasing cobalt content which validates that cobalt is substituting for sodium in between the layers of the titanate nanostructures.

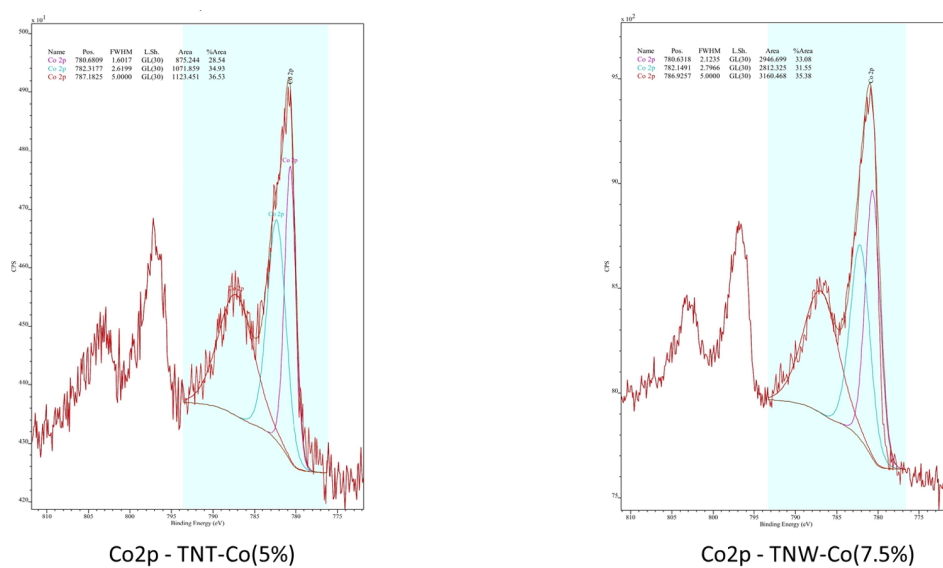


Figure 4.66: Co2p XPS spectra of intercalated TNT-Co(5%) and TNW-Co(7.5%)

| Element | TNW-Co(1%) | TNW-Co(2.5%) | TNW-Co(7.5%) | TNW-Co(10%) |
|---------|------------|--------------|--------------|-------------|
| C 1s | 19.4 | 20.9 | 18.9 | 20.8 |
| O 1s | 51.8 | 52.3 | 53.1 | 51.9 |
| Na 1s | 9.0 | 7.7 | 4.9 | 3.7 |
| Ti 2p | 19.3 | 18.0 | 20.4 | 20.1 |
| Co 2p | 0.5 | 1.1 | 2.7 | 3.5 |

| Element | TNT-Co(1%) | TNT-Co(2.5%) | TNT-Co(5%) | TNT-Co(10%) |
|---------|------------|--------------|------------|-------------|
| C 1s | 14.6 | 14.7 | 19.0 | 26.5 |
| O 1s | 54.8 | 54.6 | 52.3 | 49.6 |
| Na 1s | 8.1 | 7.3 | 5.8 | 2.9 |
| Ti 2p | 22.1 | 22.5 | 20.8 | 18.0 |
| Co 2p | 0.37 | 0.97 | 2.09 | 2.95 |

Figure 4.67: XPS quantification results of intercalated TNW's and TNT's

For the doped samples the doping is relatively less compared to the intercalated samples of similar nominal cobalt content. Table in figure 4.68 shows the XPS quantification data for (5% cobalt) doped TNT and TNW.

| Element | Co(5%)TNT | Co(5%)TNW |
|---------|-----------|-----------|
| C 1s | 9.97 | 6.55 |
| O 1s | 50.89 | 52.14 |
| Na 1s | 16.37 | 15.97 |
| Ti 2p | 21.75 | 23.56 |
| Co 2p | 1.02 | 1.78 |

Figure 4.68: XPS quantification result of (5% cobalt) doped TNT and TNW

4.10 Raman spectroscopy

Raman spectroscopy was used to further investigate the local structure of the samples. Figure 4.69 shows the Raman spectra for TNT and 5% doped (Co5%TNT) and 5% intercalated TNT (TNT Co5%) samples.

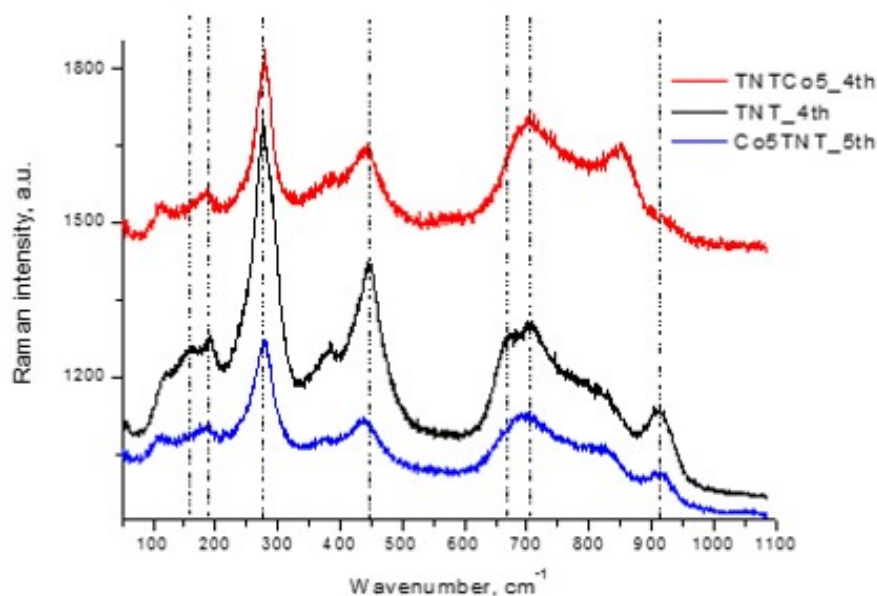


Figure 4.69: Raman spectra of titanate nanotube (TNT) and doped and intercalated titanate nanotube

A comparison of the Raman spectra of the synthesized samples with those reported in the literature shows that the set of observed bands agree well with that of titanate nanotubes ($\text{Na}_2\text{Ti}_3\text{O}_7$). [Barrocas et al. \(2016\)](#). According to previous studies, Raman peaks at 155 and 192 cm^{-1} correspond to the Na-O-Ti lattice modes, while those located at ca. 276, 449, 670 and 693 cm^{-1} are due to the Ti-O-Ti stretching in edge-shared TiO_6 . The band at 914 cm^{-1} is attributed to the stretching vibration of the shorter Ti-O bonds whose oxygen is not shared among the distorted TiO_6 units. The comparison of the base TNT sample and the 5% doped TNT and 5% intercalated TNT shows a clear difference indicating the influence of the Co doping level and the ion position in the structure of the samples. These spectra show that both the highest frequency mode (914 cm^{-1}) and the lowest frequency modes (155 and 192 cm^{-1}) have their wavenumbers and intensities affected either by the higher doping level or by the Co ionic position, in a similar manner to that reported by Marques et al. for Ce^{4+} doping/intercalation within the titanate nanotubes [Marques et al. \(2015\)](#). Besides, the Co(5%)-TNT sample shows an increase in the intensity ratio between the modes at 825 cm^{-1} and 670 cm^{-1} .

The Raman modes at 825 cm^{-1} and 914 cm^{-1} are not observed for intercalated TNT/Co(5%) sample, instead a new mode appeared at about 860 cm^{-1} . Furthermore, the spectrum of the Co(5%)-TNT sample presents a clear broadening and shifting of the wavenumber modes at 449 cm^{-1} and 670 cm^{-1} to 435 cm^{-1} and 693 cm^{-1} , respectively. The fact that these modes correspond to the Ti-O-Ti stretching in edge-shared TiO_6 supports the hypotheses that some ionic cobalt was incorporated between TiO_6 layers during the Co(5%)-TNT sample synthesis process, beyond the expected Co doping via the $\text{Ti}^{4+}/\text{Co}^{2+}$ substitution into the TiO_6 octahedra. The intercalated TNT/Co(5%) sample shows a similar behaviour although less pronounced, the peak at 670 cm^{-1} shifting to 683 cm^{-1} . Additionally, the disappearance of the 914 cm^{-1} mode and the appearance of a new mode at 860 cm^{-1} observed for the intercalated TNT/Co(5%) sample may be seen as a signature of substitution of Na^+ by ionic hydrated Co into TNT interlayers. The TNTs interlayer modification can also be pursued in the low wavenumber range, where the lattice Raman mode at 192 cm^{-1} shifts to 190 cm^{-1} and the intensity of the mode at 155 cm^{-1} decreases (or vanishes) with the substitution of Na^+ by ionic hydrated Co. Thus, the different degrees of structural rearrangement of the prepared samples induced either by Co doping or by Co intercalation is evident from the Raman modes of the samples. Similarly, the [Figure 4.70](#) shows the Raman spectra from TNW sample and 5% doped and intercalated TNW. A similar change in Raman modes are observed in the doped and

intercalated TNW compared to that of the base TNW sample.

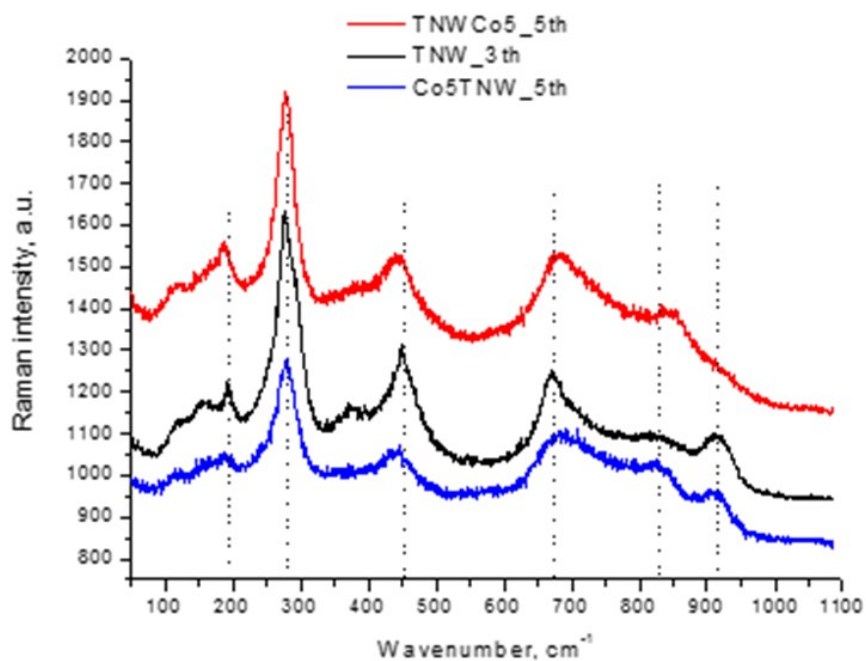


Figure 4.70: Raman spectra of titanate nanowire(TNW) and doped and intercalated titanate nanowires

Chapter 5

Conclusions

Co doped and Co intercalated sodium titanate nanostructures were investigated using several characterization techniques including electron microscopy and spectroscopy. The morphology of the nanotubes and nanowires in the case of doped and intercalated nanotubes were confirmed by TEM and STEM imaging. In order to minimize electron beam induced damage to the sample, electron microscopy was carried out at 80 kV. Electron microscopy studies confirmed that the samples have the multi-wall structure with the numbers of layers being different along the tube axis. HRTEM imaging and HRSTEM imaging revealed the crystallographic orientation of the samples. The interplanar spacing as well as the diameter distribution were obtained from this analysis confirming the nanostructures to be of less than 10 nm in diameters. The interlayer spacing is found to be between 0.7 nm - 0.8 nm and the spacing perpendicular to the walls was between 0.35 nm to 0.38 nm. The interplanar distance obtained from imaging is less than that of expected interplanar spacing from the reported structure of sodium titanate (PDF 00-031-1329). The difference in the lattice parameter could be due to the difference in sodium content as well as the compression of atomic planes during electron microscopy. EDX mapping in STEM mode used to analyze the composition distribution showed the presence of Co in all regions analyzed. However, Co in a single tube/wire is shown to have a nonhomogeneous distribution from the EDX maps. EDX quantification indicated the presence of Co in lower quantities than that of the expected composition in the synthesis. Co incorporation was better achieved in the intercalated TNTs and TNWs than that of doped TNTs and TNWs. The doping achieved in the TNW and TNT samples analyzed were less than 1%. One of the primary requirements to carry out high resolution electron microscopy work is the need of very thin (<100 nm), clean and a stable sample under the beam [Williams and Carter \(2009\)](#).

Though the titanate samples which were studied in this work did not have constraints with respect to the thickness, they were unstable accompanied with carbon build up under the electron beam. This imposed a condition which made it challenging to carry out part of the proposed work such as imaging in combination with Exit Wave Reconstruction as well as atomic resolution Z contrast imaging to distinguish Ti vs Co atoms (sample was disintegrating).

Even though the above mentioned effects were minimised compared to samples which were not heated or plasma cleaned, the stability required was not achievable due to sample being sensitive to the electron beam. One of the ways to overcome instabilities in such samples is by carrying out cryo electron microscopy. In this method the sample is loaded in a specialised holder which can be cooled to cryo temperature by using liquid nitrogen. Cooling of the titanates nanostructures would effectively reduce irradiation damage caused by the electron beam [Yoshida et al. \(2009\)](#). However such experiments were beyond the scope of the current work. EELS analysis was used to obtain the oxidation state of Co in the doped and modified nanostructures. Results obtained, indicates that, in Co doped nanostructures, a mixed oxidation of Co^{2+} and Co^{3+} exist with predominant Co^{2+} with octahedral coordination. However, in the case of Co intercalated titanate nanostructures, Co is shown to be in 2+ oxidation state. Due to the use of EELS, the analysis has a high spatial resolution and the results are from individual tubes. Composition analysis with micrometer resolution, carried out using XPS and Raman spectroscopy, to complement the electron microscopy study confirmed the oxidation states as revealed from EELS but with lesser spatial resolution. XPS analysis indicates that Co is present as 2+ in the intercalated samples (TNT-Co(5%) and TNW-(Co7.5%)) but as a mixture of Co^{2+} and Co^{3+} in the doped samples (Co(5%)-TNT and (Co5%)-TNW) and the results are in good agreement with the conclusion drawn from EELS analysis. XPS quantification of intercalated samples of TNT and TNW shows decreased Na content with increase in Co % confirming the Co incorporation in Na site in the titanate structure. Different degrees of structural rearrangement of the prepared samples induced either by Co doping or by Co intercalation was evident from the Raman modes of the samples as well.

Bibliography

- Ammrf. No Title. URL <http://www.ammrf.org.au/myscope/tem/background/concepts/lenses/poleandcoil.php>.
- B. Barrocas, A. J. Silvestre, A. G. Rolo, and O. C. Monteiro. The effect of ionic Co presence on the structural, optical and photocatalytic properties of modified cobalttitanate nanotubes. *Physical Chemistry Chemical Physics*, 18(27):18081–18093, jul 2016. ISSN 1463-9076. doi: 10.1039/C6CP01889K. URL <http://xlink.rsc.org/?DOI=C6CP01889K>.
- D. V. Bavykin and F. C. Walsh. Elongated Titanate Nanostructures and Their Applications. *European Journal of Inorganic Chemistry*, 2009(8):977–997, mar 2009. ISSN 14341948. doi: 10.1002/ejic.200801122. URL <http://doi.wiley.com/10.1002/ejic.200801122>.
- V. Bem, M. Neves, M. Nunes, A. Silvestre, and O. Monteiro. Influence of the sodium/proton replacement on the structural, morphological and photocatalytic properties of titanate nanotubes. *Journal of Photochemistry and Photobiology A: Chemistry*, 232:50–56, mar 2012. ISSN 1010-6030. doi: 10.1016/J.JPHOTOCHEM.2012.02.002. URL <https://www.sciencedirect.com/science/article/pii/S1010603012000639>.
- M. C. Biesinger, B. P. Payne, A. P. Grosvenor, L. W. Lau, A. R. Gerson, and R. S. Smart. Resolving surface chemical states in XPS analysis of first row transition metals, oxides and hydroxides: Cr, Mn, Fe, Co and Ni. *Applied Surface Science*, 257(7):2717–2730, jan 2011. ISSN 0169-4332. doi: 10.1016/J.APSUSC.2010.10.051. URL <https://www.sciencedirect.com/science/article/pii/S0169433210014170>.
- F. L. Deepak, E. A. Anumol, and J. Li. Advanced Electron Microscopy Techniques Toward the Understanding of Metal Nanoparticles and Clusters. In *Metal Nanoparticles and Clusters*, pages 219–287. Springer International Publishing, Cham,

2018. doi: 10.1007/978-3-319-68053-8_7. URL http://link.springer.com/10.1007/978-3-319-68053-8_{_}7.
- R. F. Egerton. *Electron energy-loss spectroscopy in the electron microscope*. Springer, 2011. ISBN 9781441995834.
- V. C. Ferreira, M. R. Nunes, A. J. Silvestre, and O. C. Monteiro. Synthesis and properties of Co-doped titanate nanotubes and their optical sensitization with methylene blue. aug 2013. doi: 10.1016/j.matchemphys.2013.07.029. URL <http://arxiv.org/abs/1308.5652><http://dx.doi.org/10.1016/j.matchemphys.2013.07.029>.
- I. Gatan. Extract signal — EELS.info. URL <http://www.eels.info/how/quantification/extract-signal>.
- G. Gouadec and P. Colomban. Raman Spectroscopy of nanomaterials: How spectra relate to disorder, particle size and mechanical properties. *Progress in Crystal Growth and Characterization of Materials*, 53(1):1–56, mar 2007. ISSN 0960-8974. doi: 10.1016/J.PCRYSGROW.2007.01.001. URL <https://www.sciencedirect.com/science/article/pii/S0960897407000022>.
- M. Haider, P. Hartel, H. Müller, S. Uhlemann, and J. Zach. Current and future aberration correctors for the improvement of resolution in electron microscopy. *Philosophical transactions. Series A, Mathematical, physical, and engineering sciences*, 367(1903):3665–82, sep 2009. ISSN 1364-503X. doi: 10.1098/rsta.2009.0121. URL <http://www.ncbi.nlm.nih.gov/pubmed/19687059>.
- K. Hashimoto, H. Irie, and A. Fujishima. TiO ₂ Photocatalysis: A Historical Overview and Future Prospects. *Japanese Journal of Applied Physics*, 44(12):8269–8285, dec 2005. ISSN 0021-4922. doi: 10.1143/JJAP.44.8269. URL <http://stacks.iop.org/1347-4065/44/8269>.
- K. Holsgrove. *TRANSMISSION ELECTRON MICROSCOPY STUDY OF DOMAINS IN FERROELECTRICS*. PhD thesis, Queen’s University Belfast, 2017.
- R. Huang, Y. H. Ikuhara, T. Mizoguchi, S. D. Findlay, A. Kuwabara, C. A. J. Fisher, H. Moriwake, H. Oki, T. Hirayama, and Y. Ikuhara. Oxygen-Vacancy Ordering at Surfaces of Lithium Manganese(III,IV) Oxide Spinel Nanoparticles. *Angewandte Chemie*, 123(13):3109–3113, mar 2011. ISSN 00448249. doi: 10.1002/ange.201004638. URL <http://doi.wiley.com/10.1002/ange.201004638>.

- R. Ishikawa, E. Okunishi, H. Sawada, Y. Kondo, F. Hosokawa, and E. Abe. Direct imaging of hydrogen-atom columns in a crystal by annular bright-field electron microscopy. *Nature Materials*, 10(4):278–281, apr 2011. ISSN 1476-1122. doi: 10.1038/nmat2957. URL <http://www.nature.com/articles/nmat2957>.
- O. L. Krivanek, J. P. Ursin, N. J. Bacon, G. J. Corbin, N. Dellby, P. Hrcirik, M. F. Murfitt, C. S. Own, and Z. S. Szilagy. High-energy-resolution monochromator for aberration-corrected scanning transmission electron microscopy/electron energy-loss spectroscopy. *Philosophical transactions. Series A, Mathematical, physical, and engineering sciences*, 367(1903):3683–97, sep 2009. ISSN 1364-503X. doi: 10.1098/rsta.2009.0087. URL <http://www.ncbi.nlm.nih.gov/pubmed/19687060>.
- Z.-Q. Li, W.-C. Chen, F.-L. Guo, L.-E. Mo, L.-H. Hu, and S.-Y. Dai. Mesoporous TiO₂ Yolk-Shell Microspheres for Dye-sensitized Solar Cells with a High Efficiency Exceeding 11%. *Scientific Reports*, 5(1):14178, nov 2015. ISSN 2045-2322. doi: 10.1038/srep14178. URL <http://www.nature.com/articles/srep14178>.
- W. Liu, X. Zhao, T. Wang, D. Zhao, and J. Ni. Adsorption of U(VI) by multilayer titanate nanotubes: Effects of inorganic cations, carbonate and natural organic matter. *Chemical Engineering Journal*, 286:427–435, feb 2016. ISSN 1385-8947. doi: 10.1016/J.CEJ.2015.10.094. URL <https://www.sciencedirect.com/science/article/pii/S1385894715015053>.
- T. M. Marques, O. P. Ferreira, J. A. da Costa, K. Fujisawa, M. Terrones, and B. C. Viana. Study of the growth of CeO₂ nanoparticles onto titanate nanotubes. *Journal of Physics and Chemistry of Solids*, 87:213–220, dec 2015. ISSN 0022-3697. doi: 10.1016/J.JPCS.2015.08.022. URL <https://www.sciencedirect.com/science/article/abs/pii/S0022369715300536>.
- M. Matsuoka and M. Anpo. Applications of Environmentally Friendly TiO₂ Photocatalysts in Green Chemistry: Environmental Purification and Clean Energy Production Under Solar Light Irradiation. In *Handbook of Green Chemistry*, pages 59–80. Wiley-VCH Verlag GmbH & Co. KGaA, Weinheim, Germany, jul 2010. doi: 10.1002/9783527628698.hgc015. URL <http://doi.wiley.com/10.1002/9783527628698.hgc015>.
- H. McDaniel, N. Fuke, N. S. Makarov, J. M. Pietryga, and V. I. Klimov. An integrated approach to realizing high-performance liquid-junction quantum dot sensitized solar

- cells. *Nature Communications*, 4(1):2887, dec 2013. ISSN 2041-1723. doi: 10.1038/ncomms3887. URL <http://www.nature.com/articles/ncomms3887>.
- K. Nakata and A. Fujishima. TiO₂ photocatalysis: Design and applications. *Journal of Photochemistry and Photobiology C: Photochemistry Reviews*, 13(3):169–189, sep 2012. ISSN 13895567. doi: 10.1016/j.jphotochemrev.2012.06.001. URL <http://linkinghub.elsevier.com/retrieve/pii/S1389556712000421>.
- Nanophoton. Raman Spectroscopy. URL <https://www.nanophoton.net/raman/raman-spectroscopy.html>.
- D. H. Pearson, B. Fultz, and C. C. Ahn. Measurements of 3 *d* state occupancy in transition metals using electron energy loss spectrometry. *Applied Physics Letters*, 53(15):1405–1407, oct 1988. ISSN 0003-6951. doi: 10.1063/1.100457. URL <http://aip.scitation.org/doi/10.1063/1.100457>.
- S. Pennycook and D. Jesson. High-resolution Z-contrast imaging of crystals. *Ultramicroscopy*, 37(1-4):14–38, aug 1991. ISSN 0304-3991. doi: 10.1016/0304-3991(91)90004-P. URL <https://www.sciencedirect.com/science/article/pii/030439919190004P>.
- J. Schneider, M. Matsuoka, M. Takeuchi, J. Zhang, Y. Horiuchi, M. Anpo, and D. W. Bahnemann. Understanding TiO₂ Photocatalysis: Mechanisms and Materials. *Chemical Reviews*, 114(19):9919–9986, oct 2014. ISSN 0009-2665. doi: 10.1021/cr5001892. URL <http://pubs.acs.org/doi/10.1021/cr5001892>.
- Sergiu P. Albu, Andrei Ghicov, Jan M. Macak, , Robert Hahn, and P. Schmuki*. Self-Organized, Free-Standing TiO₂ Nanotube Membrane for Flow-through Photocatalytic Applications. 2007. doi: 10.1021/NL070264K. URL <https://pubs.acs.org/doi/abs/10.1021/nl070264k>.
- J. C. H. Spence and A. V. Crewe. *Experimental HighResolution Electron Microscopy*. *Physics Today*, 34(9):90–90, sep 1981. ISSN 0031-9228. doi: 10.1063/1.2914772. URL <http://physicstoday.scitation.org/doi/10.1063/1.2914772>.
- VESTA. VESTA. URL <http://jp-minerals.org/vesta/en/>.
- Z. Wang, J. Yin, and Y. Jiang. EELS analysis of cation valence states and oxygen vacancies in magnetic oxides. *Micron*, 31(5):571–580, oct 2000. ISSN 0968-4328. doi:

10.1016/S0968-4328(99)00139-0. URL <https://www.sciencedirect.com/science/article/pii/S0968432899001390>.

D. B. Williams and C. B. Carter. *Transmission Electron Microscopy*. Springer US, Boston, MA, 2009. ISBN 978-0-387-76500-6. doi: 10.1007/978-0-387-76501-3. URL <http://link.springer.com/10.1007/978-0-387-76501-3>.

K. Yoshida, L. Miao, N. Tanaka, and S. Tanemura. Direct observation of TiO₆ octahedron forming titanate nanotube by advanced transmission electron microscopy. *Nanotechnology*, 20(40):405709, oct 2009. ISSN 0957-4484. doi: 10.1088/0957-4484/20/40/405709. URL <http://stacks.iop.org/0957-4484/20/i=40/a=405709?key=crossref.9fb8dc50433dcbc5bc88fddec8fb29e7>.